UNI
FR
UNIVERSITÉ DE FRIBOURG FACULTÉ DES SCIENCES
UNIVERSITÄT FREIBURG MATHEMATISCH-NATURWISSENSCHAFTLICHE FAKULTÄT

Department of Physics
University of Fribourg (Switzerland)

Energies and widths of atomic core levels in liquid mercury

and

Hypersatellite decay of $20 \leqslant Z \leqslant 29$ target elements bombarded by heavy-ions

THESIS

presented to the Faculty of Science of the University of Fribourg (Switzerland)
in consideration for the award of the academic grade of *Doctor rerum naturalium*

by

Yves-Patrik Maillard
from
Switzerland

Thesis No: 1995
UniPrint Fribourg
2016

UNI
FR
UNIVERSITÉ DE FRIBOURG FACULTÉ DES SCIENCES
UNIVERSITÄT FREIBURG MATHEMATISCH-NATURWISSENSCHAFTLICHE FAKULTÄT

Department of Physics
University of Fribourg (Switzerland)

Energies and widths of atomic core levels in liquid mercury

and

Hypersatellite decay of $20 \leqslant Z \leqslant 29$ target elements bombarded by heavy-ions

THESIS

presented to the Faculty of Science of the University of Fribourg (Switzerland)
in consideration for the award of the academic grade of *Doctor rerum naturalium*

by

Yves-Patrik Maillard
from
Switzerland

Thesis No: 1995
UniPrint Fribourg
2016

Accepted by the Faculty of Science of the University of Fribourg (Switzerland) upon the recommendation of:

Prof. Dr. Antoine Weis, University of Fribourg (President of the jury),
Prof. Dr. Jean–Claude Dousse, University of Fribourg (Thesis Supervisor),
Prof. Dr. Marek Pajek, University of Kielce, Poland (External reviewer),
Dr. hab. Joanna Hoszowska, University of Fribourg (Internal reviewer).

Fribourg, December 9th, 2016

Thesis supervisor	Dean
Prof. Dr. Jean-Claude Dousse	Prof. Dr. Christian Bochet

CONTENTS

ABSTRACT

The present PhD thesis contains two parts which are both related to the domain of X-ray and inner-shell atomic physics. The first part consists in a detailed investigation of the photoinduced X-ray emission of liquid mercury, while the second one concerns the radiative decay of hollow K-shell atoms bombarded by heavy ions. While the two subjects are thus quite different, they share the same experimental technique, both projects having been carried out by means of high energy resolution X-ray spectroscopy.

Mercury has been widely used in the past for making thermometers and barometers, diffusion pumps, Hg-vapor lamps and other electrical devices. Pesticides, dental preparations, batteries and catalysts are further examples of the use of the liquid metal in everyday life. Because mercury wastes have not always been eliminated properly in the past decades, this dangerous metal has spread out and accumulated in nature. As it is even found in the human food chain, mercury pollution has become a domain of extensive research in present-day environmental studies.

Among the methods employed to detect traces of mercury, the X-ray fluorescence (XRF) techniques is probably the most efficient one. In the XRF technique, the concentrations of the elements of interest are determined from the relative yields of the sample X-ray lines. Energies of the latter have thus to be known accurately to identify unambiguously the observed transitions. On the other hand, Hg is the heaviest stable element having all electronic subshells filled in the ground state. Precise experimental data concerning the transition energies and transition widths of mercury are therefore particularly adequate to probe the accuracy of atomic structure calculations of heavy elements, such calculations being more tractable and their results more reliable for elements having a $^1S_0$ ground state configuration.

The K-, L- and M-shell X-ray fluorescence of liquid Hg was measured in high energy resolution using the Laue-type DuMond and Bragg-type von Hamos spectrometers of Fribourg. The measurements were performed in-house. The Hg X-ray fluorescence was produced by irradiating the sample with the Bremsstrahlung of X-ray tubes. A set of 32 transitions was measured, more specifically 6 K, 26 L and 2 M X-ray transitions. All X-ray lines were fitted with Voigt profiles. The energies, Lorentzian widths and intensities of the lines were determined from the fits. Furthermore, solving by means of a least-squares-fit method the two linear systems of simultaneous equations built on the obtained transition energies and transition widths, the binding energies and natural widths of most core-levels of Hg could be deduced.

The second subject investigated in this PhD concerns the radiative decay of hollow K-shell atoms. Hollow K-shell atoms are atoms with an empty $1s$ level in the initial state. The X-rays emitted during the radiative decay of such double $1s$ vacancy states are shifted towards higher energies with respect to the diagram X-rays accompanying the decay of single $1s$ vacancy states. The energy shifts are typically 10 times bigger than the ones of L-shell satellites and about 50 times bigger than those of M-shell satellites. For this reason the X-rays emitted by hollow K-shell atoms are called K hypersatellite X-rays.

Hollow K-shell atoms can be produced via nuclear decay processes such as the electron capture (EC), β-decay or α-decay but the probability is very weak, typically in the order of 10^{-4}. The same holds for the creation of hollow atoms by impact with photons and electrons, double K-shell ionization (DPI) probabilities varying between 10^{-2} for light elements down to 10^{-6} for high-Z elements. Stronger K-hypersatellite signals can be obtained by bombarding the samples with heavy ions (HI). In this case, due to the strong Coulomb field of the charged projectiles, several inner-shell electrons can be indeed ionized simultaneously. The satellite and hypersatellite yields resulting from atomic collisions with heavy ions being much higher than those produced by photon and electron impact, the use of crystal spectrometers is mandatory to unravel the complex satellite and hypersatellite structure of HI-induced X-ray spectra,

In this project, we have investigated the radiative decay of double K-shell vacancy states produced in solid Ca, V, Fe and Cu targets by impact with about 10 MeV/amu C and Ne ions. The K hypersatellite X-ray lines were measured with the von Hamos crystal spectrometer of Fribourg. The experiment was carried out at the Philips variable energy cyclotron of PSI during two different runs of about one week each. From the fits of the X-ray spectra corrected beforehand for the beam intensity fluctuations and the beam intensity profile on the target as well as for the variation with the energy of the solid angle of the spectrometer, the energies, line widths and relative intensities of the hypersatellite lines could be determined.

The first aim of the project was to determine the single-to-double K-shell ionization cross sections for the 8 investigated collisions. The cross section ratios were deduced from the corrected relative intensities of the hypersatellites. The results were found to be rather well reproduced by the semi-classical approximation (SCA) model based on Dirac Hartree Fock (DHF) wave functions but also systematically bigger than the SCA predictions. The discrepancy was explained by the fact that the electron capture (EC) process which is not considered in the SCA model plays an important role in the investigated collisions and leads to bigger cross section ratios. However, as it appears in the related literature, theory strongly overestimates the EC cross sections. The difficulty was circumvented by correcting the EC contribution with a scaling factor α which was determined by a least-squares fit method. Finally, using the SCA DHF model for the determination of the impact-induced ionization cross sections and the predictions of classical trajectory Monte-Carlo (CTMC) calculations corrected by the scaling factor α=0.11 for the EC cross sections, a nice agreement was found between theory and experiment.

Résumé

Cette thèse est constituée de deux parties afférentes aux domaines de la métrologie des rayons X pour l'une et à celui de la physique atomique en couches profondes pour l'autre. La première partie présente une étude détaillée des rayons X photo-induits émis par le mercure liquide. La seconde concerne la désexcitation radiative d'atomes creux, c'est-à-dire avec une couche électronique K vide, produits par bombardement avec des ions lourds. Les deux sujets, bien que passablement différents dans leur substance, ont en commun l'application d'une même technique expérimentale, à savoir la spectroscopie de rayons X en haute résolution.

Le mercure a été largement utilisé dans le passé. Les thermomètres, baromètres, lampes à vapeur de mercure ou encore les contacteurs électriques n'en sont que quelques exemples bien connus. Les pesticides, les amalgames dentaires, les batteries et les catalyseurs sont d'autres exemples d'utilisation de cet élément dans la vie de tous les jours. Comme les déchets de mercure n'ont pas toujours été éliminés de manière appropriée dans le passé, ce métal toxique a été disséminé et accumulé dans la nature et on le retrouve par exemple, dans la chaîne alimentaire qui aboutit à l'homme. La pollution par le mercure est ainsi devenue un sujet d'importance dans le cadre des études environnementales actuelles.

Parmi les techniques utilisées pour détecter des très faibles concentrations de mercure, la méthode XRF (X-Ray Fluorescence) basée sur la détection des rayons X caractéristiques est sans doute l'une des plus efficaces. La technique XRF permet de quantifier la concentration des éléments d'intérêt à partir des intensités relatives des raies X de ces derniers. Pour ce faire, toutefois, les énergies des rayons X caractéristiques doivent être connues avec précision afin de pouvoir identifier sans équivoque les raies observées. D'autre part, le mercure est l'élément stable le plus lourd présentant une configuration électronique avec toutes les sous-couches pleines dans son état fondamental. Ainsi, des données expérimentales précises pour les énergies et les largeurs des transitions du mercure sont particulièrement utiles

pour vérifier les résultats de calculs de la structure atomique d'éléments lourds. Les calculs de structure atomique sont en effet plus faciles à aborder et leurs résultats plus fiables pour des éléments ayant une configuration $^1S_0$ dans leur état fondamental.

Les rayons X de fluorescence des couches K, L et M du mercure liquide ont été mesurées en haute résolution au moyen des deux spectromètres à cristal de Fribourg, à savoir le spectromètre DuMond, de type Laue, et le spectromètre von Hamos, de type Bragg. Les mesures ont été réalisées à Fribourg. La fluorescence a été obtenue en irradiant le mercure liquide avec le Bremsstrahlung de tubes à rayons X. Les mesures ont porté sur un ensemble de 32 transitions X, plus précisément 6 transitions K, 26 L et 2 M. Les raies mesurées ont toutes été analysées avec des profils voigtiens. Les énergies, les largeurs lorentziennes ainsi que les intensités des raies spectrales ont été déterminées à partir des fits. D'autre part, en résolvant par la méthode des moindres carrés les deux systèmes surdéterminés d'équations linéaires correspondant respectivement aux énergies des transitions mesurées et aux largeurs naturelles de ces dernières, nous avons pu déterminer les énergies et les largeurs de la plupart des niveaux atomiques de coeur du mercure.

Le second sujet de la thèse concerne la désexcitation radiative d'atomes creux, c'est-à-dire d'atomes présentant la particularité d'avoir leur niveau 1s vide dans l'état initial. Les rayons X émis lors de telles désexcitations ont une énergie sensiblement plus grande que celle des rayons X diagrammes émis par les atomes n'ayant qu'une seule lacune initiale 1s. Ces raies X particulières sont appelés raies hypersatellites K car leurs décalages en énergie par rapport aux raies diagrammes parentes sont typiquement 10 fois supérieures à celles des raies satellites L (1 lacune spectatrice dans la couche L) ou 50 fois supérieures à celles des raies satellites M (1 lacune spectatrice dans la couche M).

Les atomes creux peuvent être produits par des processus nucléaires comme la capture électronique (EC), la désintégration β ou encore la désintégration α. Dans ces processus, toutefois, la probabilité de créer des atomes creux est faible, de l'ordre de 10^{-4}. Il en va de même pour les méthodes de production consistant à bombarder les atomes avec des photons ou des électrons, la probabilité de création d'une double lacune K variant dans ce cas de 10^{-2} pour les éléments légers jusqu'à 10^{-6} pour les éléments lourds. Par contre, en bombardant les cibles à l'aide d'ions lourds, un signal hypersatellite K nettement plus fort est obtenu. Dans ce cas en effet, l'interaction de Coulomb entre les projectiles chargés et les électrons ato-

miques produit en général une ionisation multiple des atomes-cibles. Il en résulte des spectres X complexes caractérisés par des structures satellites et hypersatellites très denses que seuls des spectromètres à cristal permettent de résoudre.

Dans le cadre de ce second projet, nous avons étudié les désexcitations radiatives de doubles lacunes K produites dans des cibles solides de Ca, V, Fe et Cu par impact avec avec des ions de carbone et de néon ayant une énergie cinétique d'environ 10 MeV/amu. Les transitions hypersatellites K ont été mesurées au moyen du spectromètre à cristal von Hamos de Fribourg. Les mesures ont été effectuées à l'Institut Paul Scherrer (PSI), auprès du cyclotron à énergie variable Philips, au cours de deux périodes de faisceau d'environ une semaine chacune. Les spectres mesurés ont tout d'abord été corrigés pour les fluctuations d'intensité du faisceau et la forme de ce dernier sur la cible ainsi que pour la variation de l'angle solide du spectromètre en fonction de l'énergie, puis analysés au moyen du logiciel PeakFit. Les énergies, les largeurs ainsi que les intensités relatives des hypersatellites ont pu être déterminées.

Le projet avait pour objectif premier la détermination des rapports de sections efficaces de simple et double ionisation K pour chacune des 8 collisions étudiées. Les rapports des sections efficaces ont été déterminés à partir des intensités relatives corrigées des hypersatellites. Les résultats expérimentaux obtenus sont assez bien reproduits par le modèle d'approximation semi-classique (SCA) basé sur des fonctions d'onde de Dirac Hartree Fock (DHF), mais systématiquement plus grands que les prédictions de ce dernier. La différence a été expliquée par le fait que le processus de capture électronique (EC) qui augmente les rapports de section efficace n'est pas pris en compte dans le modèle SCA alors qu'il joue un rôle important pour les collisions étudiées. Les sections efficaces de capture électronique peuvent être calculées au moyen du modèle CTMC (classical trajectory Monte-Carlo) mais ce dernier surestime considérablement la contribution du processus EC. La difficulté a été contournée en multipliant la contribution EC par un facteur de correction α déterminé par la méthode des moindres carrés. Finalement, en utilisant le modèle SCA DHF pour la détermination des sections efficaces d'ionisation directe et les prédictions du modèle CTMC corrigées par le facteur α=0.11 pour les sections efficaces de capture électronique, un bon accord a été trouvé entre les rapports de sections efficaces expérimentaux et théoriques.

CHAPTER I

INTRODUCTION

I.1 Preamble

The present work contains two different projects which belong both to the domain of inner-shell atomic physics and X-ray spectroscopy. More specifically the first project consists of an extensive series of in-house measurements of the characteristic X-ray emission spectra of liquid mercury. The second one concerns the X-ray hypersatellite decay of four solid $3d$ elements excited by impact with moderately fast heavy ions. This second series of measurements was performed at the Philips cyclotron of the Paul Scherrer Institute.

In the first project not only the energies of the transitions were of interest but also the natural line widths of the latter. To get reliable results, a detector having a similar energy resolution as the line widths to be determined was thus required. Since K X-ray spectra induced by collision with heavy ions are characterized by very rich L-shell satellite structures that are close lying and even partly overlapping with the K hypersatellite lines, high energy resolution was also a mandatory prerequisite for the second project. For these reasons, both projects were carried out by means of high energy resolution X-ray spectroscopy, using two crystal spectrometers, a DuMond Laue type bent crystal spectrometer for the measurements of X-rays above about 11 keV and a von Hamos Bragg type bent crystal spectrometer for the measurements of X-rays of lower energies. The high-energy resolution X-ray spectroscopy technique represents thus the common denominator of the two projects. A brief reminder of the basic principles of X-ray crystal spectroscopy is outlined in Sect. I.2, while Sects. I.3 and I.4 introduce more specifically the two subjects of this thesis.

I.2 High energy resolution X-ray spectroscopy

The discovery of X-rays by W. C. Röntgen in 1895 has opened a wide field of further investigations resulting into a tremendous number of applications in everyday life. Among the stages of progress in that new science, those concerning the development of X-ray detectors are pointed out hereafter, in connection with the content of this thesis.

X-ray detectors can be divided into two groups, depending on their energy resolution and sensitivity. The group of *energy dispersive detectors* includes gas detectors, scintillators and semiconductor detectors called also diodes. In such devices, an electrical signal is produced, whose amplitude is proportional to the energy deposed by the radiation in the active volume of the detector. This category of detectors is characterized by a high efficiency, a high linearity, a good time resolution and a resolving power which varies from about 20% for the scintillators down to about 10%-5% for the proportional counters (gas detectors) and about 1% for the Si or Ge semiconductor detectors. The time response is in the order of 10^{-6} s for gas detectors and diodes and in the order of 10^{-9} s for plastic scintillators.

In *wavelength dispersive detectors* which originate from the pioneering works of W. L. Bragg around 1915, the energy of the photon is derived from the so-called Bragg angle (see below) and the spacing constant of the crystal diffraction planes. Wavelength dispersive detectors are characterized by an excellent relative energy resolution in the order of 0.01%, a high sensitivity but also, unfortunately, a poor efficiency. The latter is mainly due to the small solid angles sustained by wavelength dispersive detectors.

While in energy dispersive detectors the detection of X-rays is based on the photo effect and thus related to the particle-nature of the incoming radiation, in wavelength dispersive detectors it is the wave-like nature of the photons which is used since the electromagnetic wave associated to the incoming photon is diffracted by the regularly spaced atoms of the crystal lattice. Actually, thanks to their periodic structure, crystals present the property of reinforcing the amplitude of the diffracted wave if the path length between successive diffraction planes is an integer multiple of the incoming radiation wavelength (see Fig. I.1 and I.2). Mathematically this coherent scattering condition is given by the following equation which is referred to as the Bragg law:

$$2 \cdot d_{hk\ell} \cdot \sin(\vartheta) = n \cdot \lambda = n \cdot \frac{h \cdot c}{E}, \tag{I.1}$$

where $d_{hk\ell}$ is the reticular distance, ϑ the angle of the incoming and outgoing radiation with respect to the diffraction planes, n a positive integer number called diffraction order, λ and E the wavelength and energy of the considered X-rays, h the Planck constant and c the velocity of light in vacuum.

If the Bragg law is not fulfilled, the diffracted signal vanishes due to destructive interferences. Note that the Bragg law is a necessary but not sufficient condition to get a diffraction. In fact, the intensity of the diffracted wave is proportional to the squared modulus of the structure factor $F_{hk\ell}$ which, depending on the arrangement of the atoms in the elementary cell of the crystal, can be zero. For instance, for face centered cubic crystals such as silicon and germanium, the structure factor is

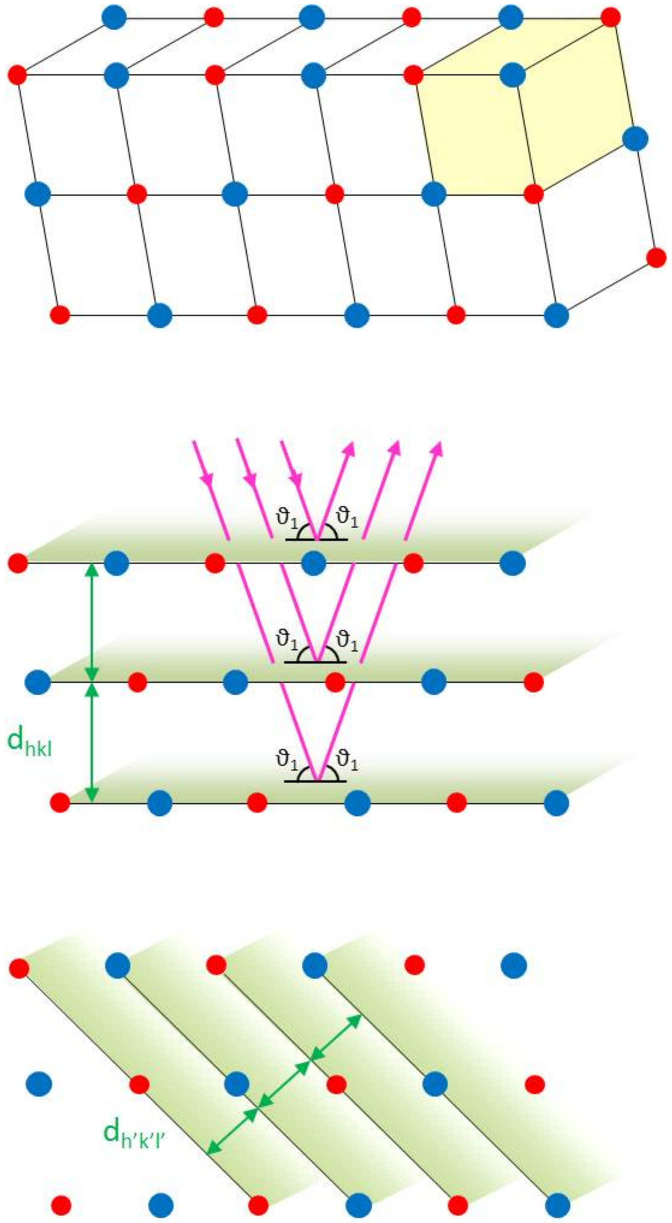

Figure I.1 – Crystal structure. Depending on the cut of the crystal plate, diffraction planes with different orientations can be used. The latter are defined by the Miller indices $(hk\ell)$. The interplanar spacing $d_{hk\ell}$ called also reticular distance depends on the chosen diffraction planes.

only different from zero when the Miller indices $(hk\ell)$ are all even or all odd. In other words no diffraction will be observed for crystal planes such as (110) because $F_{110} = 0$, but a strong diffraction does exist for the planes (111). The structure factor which is in general a complex number is defined by [1]:

$$F_{hk\ell} = \sum_{j=1}^{N} f_j \cdot e^{2\pi \cdot i \cdot (h \cdot x_j + k \cdot y_j + \ell \cdot z_j)} \quad , \tag{I.2}$$

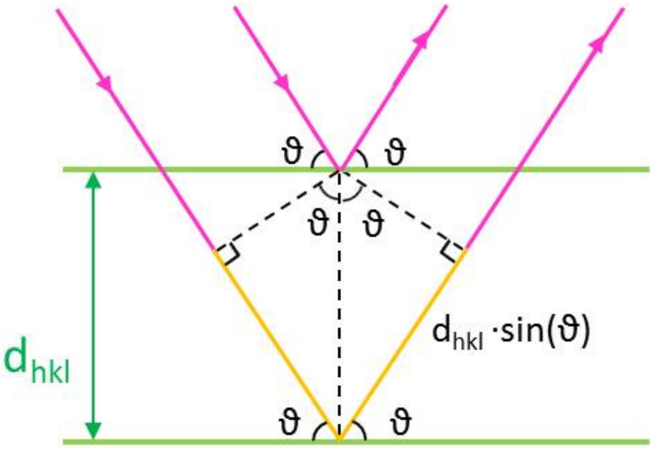

Figure I.2 – Schematic drawing to derive the Bragg law (Eq. I.1) for the 1^{st} diffraction order. The yellow lines represent the path length difference between the partial waves diffracted by two adjacent crystal planes.

where f_j represents the atomic scattering factor of the j^{th} atom in the elementary cell of the crystal, N the number of different atoms in this cell, i the unit imaginary number and x_j, y_j and z_j the spatial coordinates of the j^{th} atom.

As mentioned before, crystal spectrometers are characterized by a relative energy resolution $\Delta E/E$ of about 10^{-4}. The highest resolving power is provided by setups based on flat crystals. In counterpart, the solid angle and hence the efficiency of flat crystal spectrometers is very low. Indeed, in X-ray emission spectroscopy the radiation from the source being divergent, the Bragg law can be satisfied only by a small area of the crystal if the latter is flat. To increase the reflecting area, the crystal plate can be bent cylindrically or spherically. Depending on the chosen geometry, the radius of curvature ranges from a few centimeters up to several meters. If the source of radiation is placed on the Rowland circle, i.e., on the virtual circle having a radius equal to the half value of the radius of the crystal curvature and passing by the crystal center and the curvature center, simple geometrical considerations show that the whole surface of the bent crystal satisfies the Bragg condition, which results in a tremendous enhancement of the solid angle. The enhancement factor varies between 10^2 and 10^3 depending on the crystal size. The price to pay for this efficiency increase is some loss in the energy resolution as a result of the imperfections in the crystal curvature or the quasi-mosaicity induced in the crystal plate by the curvature.

Bent crystal spectrometers can be operated in the Bragg or Laue diffraction mode. In the Bragg mode, the diffraction planes are parallel to the front surface of the

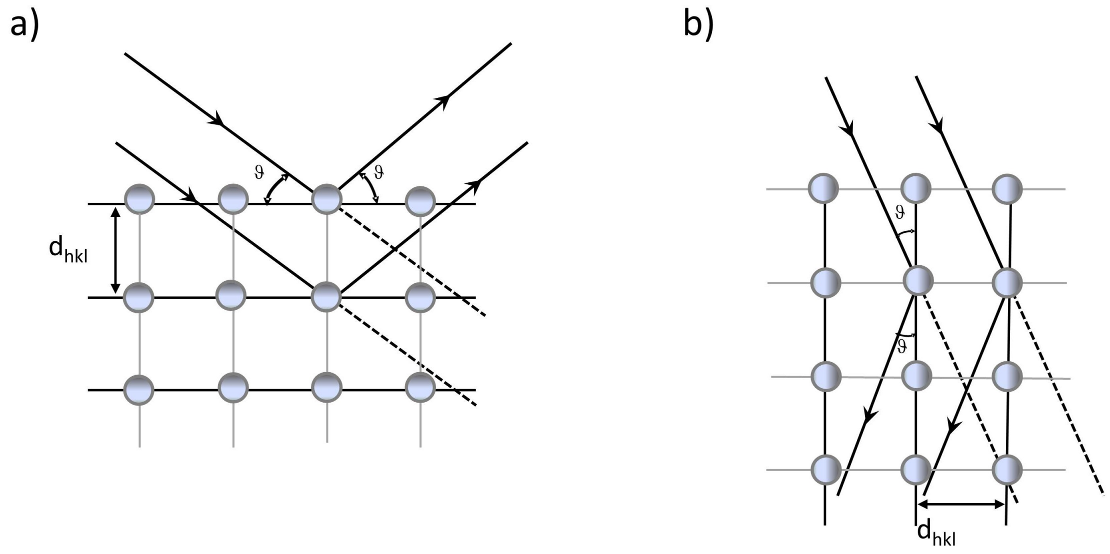

Figure I.3 – a) Bragg and b) Laue diffraction geometries.

crystal, i.e., the surface exposed to the incoming radiation, whereas in the Laue mode the diffraction planes are normal to the front surface of the curved crystal plate. Thus, in the Bragg mode, the incoming and diffracted X-ray beams are located on the same side of the crystal, whereas in the Laue mode the diffracted X-rays emerge from the rear surface of the crystal plate (see Fig.I.3). For this reason the Bragg mode is also called reflection setup and the Laue mode transmission setup. In the Laue mode, the photons have to cross the crystal plate to reach the detector. This results in an attenuation of the intensity of the incident and diffracted radiation. This attenuation grows drastically when the photon energy decreases. For instance for a 1 mm thick quartz crystal plate, the absorption which amounts to about 4% at 100 keV reaches about 99% at 10 keV. For this reason, Laue-type crystal spectrometers are usually employed for hard and tender X-rays whose energies are bigger than about 10 keV. On the other hand, due to geometrical constraints in the design of the spectrometer, the minimum Bragg angles sustainable by Bragg-type crystal spectrometers cannot be below about 20°. For crystals commonly used in X-ray spectroscopy, Bragg angles $\vartheta \geq 20°$. correspond to photon energies $E \leq 15$ keV. In that sense, Laue-type and Bragg-type crystal spectrometers can be considered as complementary high energy resolution X-ray detectors. A more comprehensive overview of crystal spectrometers can be found in Ref. [2].

In the mercury project the K X-ray spectrum and most of the L X-ray transitions were measured with a DuMond Laue-type bent crystal spectrometer, whereas the low energy part of the L X-ray spectrum as well as a few M X-ray transitions were measured using a von Hamos Bragg-type crystal spectrometer. In the second project, the energies of the hypersatellites of interest being all smaller than 10 keV, the measurements were also performed with the von Hamos spectrometer. Both instruments were designed, constructed and developed in Fribourg before the beginning of the present thesis. More detailed information about the two spectrometers are given in Chap. II and Chap. III.

I.3 Mercury project

The mercury project can be viewed in the broader context of the X-ray metrology activities of the Atomic and X-Ray Physics group (AXP) of the University of Fribourg. These activities include the precise determination of the

(i) energies and natural widths of X-ray transitions and/or core atomic levels,

(ii) the relative intensities of X-ray lines, and

(iii) the cross sections of exotic atomic inner-shell decay processes.

Past works belonging to the first category (i) were devoted either to a particular atomic subshell investigated for a series of elements through the Periodic Table [3–5]) or to many subshells of one or two selected elements [6–8]. The $K\beta/K\alpha$ yield ratio measurements performed within the international X-Ray Fundamental Parameters Initiative collaboration is an example of the second category (ii) of projects which includes also the measurements of much weaker transitions such as the forbidden $2s$-$1s$ M1 transition in several heavy elements [9] or the two-electron-one photon (TEOP) transitions which represent an alternative decay channel of double K-shell vacancy states [10]. Among the 3^{rd} category (iii) of X-ray metrology projects carried out in Fribourg, one can mention the determination of the cross sections of the radiative Auger effect [11–13] and X-Ray resonant Raman scattering [14, 15].

The mercury study presented in the second chapter of this thesis can be linked with the first category (i) of X-ray metrology projects. The measurements of the photoinduced X-ray emission of the heavy element (Z = 80) were performed using the DuMond crystal spectrometer for transitions above 11 keV and the von Hamos crystal spectrometer for transitions below 11 keV. The target X-ray fluorescence was produced by irradiating the liquid sample with the Bremsstrahlung from X-ray tubes. The energies and natural line widths of 6 K-shell, 26 L-shell and 2 M-shell

X-ray transitions were determined. Using a least-squares-fit method to solve the two sets of equations derived from the observed transition energies and transition widths, the binding energies of the subshells K to M_5 and O_1 and the level widths of the subshells K to N_5 and O_1 could also be determined. The main results of this study have been already published [16].

I.4 Hypersatellite project

Hypersatellite lines are X-ray lines that are emitted in the presence of a spectator vacancy located in the same shell as the primary hole. Such X-ray lines are called hypersatellites because their energy shifts with respect to the parent diagram lines are significantly bigger than those of satellite lines for which the spectator holes are located in more outer shells than the primary vacancies. $K\alpha$ and $K\beta$ hypersatellites, noted $K\alpha^h$ and $K\beta^h$, respectively, correspond thus to the transitions $1s^{-2}$ - $1s^{-1}2p^{-1}$ and $1s^{-2}$ - $1s^{-1}3p^{-1}$.

Accurate measurements of hypersatellite energies are very useful to probe the goodness of atomic structure calculations because the energies of hypersatellite transitions are more sensitive than diagram transitions to the Breit interaction, quantum electrodynamics (QED) corrections and relativity effects. The $K\alpha_1^h$ hypersatellite is forbidden by the E1 selection rules in the pure LS-coupling scheme. It is, however, allowed in the jj-coupling scheme. The $K\alpha_2^h$ hypersatellite is allowed in both coupling schemes. As a consequence, the $K\alpha_1^h/K\alpha_2^h$ intensity ratio allows to probe the intermediacy of the coupling scheme across the periodic table [17, 18]. A further interest of hypersatellite X-ray lines resides in their natural line widths from which the mean lifetimes of double $1s$ vacancy states can be determined and compared to theory [19]. Finally, in atomic collisions involving heavy ions (HI), the double-to-single K-shell ionization cross section ratios which can be derived from the relative hypersatellite yields permit to check the reliability of the predictions from different theoretical models such as the SCA (Semi-Classical Approximation), PWBA (Plane Wave Born Approximation) and CTMC (Classical Trajectory Monte-Carlo) models. A reliable knowledge of double K-shell ionization cross sections is also needed in a variety of applications such as plasma diagnostics [20] or the interpretation of the X-ray radiation from the Universe [21].

The K hypersatellite study of this thesis is a continuation of former projects in which the double K-shell vacancies were produced by impact with electrons [22], photons [23, 24] as well as light and heavy ions [18, 25]. L- and M-shell hypersatellites induced by impact with fast heavy ions were also investigated before this work [26–28].

In the above mentioned electron and photon induced hypersatellite studies low-Z atoms were investigated, whereas the HI-induced hypersatellite measurements concerned heavier elements (Zr, Mo, Pd and Th). The project carried out within this thesis is devoted to HI-induced K hypersatellites of several mid-heavy elements. Indeed, high energy-resolution measurements of the $K\alpha$-hypersatellite X-ray spectra of Ca, V, Fe and Cu were performed. For Ca and V, the $K\beta$-hypersatellite X-ray spectra were also measured. The double $1s$ ionization of the target atoms was produced by bombarding the four samples with 144 MeV C^{4+} and 180 MeV Ne^{6+} ions. The X-ray spectra were observed by means of high energy resolution X-ray spectroscopy, using the von Hamos spectrometer of Fribourg. The energies and natural line widths of the observed hypersatellites were determined and compared to existing experimental and theoretical values. For all investigated collisions the double-to-single K-shell ionization cross sections were derived from the measured hypersatellite-to-diagram line intensity ratios. The obtained values were compared to predictions from the Semi-Classical Approximation (SCA) model based on hydrogen-like and relativistic Hartree-Fock wavefunctions as well as to theoretical values obtained from Classical Trajectory Monte-Carlo (CTMC) calculations. A paper presenting the results of this second project is in preparation for *Physical Review A*.

CHAPTER II

ENERGIES AND WIDTHS OF ATOMIC CORE LEVELS IN LIQUID MERCURY

II.1 Introduction

Mercury is the only common metal liquid at room temperature. It has been widely used in the past in laboratory work for making thermometers, barometers, diffusion pumps, Hg-vapor lamps and advertising signs, mercury switches and other electrical devices. Pesticides, dental preparations, batteries and catalysts are further examples of the use of the versatile liquid metal in everyday life. However, mercury is also known as a virulent poison that is readily absorbed through the respiratory and digestive tracts. It acts as a cumulative poison since only small amounts can be eliminated at a time by the human organism. Furthermore, since Hg is a very volatile element, dangerous levels are easily attained in air. The danger is still increased by the colorless and odorless nature of the Hg vapor. Because mercury wastes have not been always eliminated properly in the past decades, this dangerous metal has spread out and accumulated in nature. As a consequence the toxic element has received a renewed interest in the recent years and mercury pollution has become an important field in environmental studies.

Among the methods employed to detect traces of mercury, the X-ray fluorescence (XRF) and particle-induced X-ray emission (PIXE) techniques are probably the most efficient ones. In these techniques, the concentrations of the elements of interest are usually determined from the relative yields of the sample K X-ray lines. Energies of the latter have thus to be known accurately to identify unambiguously the observed transitions. In in-situ XRF analysis of Hg-contaminated samples, portable X-ray sources characterized by high-voltages limited to 40-60 kV are employed that restrict the observation to the L X-ray emission of mercury. In this case, a correct and reliable analysis of the complex L X-ray spectrum in which many transitions are overlapping is only possible if the energies of the Hg L X-ray transitions are known with an accuracy of about 1 eV. In the XRF and PIXE methods, the knowledge of the line shapes of the measured X-ray transitions represents an additional important asset to improve the precision and reliability of the results even in low-resolution measurements [29]. Actually, as the line shapes of the observed X-rays result from the convolution of the instrumental response of the detector with the natural widths of the transitions, the latter have indeed to be known as accurately as possible to obtain correct intensities from the fits.

On the other hand, Hg is the heaviest stable element having all electronic subshells filled in the ground state. Precise experimental data concerning the transition energies and transition widths of mercury are therefore particularly adequate to probe the goodness of atomic structure calculations of heavy elements. However, as indicated by Deslattes *et al.* [30], for mercury the only existing data base for experimental X-ray transition energies is that of Bearden [31] which is almost 50 years old. Furthermore, as it was pointed out by Fuggle already in 1980 [32], a similar lack of experimental information does exist for the widths of the atomic core-levels of mercury. The situation has not much improved in the last two decades. In the recent inventory of atomic level widths made by Campbell and Papp [33] one can see indeed that for mercury experimental data are available only for the L_{1-3}-subshells [34] and the N_{4-7}-subshells [35, 36]. Here also there is thus a clear need for modern data for the widths of most Hg core-levels.

For the above-mentioned reasons we have performed a series of high-resolution X-ray emission spectroscopy (XES) measurements of liquid Hg. The transition energies and transition widths of a variety of K, L and M X-ray lines induced by means of photoionization were determined. As the energy, respectively the width, of an X-ray transition is given by the difference of the binding energies of the two atomic levels involved in that transition, respectively by the sum of the widths of the two levels, two sets of linear equations could be derived from the measured transition energies and transition widths. Solving the two systems of equations by means of a least-squares-fit method, two self-consistent sets of experimental electron binding energies and level widths could be obtained for most core-levels of liquid Hg.

II.2 Experiment

II.2.1 Experimental method

The measurements of the X-ray spectra were performed at the University of Fribourg by means of high-resolution X-ray spectroscopy. The K and most L X-ray lines were observed with a DuMond transmission-type bent crystal spectrometer [37]. As in the transmission geometry (Laue diffraction) the photon absorption due to the crystal thickness becomes very important at low-energy, the L transitions below 11 keV and the M transitions were measured with a von Hamos reflection-type bent crystal spectrometer (Bragg diffraction) [38]. As the energy domains covered by the two spectrometers are overlapping between 11 and 15 keV, the $L_2 - M_4$ transition (E = 11.8 keV) was measured with both instruments in order to make a cross-check of the obtained results and to probe the reliability of the quoted uncertainties.

For the production of the Hg fluorescence, the liquid target was irradiated with the Bremsstrahlung from commercial 3 kW Coolidge-type X-ray tubes. For the L X-ray transitions measured with the DuMond spectrometer a Au-anode X-ray tube equipped with a 1-mm thick beryllium window was employed. The tube was operated at 80 kV × 35 mA. The same tube was used for the $K\beta$ measurements but at 95 kV × 30 mA. The Hg $K\alpha_2$ and Au $K\alpha_1$ transitions being close in energy, a Cr-anode tube (95 kV × 30 mA) was employed for the measurement of the $K\alpha$ X-ray spectrum. For the low-energy measurements performed with the von Hamos spectrometer, the same Cr-anode tube was chosen because of its thinner beryllium window (0.5 mm). The tube was operated at 60 kV × 40 mA for both the L and M X-ray measurements.

II.2.2 Target

The same target cell was used for the DuMond and von Hamos measurements. It consisted of 99.999% pure liquid mercury enclosed in a small metallic cell with a Kapton^{TM} window serving as well for the irradiation of mercury as for the observation of the characteristic radiation of the latter. The different components of the target cell are presented in Fig. II.1.

The cell was made from a cast stainless steel rectangular prism whose front surface was milled to form a 30-mm high × 8-mm wide × 2-mm deep cavity. Stainless steel

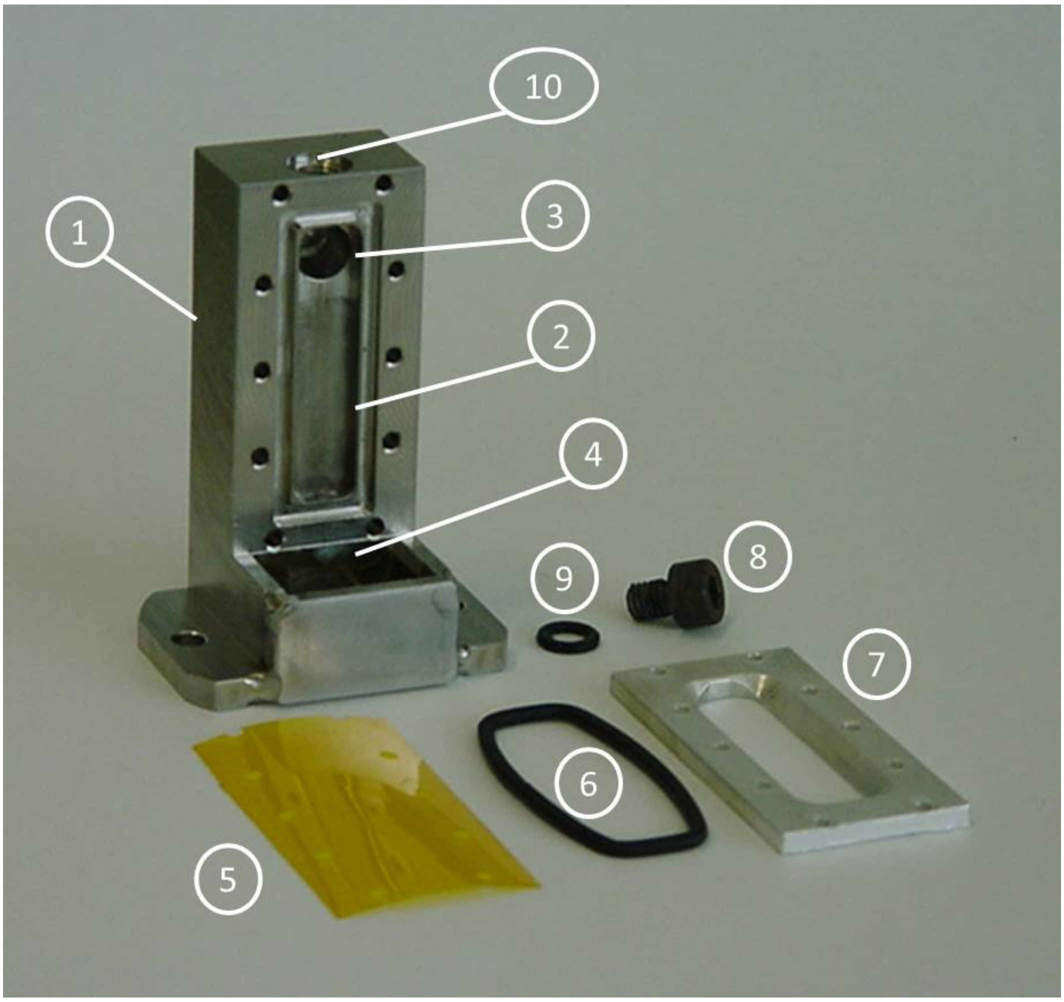

Figure II.1 – Dismantled Hg target cell. Shown are the cast stainless steel body (1), Hg reservoir (2), thermal expansion outlet (3), external security receptacle (4), Kapton^{TM} foil (5), sealing ring of the window (6), Al frame of the window (7), screw cap (8) with associated sealing ring (9) and filling aperture (10).

was chosen because it is one of the rare metals that do not react with mercury. The cavity was then covered with a thin Kapton^{TM} foil, using an aluminium frame and a sealing ring to make the small reservoir mercury-tight. For safety reasons, all measurements were performed with a 75 μm-thick Kapton^{TM} window, except the M X-ray measurements for which a 8 μm-thick Kapton^{TM} foil was used in order to minimize the absorption of the 2.2 keV M X-rays through the Kapton^{TM} window. To take into account the thermal expansion of the irradiated Hg, a circular outlet was drilled in the top part of the cavity. In addition, a small receptacle was designed at the bottom of the target mount to prevent mercury from spreading thoughout the entire target chamber in case of tearing of the Kapton^{TM} window.

To allow the target cell to be filled or drained off, a small circular hole was drilled between the top part of the cavity and the outside. After filling up with Hg, the hole was sealed with a screw cap and a tiny sealing ring.

II.2.3 DuMond spectrometer

The DuMond crystal spectrometer of Fribourg [37] consists mainly of a target chamber, a bent crystal plate that can be rotated around a vertical axis by ± 20° and a self-propelled detector-collimator system. The latter can move on a 4.5 m-long circular track by means of two conical stainless steel rollers, permitting the detector and collimator to be rotated by ± 40°. During acquisition, the detector-collimator system is automatically aligned on the double Bragg angle by means of an optical tracking system. The axes of rotation of the crystal and detector are separate but aligned vertically. The distances between the target and the bent crystal and between the crystal and the detector are 3.1 m and 2.9 m, respectively. The instrument is therefore rather big, occupying a volume of approximately $7 \times 4 \times 2$ m^3. To minimize the absorption of the measured X-rays in air, two evacuated pipes are installed between the target chamber and the crystal and between the crystal and the front of the collimator. The design, working principles and performances of the spectrometer are presented in more details in [37]. A side view of the instrument is depicted in Fig. II.2.

For the present project the DuMond spectrometer was operated in the so-called modified slit-geometry (see Fig. II.3). In this geometry the sample is viewed by the crystal through a narrow rectangular slit located on the Rowland circle, a few cm in front of the target. For X-ray measurements, this geometry presents several advantages with respect to the standard DuMond geometry. In particular the slit-geometry makes possible the use of extended radiation sources. This is an important asset when measuring gaseous [12,39] or liquid samples. Furthermore, it permits one to get rid of the systematic errors originating from the thermal deformation of the irradiated sample and to enhance the luminosity of the spectrometer by diminishing the self-absorption of the fluorescence X-rays in the target. The 30-mm high rectangular slit is made of two vertical 5-mm thick juxtaposed Pb plates. For the present measurements a slit width of 0.15-mm was employed. The Hg sample was oriented so that the angle between the normal to the Kapton^{TM} window of the target cell and the normal to the window of the X-ray tube was 24°. This angle was chosen as a compromise between two opposing effects influencing

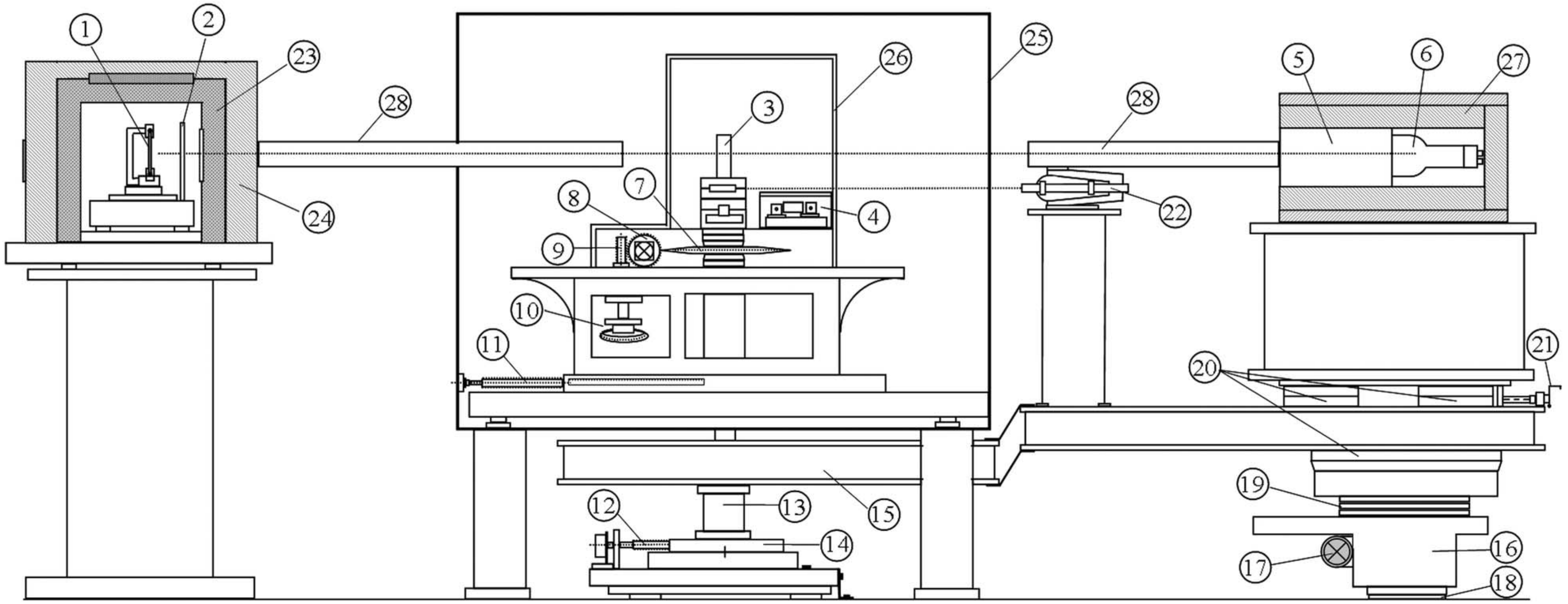

Figure II.2 – Side view of the DuMond crystal spectrometer (taken from Ref. [37]) with (1) target, (2) slit, (3) crystal, (4) optical laser interferometer, (5) Soller slit-collimator, (6) detector, (7) large tooth wheel, (8) small tooth wheel and second worm gear (behind), (9) first worm gear, (10) step motor for the crystal rotation, (11) screw rod for the crystal focusing, (12) screw rod for the detector axis focusing, (13) detector rotation spindle, (14) movable table of the detector rotation spindle, (15) detector rotation arm, (16) detector automotive carriage, (17) step motor of the detector carriage, (18) circular rail, (19) large ball bearing, (20) Schneeberger minirails, (21) manual adjustment of the collimator position, (22) laser of the detector position optical tracking system, (23) target chamber, (24) lead shielding, (25) external thermostatic housing, (26) internal thermostatic housing, (27) lead shielding, (28) evacuated pipe.

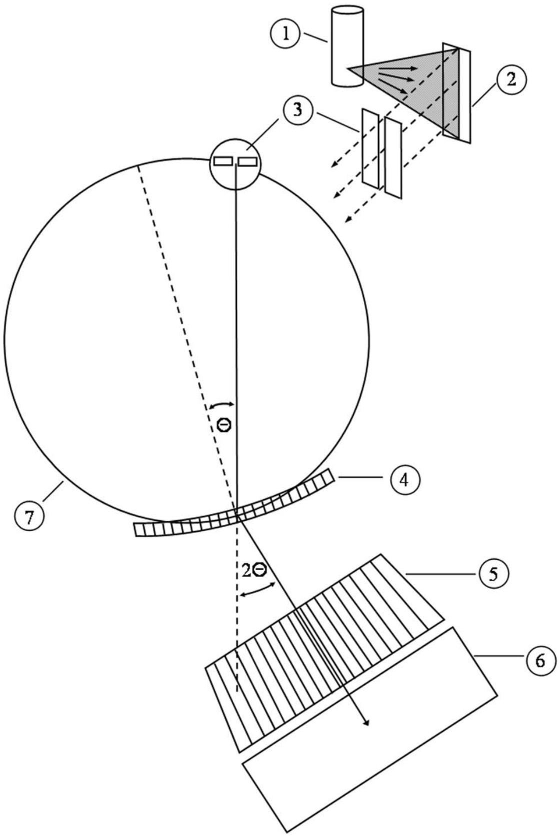

Figure II.3 – Schematic view of the so-called modified DuMond slit geometry (not to scale). The slit (3) is located on the Rowland circle (7) and acts as the effective photon source. The target (2) is irradiated with the Bremsstrahlung from the X-ray tube (1). The curved cristal (4) is placed in front of the soller-slit collimator (5) and detector (6). The radius of curvature of the crystal is twice that of the Rowland circle.

the intensity of the measured fluorescence radiation, namely the area of the target surface seen by the crystal through the narrow slit and the self-absorption of the fluorescence X-rays in the target.

The rotation of the crystal is performed via a two-stage tooth wheel-worm gear mechanism driven by a stepping motor. With this mechanism, minimum angular steps of 0.075 arcsec can be performed with a maximum angular speed of about 1.7° per minute. The non-linearity of the driving mechanism does not exceed 5 arcsec over the entire angular domain of ± 20°. The Bragg angles are measured by means of a Doppler effect-based laser interferometer with a precision of a few milliarcsec [40]. The rotation mechanism of the crystal is enclosed in a thermostatic housing in which the temperature is maintained constant within ± 0.1 C, whereas the bent crystal lamina and laser interferometer are enclosed in a second smaller housing where the temperature fluctuations are kept smaller than 0.03 C by means of Peltier elements. In the DuMond geometry the crystal plate is bent cylindrically and the radius of curvature is twice that of the focal circle. For this project a 10 × 10 cm^2 (110) quartz crystal plate with a thickness of 0.5 mm was employed. The plate was bent to a radius of 311 cm by means of a clamping block similar to the one described in [41]. Due to the window width of the clamping block and because the top and bottom parts of the crystal which were poorly curved as a result of the Sumbaev effect [42] could not be used, the effective diffracting area of the crystal was 12 cm^2. The corresponding solid angle of the DuMond spectrometer was thus about 1.2×10^{-4} sr.

For the Hg project a 5 inches diameter Phoswich scintillation counter was employed for the detection of the diffracted X-rays. The latter consists of a thin (0.25 in.) NaI(Tl) crystal followed by an optically coupled thicker (2 in.) Cs(Tl) crystal. Both crystals are mounted on the same photomultiplier tube. As the rising times of the signals are different for the two crystals, the events corresponding to each scintillation can be identified by a pulse-shape analysis [43]. This type of detector permits to strongly diminish the background arising from high-energy photons, which is an important asset when weak X-ray lines have to be extracted from the background [9, 11, 13]. A further reduction of the background was obtained by enclosing the Phoswich detector in a heavy Pb-Cu-Al shielding, and by sorting on-line the events of interest as a function of their energy. The Soller-slit collimator placed in front of the detector consists of 24 parallel rectangular slits that are 660-mm long, 110-mm high and 2-mm wide. The collimator has a trapezoidal angular response with a plateau length of about 130 arcsec and a transmission coefficient of 51%.

The angular instrumental response of the DuMond spectrometer depends principally on the slit width and on the precision of the crystal curvature but not, at least in first approximation, on the Bragg angle. In general, the response can be well reproduced by a Gaussian function. The angular instrumental resolution was determined by measuring the $K\alpha_1$ transitions of Gd and Au, in first and fourth orders of diffraction, respectively, using in the fits the level widths quoted by Campbell and Papp [33] to derive the Lorentzian widths of the two transitions. From the fits in which the Lorentzian widths were kept fixed, consistent FWHM Gaussian widths of 12.8(7) arcsec (Gd) and 12.9(1.6) arcsec (Au) were found.

The energy resolution Γ_E can be deduced from the angular resolution Γ_ϑ using the following relation :

$$\Gamma_E = \cot(\vartheta) \cdot E \cdot \Gamma_\vartheta \tag{II.1}$$

where ϑ is the Bragg angle and E represents the photon energy. As shown by equation II.1, for a given photon energy, Γ_E improves with increasing Bragg angles. For this reason the K X-rays were measured in second order of diffraction. The variation of the energy resolution versus the photon energy is depicted in Fig. II.4. One sees that for the L X-ray measurements the resolution of the DuMond spectrometer varied between 3 eV at 11 keV and 5.5 eV at 15 keV, whereas for the K X-ray measurements the resolution was markedly worse, ranging from 46 eV at 65 keV to 80 eV at 85 keV.

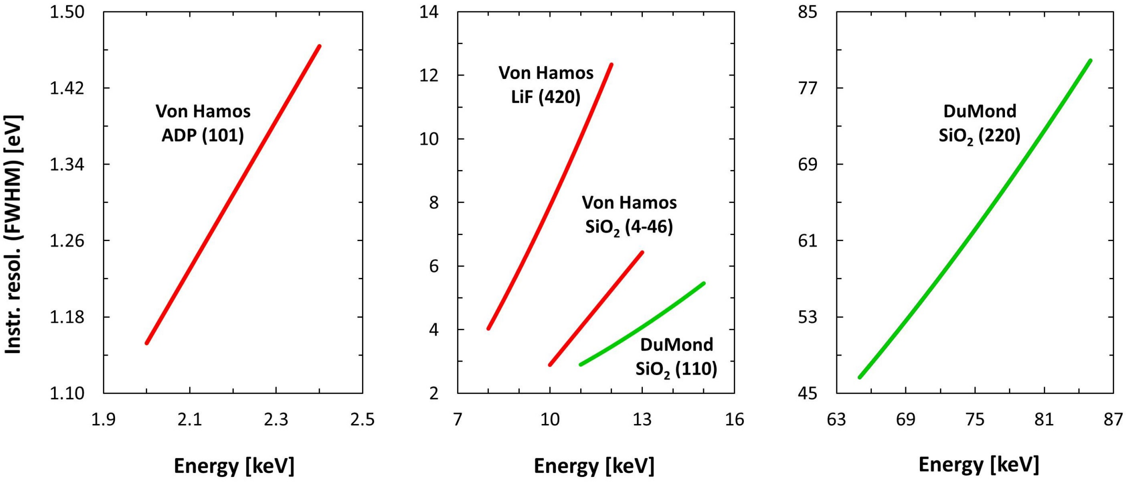

Figure II.4 – Variation of the FWHM instrumental resolution of the von Hamos and DuMond spectrometers as a function of the X-ray energy. The energy-dependent instrumental broadening is shown for the energy domains corresponding to the measured M transitions (left pannel), L transitions (mid pannel) and K transitions (right pannel).

In the DuMond geometry the crystal-to-slit distance (focal length f) corresponding to the best instrumental resolution varies with the photon energy, i.e., the Bragg angle ϑ:

$$f = R \cdot \cos\vartheta \tag{II.2}$$

where R is the radius of curvature of the crystal. As a consequence the focal length f should be adjusted for each X-ray line. However, when the X-ray spectrum extends over a large angular range and comprises many weak lines, this optimization is not so convenient. It is indeed simpler to measure a selected group of lines with an average value of the focal length and to correct then off-line the instrumental broadenings for the tiny deviations resulting from the focal length errors [6]. For this reason the variation of the instrumental broadening as a function of the focal length was determined by measuring the $K\alpha_1$ line of Gd at several different focusing distances around the optimum value.

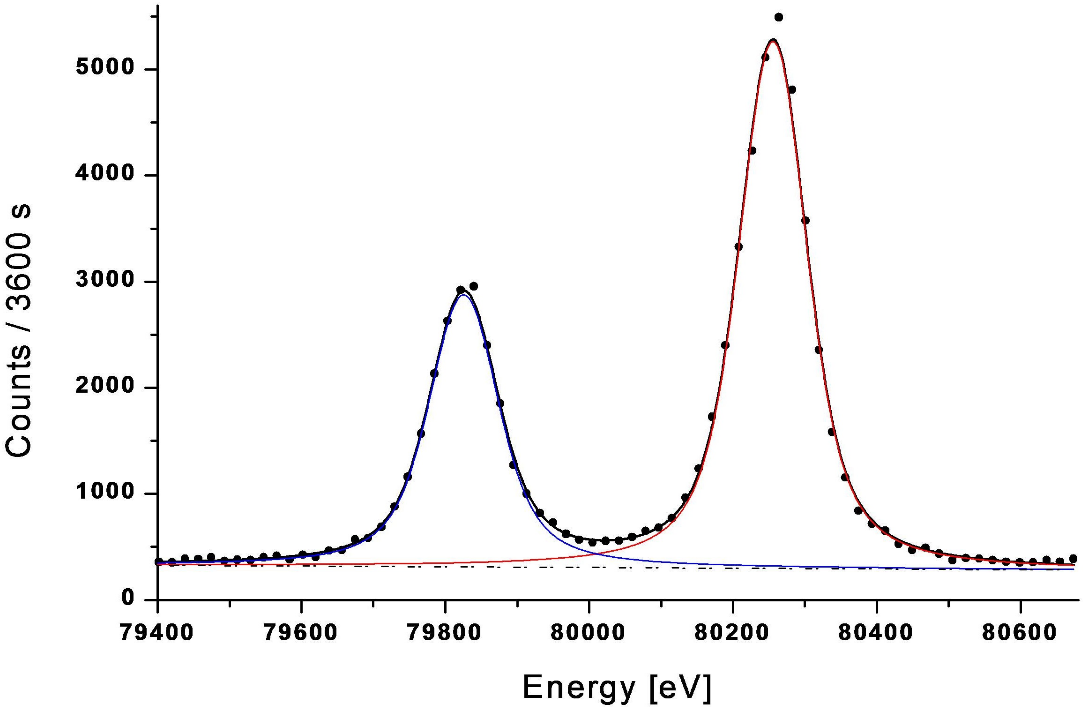

Figure II.5 – High-resolution K-$M_{2,3}$ X-ray spectrum of Hg measured with the DuMond spectrometer. As shown, the two components of the fine structure doublet are well resolved.

To calibrate in energy the angular spectra measured with the DuMond spectrometer, the crystal lattice spacing constant and the zero of the Bragg angle scale must be known accurately. The lattice constant of the $SiO_2(110)$ crystal employed in the present project was determined by measuring the $K\alpha_1$ transition of Au in 4^{th} order on both sides of diffraction. Using the so-determined double Bragg angle 2ϑ and the wavelength of the Au $K\alpha_1$ transition reported in [44, 45], the value $d_{110} = 2.456645(20)$ Å was obtained. As the K X-ray measurements were performed about two years later the lattice constant was re-determined at the end of these measurements, using again the $K\alpha_1$ transition of Au but this time in 2^{nd} order of diffraction. A somewhat bigger value of 2.456705(19) Å was obtained. As no explanation was found for this small but significant discrepancy, we opted to use the average value of the two measurements and for the uncertainty the half of the difference between the two values, i.e. $d_{110} = 2.456675(30)$ Å . Finally, as the zero Bragg angle may vary with the focal length f, it was determined for each group of lines observed at the same value of f by measuring the most intense transition of the group at positive and negative Bragg angles.

With the DuMond spectrometer, data collection is carried out point by point. In other words, the angular spectrum is scanned step by step with the same acquisition time for each angular position of the crystal. If the measured X-ray spectrum comprises weak lines, acquisition times up to thousand seconds per point or even more are not exceptional so that the measurement may last several days. In order to minimize the systematic errors related to long-term instabilities of the experimental setup (e.g. fluctuations of the X-ray tube intensity) such angular regions were measured in several successive step-by-step scans that were then summed together off-line. For illustration, two high-resolution X-ray spectra of mercury measured with the DuMond spectrometer are shown in Figs. II.5 and II.8.

II.2.4 Von Hamos spectrometer

The $M_4 - N_6$, $M_5 - N_7$, $L_3 - M_5$, $L_3 - M_4$, $L_3 - M_1$ and $L_2 - M_1$ transitions whose energies are smaller than 11 keV were measured with a von Hamos Bragg-type curved crystal spectrometer. Furthermore, as indicated before the strong $L_2 - M_4$ transition was observed with both the von Hamos and DuMond spectrometers to probe the precision and consistency of the two independent measurements.

The von Hamos spectrometer consists of three main components : a target-slit mechanism, a bent crystal and a position-sensitive detector. The crystal is bent cylindrically around a horizontal axis parallel to the direction of dispersion and provides focusing in the vertical direction. The front surface of the detector, the slit axis and the axis of curvature are all contained in the same vertical plane. The von Hamos geometry permits at one position of the three spectrometer components data collection over an energy interval that is limited by the horizontal extension of the detector. To cover a greater energy domain the central Bragg angle is adjusted by displacing the crystal and detector along axes which are parallel to the direction of dispersion. The slit-to-crystal and crystal-to-detector distances are both varied but kept equal. The crystal and the detector are moved by means of remote-controlled stepping-motors with a precision of 5 μm. Their actual position is determined using two optical devices with an accuracy of 1 μm. The target-slit mechanism, crystal and detector are shown in Fig. II.6. They are enclosed in a 180-cm long × 62-cm wide × 25-cm high vacuum chamber that can be pumped

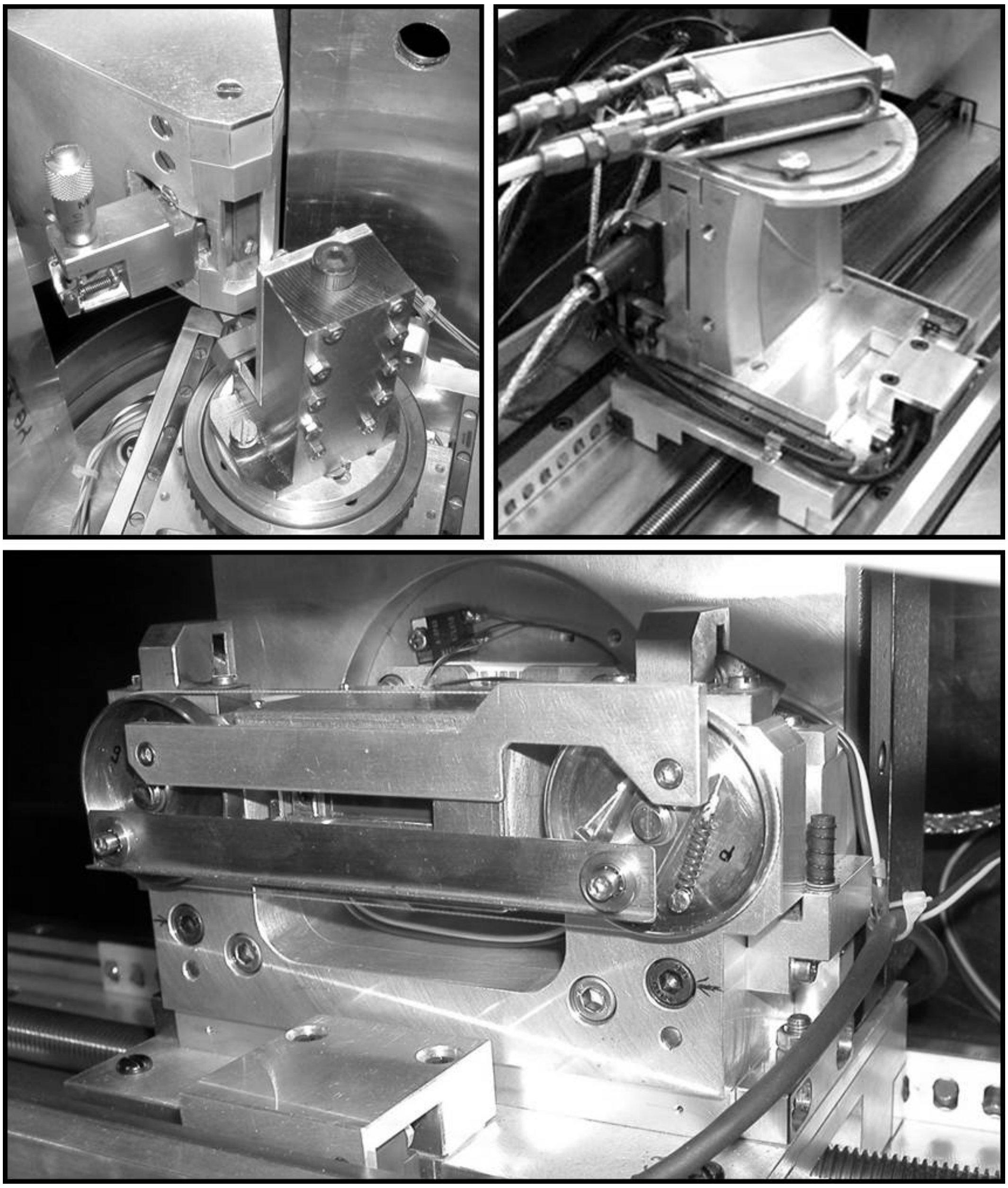

Figure II.6 – Photographs showing the three main components of the von Hamos spectrometer : the rear part of the Hg target placed in front of the slit with the micrometer-screw used to adjust the slit-width (top left panel), the bent crystal glued on its concave aluminium support (top right panel), and the CCD camera with the remote-controlled X-ray shutter (bottom panel). The screw-rods serving to move the crystal and the CCD detector along the dispersion axis are also visible (top right and bottom pannels). The device mounted on the top of the crystal support is a photodiode detector used to monitor the beam intensity in heavy-ion and synchrotron radiation experiments.

down to about 10^{-6} mbar by means of a turbo-molecular pump.

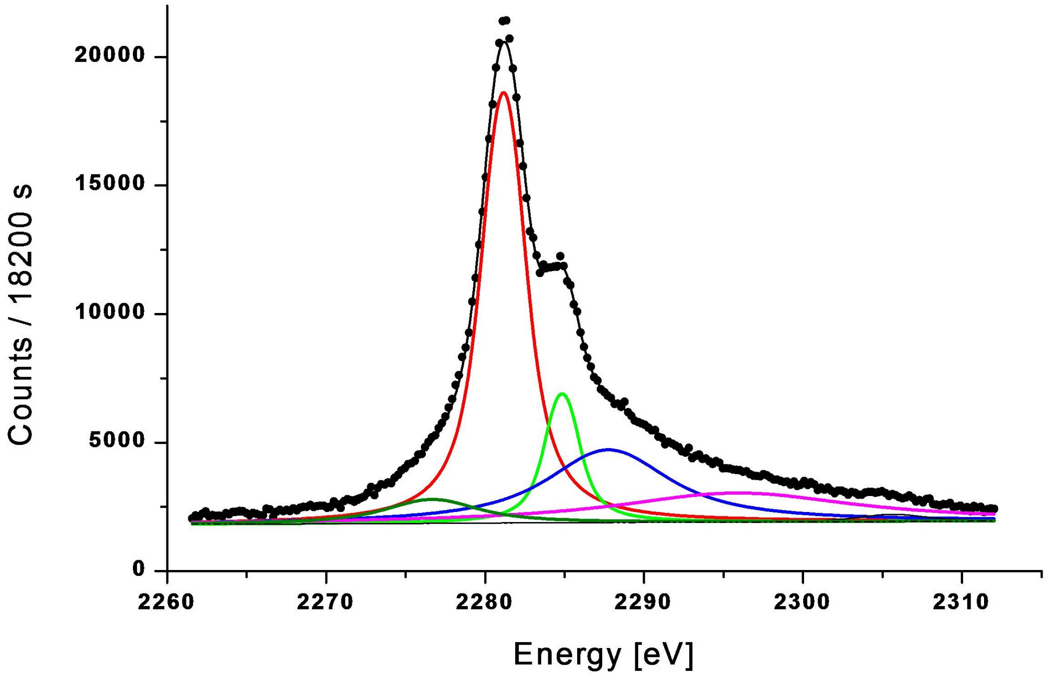

Figure II.7 – Hg $M_4 - N_6$ transition measured with the von Hamos spectrometer. The complex N-satellite structure was fitted with three Voigtians (green, blue and violet lines). The olive line around 2275 eV accounts for the slight asymmetry observed in the instrumental response of the von Hamos spectrometer when equipped with the ADP (101) crystal. The line at about 2305 eV was assigned to residuals from the sixth order diffraction of the $L_2 - M_4$ transition.

The von Hamos geometry requires that the X-ray source viewed by the crystal is kept fixed on the curvature axis. Thus the slit location remains unchanged but the position of the target behind the slit must be adjusted as a function of the Bragg angle. In order to maximize the count rate in the detector the target orientation around a vertical axis can also be adjusted. The optimizations of the target position and target orientation are remote-controlled by means of two stepping-motors. Furthermore, the target displacement and the orientation of the slit around its vertical axis are mechanically correlated so that the slit is always perpendicular to the target-to-crystal direction. The rectangular slit is made of two vertical juxtaposed 0.3-mm thick Ta plates. More details about the spectrometer design and its operational characteristics can be found in [38].

For the present project a slit width of 0.25 mm was employed. For each measurement the orientation of the Hg target was chosen so that the angles between the normal to the front surface of the target and the direction of the ionizing radiation, respectively the target-to-crystal direction, were equal. As the Bragg angles covered by the von Hamos spectrometer range between 24.4° and 61.1°, three different crystals were needed. The L_3 X-ray lines were measured with a LiF(420) crystal (2d = 1.8010 Å), the M-rays with an ADP(101) crystal (2d = 10.642 Å), whereas the $L_2 - M_4$ transition was observed in second order, using a $SiO_2(2\bar{2}3)$ crystal (2d = 2.7500 Å). The three crystal plates are 10-cm high and 5-cm wide with thiknesses of 1.1 mm (LiF), 0.3 mm (ADP) and 0.4 mm (SiO_2). They are glued on aluminium blocks machined to concave cylindrical surfaces with radii of 25.4 cm.

The diffracted X-rays were detected with a deep-depleted Charge-Coupled-Device (CCD) camera (depletion depth of 50 μm) consisting of 1024 pixels in the direction of dispersion and 256 pixels in the vertical direction with a pixel resolution of 27 μm in both directions [46] The CCD chip was thermoelectrically cooled down to -60 C. For each measurement several thousands of two-dimensional images were collected. The latter were filtered off-line, setting appropriate energy windows to sort the pixels corresponding to good events. The filtered images were then added together and the sum-image projected on the dispersion axis to obtain the one-dimensional position spectrum, i.e., the energy spectrum. For illustration the spectrum corresponding to the $M_4 - N_6$ transition is depicted in Fig. II.7.

The one-dimensional position spectra were calibrated in energy using photoionization measurements of the $K\alpha_1$ and $L\alpha_1$ transitions of several mid-heavy elements. For the calibration of the spectra measured with the LiF(420) and $SiO_2(2\bar{2}3)$ crystals, the $K\alpha_1$ transitions of Zn, Ge, Se and Br were employed, whereas for the calibration of the spectra measured with the ADP(101) crystal the $L\alpha_1$ transitions of Nb and Mo were used. The energies of the six calibration transitions are given as footnotes in Table II.1 (see Sect. II.4). They were derived from the wavelengths reported by Bearden [31]. Since the latter values are given in the Å* scale, they were corrected by the conversion factor 1.0000150 Å*/Å and then converted to energies using the energy-wavelength product $V\lambda = 12.398419$ keVÅ. The two conversion factors were computed using for the Planck constant h, speed of light c and elementary charge e the values recommended in 2006 by the Committee on Data for Science and Technology (CODATA) [47]. Furthermore, the uncertainties quoted by Bearden being probable errors (50% confidence limits), they were multiplied by 1.48 to obtain standard deviation errors (67% confidence limits).

The instrumental broadening of the von Hamos spectrometer originates mainly from the slit width, the mosaicity and Darwin width of the crystal and the spatial resolution of the detector. The broadening due to the slit is given by:

$$\Delta E_{slit} = \frac{w_{slit}}{2R} \cdot \cos(\vartheta) \cdot E \tag{II.3}$$

where w_{slit} represents the width of the slit, R the crystal radius of curvature, ϑ the Bragg angle and E the energy of the measured transition. Similarly the broadening resulting from the spatial resolution of the detector can be written as:

$$\Delta E_{CCD} = \frac{w_{pixel}}{4R} \cdot \sin(2\vartheta) \cdot E \tag{II.4}$$

where w_{pixel} stands for the size of the CCD pixels in the direction of dispersion. From the above relations, one finds that for the M and L X-ray lines measured with the von Hamos spectrometer the broadening related to the slit (width of 0.25 mm) ranged between 0.9 eV and 4.0 eV, whereas the detector contribution varied between 0.05 eV and 0.31 eV, only. The 27 μm resolution of the CCD detector was thus not really needed and a software binning of four adjacent columns was performed off-line in order to obtain higher count rates in the one-dimensional position spectra.

The instrumental broadening of the von Hamos spectrometer was determined experimentally, using the above-mentioned $K\alpha_1$ and $L\alpha_1$ calibration measurements. It was found that for the three crystals the instrumental response could be well reproduced by a Gaussian function. The full widths at half maximum (FWHM) of the three Gaussians were obtained from the fits of the calibration measurements in which the natural Lorentzian widths of the transitions were kept fixed at the values derived from the atomic level widths quoted in the Tables of Campbell and Papp [33]. The variation of the instrumental resolution with the photon energy is shown for the three crystals in Fig. II.4. One can see that for the energy corresponding to the $L_2 - M_4$ transition (11.8 keV) the resolution obtained with the $SiO_2(4\bar{4}6)$ crystal (5 eV) was markedly better than the one obtained with the LiF(420) crystal (12 eV). Since the slit and detector contributions to the broadening are about equal for the two crystals, the observed resolution difference indicates that the mosaicity character of the LiF crystal is more pronounced, i.e., that the angular distribution of the crystallites is significantly broader in the LiF crystal than in the SiO_2 one. From Fig. II.4 one can also see that in the 11-15 keV overlapping energy region the resolution of the von Hamos spectrometer, even when using the $SiO_2(4\bar{4}6)$ crystal, is somewhat worse than the one of the DuMond spectrometer, justifying thus the choice of the transmission-type instrument for the measurement of the *L* X-ray transitions occurring above 11 keV.

II.3 Data analysis

II.3.1 Fitting procedure

The transitions observed with the DuMond spectrometer were divided into twelve groups. Transitions belonging to the same group were measured at the same focal length. Similarly the transitions observed with the von Hamos spectrometer were divided into six groups corresponding to the six different positions of the crystal and CCD camera at which the data were collected. Each group was analysed separately by means of the least-squares-fitting software package MINUIT [48]. Since the widths of the Gaussian instrumental responses of the two spectrometers were similar or narrower than the widths of the Lorentzian functions corresponding to the line shapes of the X-ray transitions, Voigt profiles that result from the convolution of Lorentz and Gauss functions were employed to reproduce the line shapes of the measured transitions [49]. The energies, intensities and Lorentzian widths of the transitions as well as the two parameters of the linear background were let free in the fitting procedure, whereas the Gaussian widths were kept fixed at their known values. However, in several cases, some additional constraints needed to be set. For instance, in the analysis of the $K\beta_2$ spectrum, the intensity ratio of the $K-N_2$ and $K-N_3$ transitions and the energy separation between the two components had to be kept fixed. The intensity ratio was deduced from the Tables of Scofield [50] and the energy difference from the average values of the N_2 and N_3 subshell binding energies quoted in Refs [32] and [35]. Similar constraints were applied to the fits of the $L_1-N_{4,5}$, $L_1-O_{2,3}$, $L_3-N_{6,7}$ and $L_3-O_{4,5}$ doublets.

Typical examples of the difficulties encountered during the data analysis are illustrated by the spectrum shown in Fig. II.8. This spectrum was measured with the DuMond spectrometer (group 9). The three lines that clearly emerge from the background correspond, in the direction of increasing energies, to the L_1-N_2 (at about 14160 eV), L_2-O_4 and L_1-N_3 transitions. The weaker structure around 14100 eV was assigned to the L_2-O_1 and L_2-N_6 transitions. The asymmetry occurring on the high-energy flank of the L_2-O_4 transition is due to unresolved N-satellite structures originating from L_1L_2N Coster-Kronig transitions. Finally, the small excess of intensity visible around 14300 eV corresponds to the elastic scattering by the Hg target of the L_1-O_2 and L_1-O_3 transitions of Au from the characteristic emission of the X-ray tube anode. In addition to the problems related to the large number of transitions appearing in that energy region and the overlap of some of these transitions, a further difficulty we had to face concerned the presence in the spectrum of the L_2 edge of Hg (at 14209 eV). The line shapes of the $L_2 - O_4$ and $L_1 - N_3$ were indeed found to be affected by this edge as a result of the abrupt change of the self-absorption of the photons of interest in the target. Thus, at first, the spectrum was corrected to account for the variation of the self-absorption, using a theoretically constructed profile to reproduce the shape of the L_2 edge. The amplitude of the correction was adjusted so that the relative yields of the $L_1 - N_2$ and $L_1 - N_3$ transitions that lie respectively below and above the L_2 edge were consistent with the relative intensities reported by Scofield [50]. The corrected spectrum was then fitted, using one Voigtian for each of the seven transitions mentioned above. No constraint was set except for the $L_2 - O_4$ N-satellite whose energy and width were fixed at values derived from the fit of the $L_3 - O_5$ N-satellite (group 4) which could be resolved. The errors induced on the energies and widths of the $L_2 - O_4$ and $L_1 - N_3$ transitions by this crude approximation were probed and found to be small because of the weak relative intensity of the $L_2 - O_4$ N-satellite (about 6%).

To improve the poor statistics observed for the $L_2 - O_1$ and $L_2 - N_6$ transitions, the energy region between 14050 and 14135 eV was remeasured in several successive scans corresponding to a total collecting time of 4 hours per point (see inset of Fig. II.8). This region was fitted separately with four Voigtians, two for the diagram transitions plus one for the $L_2 - N_7$ transition (thin solid line in the inset, at 14110 eV) and one for the $L_2 - O_1$ N-satellite (dotted line). As shown by the inset, the four lines are superimposed on the low-energy tail of the stronger $L_1 - N_2$ transition whose position and width were kept fixed, using the values obtained from the fit of the full spectrum. The intensity, however, was let free to permit a better adjustment of the intensity scale of the two spectra. The energy separation between the $L_2 - N_7$ and $L_2 - N_6$ transitions was deduced from the difference between the binding energies of the subshells N_6 and N_7 quoted in Ref. [32] and fixed at that value. Similarly the difference between the level widths of the subshells N_6 and N_7 deduced from [35] was used to adjust the natural line width of the $L_2 - N_7$ transition to the one of the $L_2 - N_6$ transition. Finally the width and energy shift of the $L_2 - O_1$ N-satellite were also fixed, using again the values obtained from the fit of the resolved $L_3 - O_5$ N-satellite.

The spectra measured with the von Hamos spectrometer were analyzed in a similar

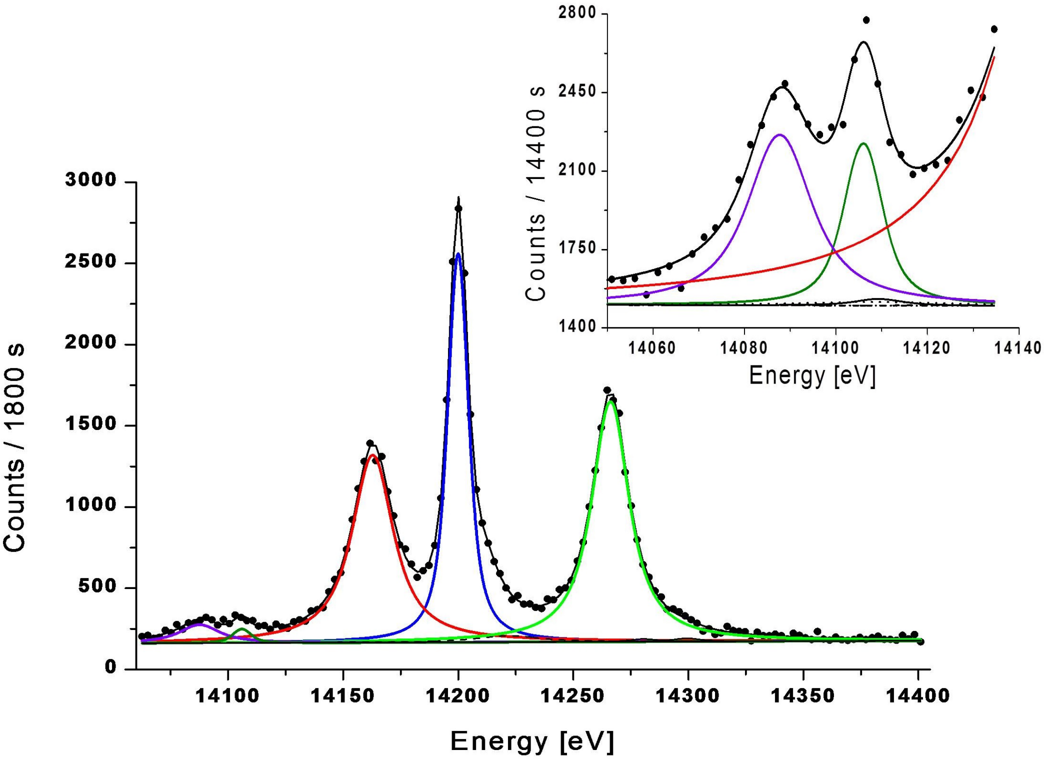

Figure II.8 – Part of the Hg L X-ray spectrum measured with the DuMond spectrometer. The spectrum was corrected for the L_2 absorption edge occurring at 14209 eV. The three main lines correspond to the $L_1 - N_2$ (red line), $L_2 - O_4$ (blue line) and $L_1 - N_3$ (green line) transitions. The low energy part of the spectrum around 14100 eV was remeasured with a longer acquisition time. It is shown enlarged in the inset where one can distinguish the $L_2 - O_1$ (violet line) and $L_2 - N_6$ (dark-green line) transitions as well as the weak $L_2 - N_7$ transition (solid line at 14110 eV) overlapping with the $L_2 - O_1$ N-satellite structure (dotted line). The dotted line at about 14220 eV (in the main figure) corresponds to the N-satellite of the $L_2 - O_4$ transition. The hardly visible components around 14280 eV and 14300 eV, respectively, correspond to the $L_1 - O_2$ and $L_1 - O_3$ transitions of Au. The latter are due to the elastic scattering by the target of the characteristic X-ray emission from the X-ray tube anode.

way. An example is presented in Fig. II.7 showing the $M_4 - N_6$ transition. The latter could be well fitted with a single Voigt profile. The small component fitted below the main line is due to the ADP (101) crystal. The same asymmetry was indeed observed in the $L\alpha_1$ transitions of Nb and Mo employed for the calibration of the spectrometer. The broad and intense structure on the right corresponds to N-satellite X-ray lines originating from $M_{1,2,3}M_4N$ Coster-Kronig transitions.

This structure could be well reproduced with one narrow and two broad juxtaposed Voigt profiles. All parameters were let free in the fit except the relative position and relative intensity of the line accounting for the asymmetry of the crystal response which were fixed at the same values as the ones obtained from the fits of the calibration lines. One could be tempted to assign the narrow profile at about 2285 eV to the $M_4 - N_7$ transition, the fitted energy shift of 3.8 eV relative to the $M_4 - N_6$ transition being consistent with the binding energy difference between the $4f_{5/2}$ and $4f_{7/2}$ levels. However, although no information could be found in the literature about the strength of the $M_4 - N_7$ transition, the latter is expected to be very weak because forbidden by the selection rule $\Delta j = 0, \pm 1$, which is in contradiction with the relatively strong intensity found for this line. The latter was thus assigned, as mentioned before, to N-satellite structure of the $M_4 - N_6$ transition.

II.3.2 Satellite X-ray lines

As a result of $L_1 L_{2,3} M$ and $L_1 L_{2,3} N$ Coster-Kronig transitions, L_1^{-1} single-vacancy states may be transformed to $L_{2,3}^{-1} M^{-1}$ and $L_{2,3}^{-1} N^{-1}$ double-vacancy states. Such two-hole states may also be created via M- and N-shell shake processes [51, 52] as a consequence of the sudden change of the atomic potential following the L-shell photoionization. However, shakeup and shakeoff processes resulting from L-shell photoionization are characterized by very weak probabilities and can thus be neglected with respect to Coster-Kronig transitions. The radiative decay of double-vacancy states giving rise to satellite X-ray lines, satellite structures are in general present in L_2 and L_3 X-ray spectra. On the contrary, in photoinduced L_1 X-ray spectra only diagram transitions corresponding to the radiative decay of single vacancy states are observed. The same holds for the M_4 and M_5 X-ray spectra in which strong N-satellite structures are usually observed as a result of $M_{1,2,3} M_{4,5} N$ Coster Kronig transitions (see, e.g., Fig. II.7).

Satellite X-ray lines are slightly shifted in energy relative to their parent diagram lines. In general, the energy shifts are positive and decrease with the principal quantum number of the spectator vacancy. As a consequence, for $L_{2,3}$ transitions, satellites corresponding to M-shell spectator vacancies can be separated from their parent diagram lines, but satellites corresponding to N-shell spectator vacancies are usually not resolved, the energy shifts being smaller in this case than the natural widths of the transitions. However, the energy shift of a satellite increasing with the principal quantum number of the transition electron, for $L_{2,3}$ transitions involving electrons from outer orbitals such as, e.g., $L_{2,3} - O$ transitions, N-satellites can again be resolved, provided a detector with a high enough resolution is employed. Finally, energy shifts induced by spectator vacancies located in the outer O- and P-shells are so small that the corresponding X-ray satellite lines have practically no noticeable effect on the line shapes of the parent diagram transitions.

For mercury, L_1L_2M Coster-Kronig transitions are energetically forbidden but $L_1L_2N_{3-7}$, $L_1L_3N_{1-7}$ and $L_1L_3M_{4,5}$ transitions are allowed. The line shapes of L_2 and L_3 X-ray transitions may thus be affected by unresolved N-satellites. In principle, M-satellites of L_3 transitions are less problematic for the data analysis since they can be resolved. However, due to the rather high density of lines characterizing L X-ray spectra, the M-satellites may overlap with other close-lying diagram lines. In such cases the energies and widths of the overlapping diagram transitions may be affected by sytematic errors if the M-satellites are not considered in the analysis. For these reasons we have determined the centroid energies and theoretical shapes of the M-satellites corresponding to the $L_3 - M_{1,4,5}$ and $L_3 - N_{1,4,5}$ transitions. Similar calculations were performed for the N-satellites of the $L_2 - M_{1,4}$, $L_2 - N_{1,4,6}$, $L_3 - M_{1,4,5}$ and $L_3 - N_{1,4,5,7}$ transitions. Results of these calculations were then employed in the data analysis to identify the observed transitions and to fit correctly the diagram transitions in the cases of unresolved N-satellites or overlapping M-satellites.

The line shape of a particular $j_1j_2(J) \rightarrow j_3j_2(J')$ satellite transition was constructed by computing numerically the sum of all components pertaining to the considered transition. In the above notation, j_1 and j_3 represent the angular momentum of the transition hole in the initial state (total angular momentum J) and final state (total angular momentum J') and j_2 the angular momentum of the spectator vacancy. The sum was calculated over all (J,J') values permitted by the selection rule ΔJ=0,±1. A Voigtian profile of energy E, Lorentzian width Γ and relative intensity I_{rel} was attached to each component. The energies of the different satellite components were derived from the experimental energy of the parent diagram transition and the energy shifts quoted in Ref. [53]. All components were given the same Gaussian and Lorentzian widths. For the Gaussian width the value assigned to the parent diagram transition was taken. The Lorentzian width was approximated by :

$$\Gamma = \Gamma_{j_1} + \Gamma_{j_3} + 2 \cdot \Gamma_{j_2} \tag{II.5}$$

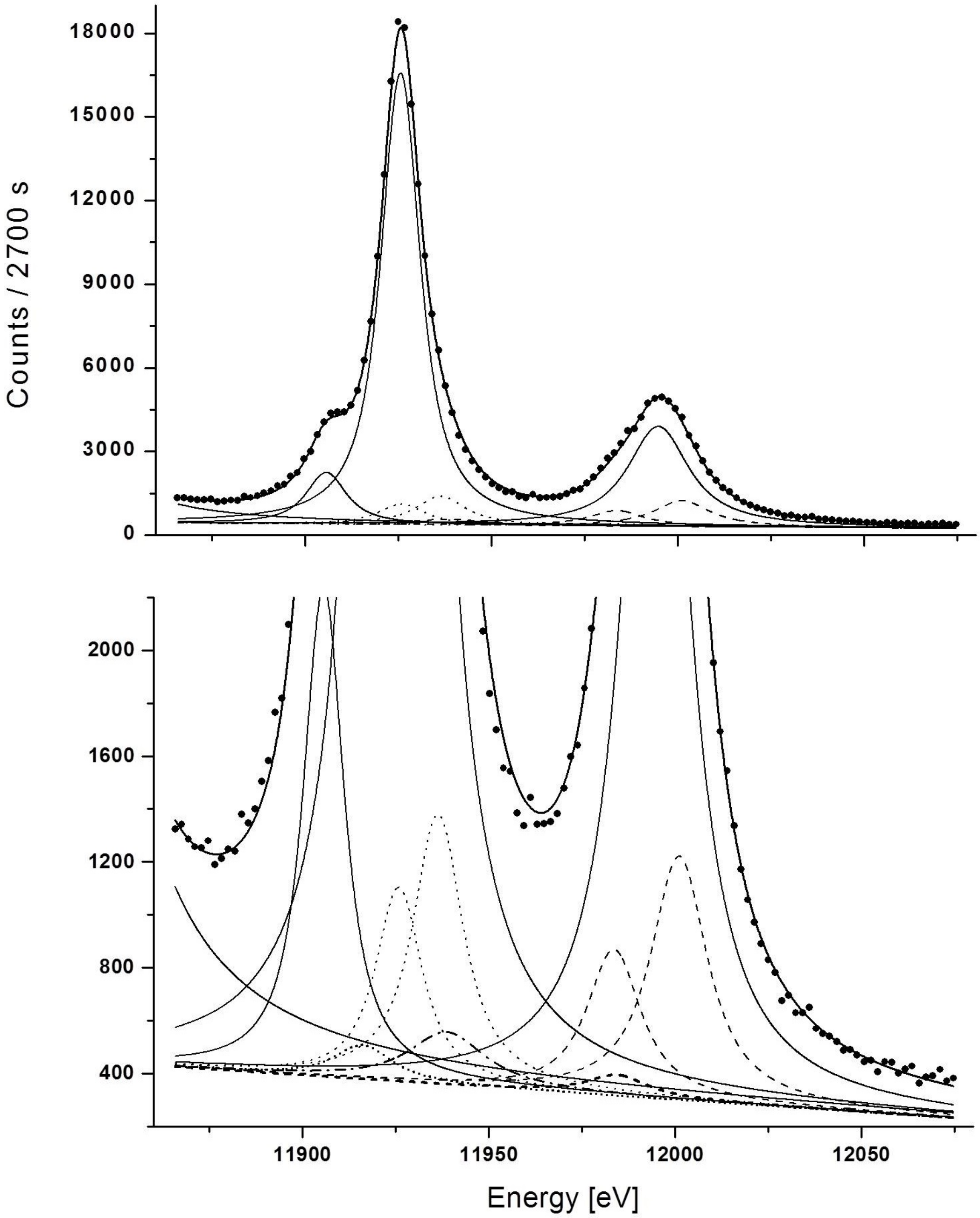

Figure II.9 – Hg $L_3 - N_{4,5}$ and $L_1 - M_3$ transitions measured with the DuMond spectrometer. As shown, the $L_1 - M_3$ diagram line is overlapping with the M-satellites (dashed lines) of the $L_3 - N_{4,5}$ transitions which in turn are overlapping with their N-satellites (dotted lines). Details about the simulated satellites are shown in the bottom part of the figure. The weak dotted and dashed components correspond to the N and M-satellites of the $L_3 - N_4$ transition. The dashed-dotted component represents the second order N-satellite of the $L_3 - N_5$ transition. The higher background observed on the left side of the spectrum is due to the high-energy tail of the strong $L_2 - M_4$ transition. The fitted tail is clearly visible in the bottom part of the figure.

where Γ_{j_1} and Γ_{j_3} are the widths of the subshells where the transition hole is located in the initial and final states and Γ_{j_2} the width of the subshell where the spectator hole is located. The subshell widths were taken from Ref. [33]. The relative intensities of the components were assumed to be proportional to the relativistic electric-dipole X-ray emission for a double-hole-state transition [54]:

$$I_{\mathsf{rel}} \propto (2J'+1)\cdot(2j_1+1)\cdot\begin{Bmatrix} j_3 & J' & j_2 \\ J & j_1 & 1 \end{Bmatrix} \tag{II.6}$$

The $6j$-coefficients occurring in rel. (6) were calculated using the formula and symmetry properties reported in [55]. It was found that most of the so-constructed M and N-satellite profiles could be well reproduced by two juxtaposed Voigtians. In the fits the widths, positions and yield ratios of the two Voigtians were kept fixed at the values obtained from the calculations.

The relative intensities of the satellite lines which are equal to the ratios of double-to-single vacancy states were estimated, using the radiationless transition probabilities reported recently by Santos *et al.* for the subshells L_1 [56] and L_2 [57], the fluorescence yields quoted in [58] and the relative intensities of the transitions L_1-M_2, L_2-M_4 and L_3-N_1 measured in the present work. The following results were obtained :

$$\frac{I(L_2^{-1}N_{3-7}^{-1})}{I(L_2^{-1})} = 0.06 \tag{II.7}$$

$$\frac{I(L_3^{-1}N_{1-7}^{-1})}{I(L_3^{-1})} = 0.15 \tag{II.8}$$

$$\frac{I(L_3^{-1}M_{4,5}^{-1})}{I(L_3^{-1})} = 0.23 \tag{II.9}$$

Rearrangement processes that modify the number of spectator vacancies prior to the L X-ray emission were taken into account in these calculations. In particular, the Auger decay of the $M_{4,5}$ spectator vacancies into $N_i^{-1}N_j^{-1}$ double-vacancies was considered. This process leads to $L_3^{-1}N_i^{-1}N_j^{-1}$ triple-vacancy states, i.e., to second order N-satellites. Using the $M_{4,5}N_iN_j$ Auger rates reported by McGuire [59] and the fraction of $L_3^{-1}M_{4,5}^{-1}$ two-hole states given by (II.9), the following ratio was obtained for the triple-vacancy states :

$$\frac{I(L_3^{-1}N_{1-7}^{-2})}{I(L_3^{-1})} = 0.08 \tag{II.10}$$

Above estimates for the satellite yields were compared with the values obtained from the fits for the total satellite intensities. The comparisons were made, using resolved and partially resolved satellites. More or less satisfactory agreements were found. However, some trend of the calculations to overestimate the intensities of the M-satellites was observed. For this reason, in most fits the total intensities of the satellites were let free and intensities fixed to above estimates were only employed in the case of non-converging fits or when the satellite intensities from the fits were obviously wrong.

An example of calculated M and N-satellite profiles is presented in Fig. II.10 for the $L_3 - M_1$ transition. The stick spectrum in the top inset represents the energies and relative intensities of the components of the $L_3^{-1}M^{-1} \rightarrow M_1^{-1}M^{-1}$ satellite transition, the open circles correspond to the sum of the Voigtians attached to the different components and the solid line stands for the fit of this sum with two Voigtians. The two pairs of Voigtians corresponding respectively to the M-satellite (dashed lines) and N-satellite (dotted lines) are represented enlarged in the bottom inset. As shown in the main figure the observed shape of the high-energy flank of the diagram transition could be well reproduced by the calculated M-satellite. One can also see that the N-satellite diminishes somewhat the fitted width of the diagram transition and has thus to be considered to obtain reliable results.

A further example is shown in Fig. II.9 representing the $L_3 - N_{4,5}$ and $L_1 - M_3$ transitions. One sees that in this case the two Voigtians corresponding to the M-satellite of the strong $L_3 - N_5$ transition coincide accidentally in energy with the $L_1 - M_3$ transition whose observed width is therefore significantly affected by the overlapping satellite. In the fit the M and N-satellites of the $L_3 - N_4$ and $L_3 - N_5$ transitions were considered as well as the second order N-satellite of the $L_3 - N_5$ transition. The line shape of this second order satellite being almost symmetric, the latter was fitted with a single Voigt profile (dashed-dotted line). The same holds for the M and N-satellites of the weak $L_3 - N_4$ transition. The seven Voigtians used to reproduce the satellites are shown enlarged in the bottom part of the figure.

As the energy shifts for transitions from the O-shell are not quoted in [53], no simulation could be performed for the satellites of $L_{2,3} - O$ transitions. In Ref. [60], some data are available but they concern only the L_1-shell. Fortunately, no overlap between the M-satellites of the $L_3 - O_1$ and $L_3 - O_5$ transitions and other diagram transitions was observed so that the line shapes of these satellites were

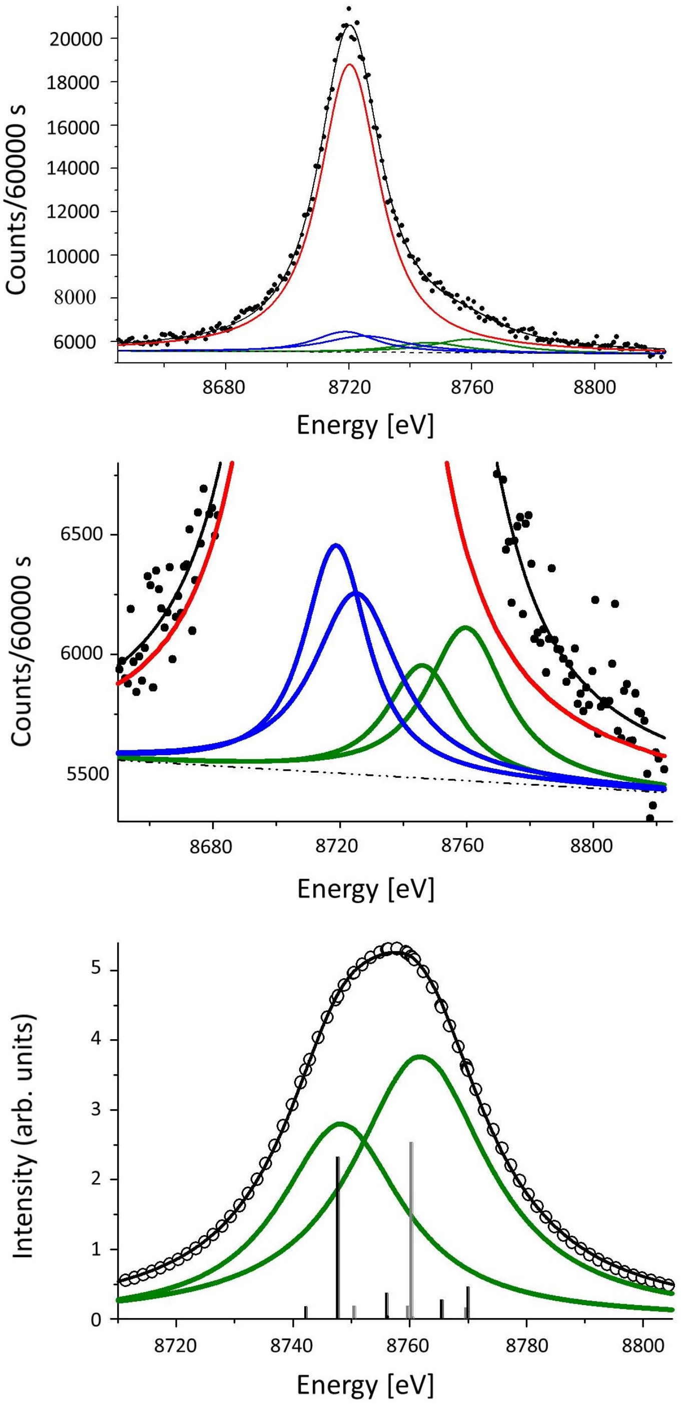

Figure II.10 – Hg $L_3 - M_1$ transition measured with the von Hamos spectrometer (top panel). The fitted diagram line is represented by the red line. The calculated N-satellites (blue lines) and M-satellites (green lines) as well as the linear background (double dot-dashed line) are shown enlarged in the middle panel. The bottom panel shows the calculated M-satellite components, the resulting satellite profile and the two Voigtians employed to reproduce the simulated shape. More details are given in the text.

not needed in the data analysis. For the N-satellites of the $L_2 - O_1$, $L_2 - O_4$ and $L_3 - O_1$ transitions, the energy shifts and widths of the two Voigtians were fixed at the values obtained from the fit of the resolved $L_3 - O_5$ N-satellite, whereas the satellite intensities were either let free in the fits or kept fixed at the above theoretical estimates. The uncertainties related to these crude approximations were considered in the calculation of the errors reported for these transitions in Tables II.1 and II.3 (see next section).

II.4 Results and discussion

II.4.1 Transitions energies

The energies of the K, L and M X-ray transitions observed in the present work are presented in Table II.1. Experimental energies from Bearden [31] and theoretical values taken from Ref. [30] are also presented for comparison. Transition energies derived from the electron binding energies obtained in this work (see next subsection) are also quoted to point out which transitions deviate from the self-consistency principle.

Table II.1 – Energies in eV of the observed Hg transitions. The energies quoted in the third column were derived from the K to M_5 and O_1 binding energies obtained in the present work by the least-squares fit method (see Sect. II.4.2) and the average values of the N_1 to N_7 and O_2 to O_5 binding energies reported by Svensson *et al.* [35] and Fuggle and Martensson [32]. The notation 68892.78(1.10/29) means 68892.78 eV ± 1.10 eV with an included statistical error from the fit of ± 0.29 eV.

Transition	Present work	Calc. from present binding energies	Bearden [31][a]	Theor. values from Ref. [30]
$K-L_2$	68892.78(1.10/29)[b]	68893.14(48)	68895.1(1.7)	68894.3(2.3)
$K-L_3$	70818.53(89/21)[b]	70818.15(47)	70819.5(1.8)	70819.0(2.2)
$K-M_2$	79822.94(1.16/63)[b]	79822.65(50)	79823.3(2.3)	79824.1(3.6)
$K-M_3$	80253.86(1.04/35)[b]	80254.22(50)	80254.2(2.3)	80256.1(3.7)
$K-N_3$	82525.88(1.25/50)[b]	82526.00(49)	82544.8(16.3)	82527.7(2.5)
L_1-M_2	11563.09(18/8)[b]	11563.10(17)	11563.1(1.1)	11563.7(3.0)
L_1-M_3	11994.68(20/8)[c]	11994.67(19)	11995.4(1.2)	11995.6(3.1)
L_1-M_4	12457.10(54/51)[c]	12456.96(17)	12445.5(3.7)	12456.6(2.4)
L_1-M_5	12547.68(31/26)[c]	12547.65(17)	12560.3(3.8)	12547.1(2.3)
L_1-N_2	14162.74(27/18)[c]	14162.59(43)	14162.3(1.7)	14164.7(4.6)
L_1-N_3	14266.05(26/16)[c]	14266.44(22)	14264.8(1.7)	14267.2(1.9)
L_1-N_5	14484.14(47/42)[c]	14484.14(29)	14474.3(1.8)	14484.8(1.7)

---

[a] Readjusted according to CODATA 06 [47].

[b] DuMond spectrometer, SiO_2 (220). Reference energy: 68804.50(18) eV (Au $K\alpha_1$) [30].

[c] DuMond spectrometer, SiO_2 (110). Reference energy: 68804.50(18) eV (Au $K\alpha_1$) [30].

Table II.1 *(continuation)*

Transition	Present work	Calc. from present binding energies	Bearden [31][a]	Theor. values from Ref. [30]
$L_1 - O_3$	14778.86(28/18)[c]	14778.44(29)	14778.5(1.8)	
$L_2 - M_1$	10648.51(71/12)[d]	10647.06(32)	10651.4(1.4)	10647.3(2.5)
$L_2 - M_4$	11823.29(15/2)[c] 11823.75(95/4)[e]	11823.38(11)	11822.7(8)	11822.7(1.4)
$L_2 - N_1$	13407.08(29/22)[c]	13407.01(41)	13410.3(1.5)	13408.1(3.4)
$L_2 - N_4$	13831.30(20/5)[c]	13831.26(18)	13830.2(1.1)	13831.7(2.7)
$L_2 - N_6$	14105.81(30/23)[c]	14105.61(15)	14107.3(1.7)	14105.2(1.6)
$L_2 - O_1$	14087.57(42/37)[c]	14087.79(27)	14089.7(1.7)	
$L_2 - O_4$	14199.86(22/9)[c]	14199.91(15)	14198.8(1.7)	
$L_3 - M_1$	8721.71(34/3)[d]	8722.04(30)	8721.3(9)	8722.6(1.9)
$L_3 - M_4$	9898.71(32/6)[d]	9898.36(13)	9897.7(8)	9898.1(1.3)
$L_3 - M_5$	9989.43(33/1)[d]	9989.05(14)	9988.9(6)	9988.6(1.2)
$L_3 - N_1$	11482.01(23/17)[c]	11482.00(41)	11482.5(1.1)	11483.5(3.2)
$L_3 - N_4$	11905.64(22/12)[c]	11906.25(18)	11904.1(1.2)	11907.0(2.5)
$L_3 - N_5$	11925.58(18/2)[c]	11925.55(27)	11924.2(1.2)	11926.3(6)
$L_3 - N_7$	12184.32(42/38)[c]	12184.70(15)	12194.1(1.2)	12184.7(1.4)
$L_3 - O_1$	12162.92(33/28)[c]	12162.78(24)	12162.6(1.2)	
$L_3 - O_5$	12277.00(17/4)[c]	12276.80(15)	12277.1(1.3)	
$M_4 - N_6$	2282.23(5/1)[f]	2282.23(13)	2282.5(6)	
$M_5 - N_7$	2195.71(9/1)[f]	2195.65(15)	2195.3(5)	

---

[a] Readjusted according to CODATA 06 [47].

[c] DuMond spectrometer, SiO_2 (110). Reference energy: 68804.50(18) eV (Au $K\alpha_1$) [30].

[d] von Hamos spectrometer, LiF(420). Reference energies: 8638.91(7) eV (Zn $K\alpha_1$) [61], 9886.52(11) eV (Ge $K\alpha_1$) [31] and 11222.52(12) eV (Se $K\alpha_1$) [30].

[e] von Hamos spectrometer, SiO_2(446). Reference energies: 11222.52(12) eV (Se $K\alpha_1$) [30] and 11924.35(34) eV (Br $K\alpha_1$) [31].

[f] von Hamos spectrometer, ADP(101). Reference energies: 2165.90(11) eV (Nb $L\alpha_1$) [31] and 2293.18(5) eV (Mo $L\alpha_1$) [31].

As mentioned before, for mercury there are no other recent high-resolution measurements of X-ray transitions decaying core-vacancy states, except for the weak $L_1 - M_{4,5}$ quadrupole transitions for which energies of 12457.05(52) eV and 12547.60(29) eV were reported [3]. Taking into consideration the small difference of the reference energy (Au $K\alpha_1$ transition) used in [3] (68804.94 eV) and in the present work (68804.50 eV), adjusted values of 12456.97(52) eV and 12547.52(29) eV are obtained, which are both in good agreement with the values quoted in Table II.1 (12457.10 ± 0.54 eV and 12547.68 ± 0.31 eV). The energies found with the DuMond and von Hamos spectrometers for the $L_2 - M_4$ transition differ by 0.46 eV but the two results are consistent within the quoted errors. The total errors listed in Table II.1 (first numbers in the brackets) include the fit errors which are also indicated (second numbers in the brackets). For the transitions observed with the von Hamos spectrometer, the total errors are generally bigger than those observed with the DuMond spectrometer for transitions of comparable energies. These bigger errors are mainly due to the uncertainties related to the energy calibration of the von Hamos spectrometer.

The comparison with Bearden's energies shows that about one third of the values are not consistent with present results within the combined errors, more than 15% of them being even not consistent within 3-σ errors. In particular, surprisingly strong deviations are observed for the $K - N_3$ (+18.9 eV), $L_1 - M_4$ (-11.6 eV), $L_1 - M_5$ (+12.6 eV), $L_1 - N_5$ (-9.8 eV) and $L_3 - N_7$ (+9.8 eV) transitions. It can be also noted that the errors of the present transition energies are in average about three times smaller than those of Bearden. The comparison with the theoretical energies reported in [30] shows on the contrary an excellent agreement since all quoted values are consistent with present results. The errors listed in [30] for the theoretical transition energies could even be somewhat overestimated since the average deviations between the theoretical values and present results are about 2.5 times smaller than the reported theoretical uncertainties. Five kinds of contributions were considered in these calculations, namely the finite size of the atomic nucleus, different relativistic effects (corrections to the Coulomb energy, magnetic and retardation energy), the Coulomb and Breit correlation, several radiative (QED) corrections and the Auger shift. More details about the theoretical procedures used to perform these calculations can be found in [62].

A good agreement is also observed between the transition energies directly measured and those derived from the binding energies. Actually, Table II.1 shows that only for the $L_2 - M_1$ and $L_3 - N_4$ transitions the two energies are not consistent. For the first transition, the measured energy is smaller by 1.45 eV than the one deduced from the binding energy difference, whereas the combined error of the two energies is 0.78 eV. No precise explanation was found for that discrepancy. For the $L_3 - N_4$ transition, the measured energy is bigger by 0.61 eV and the combined error is 0.28 eV. In this case, the explanation for the discrepancy resides probably in the difficulties encountered to fit precisely the weak $L_3 - N_4$ transition, the latter being poorly separated from the stronger close-lying $L_3 - N_5$ transition (see Fig. II.9). For these two inconsistent transition energies, the values derived from the binding energy differences are probably more reliable. They are also closer to the theoretical predictions than the measured ones. Finally, one would like to point out that the errors of the energies computed from the binding energies are smaller than those of the measured energies and that they do not depend on the intensity of the considered X-ray line. This method presents thus the advantage to provide also precise energies in the case of weak transitions. The errors quoted in Table II.1 for the transition energies derived from the binding energy differences were computed by means of the following relation :

$$\Delta E_{ij} = \pm\sqrt{\sigma_{ii}^2 + \sigma_{jj}^2 - 2\sigma_{ij}} \tag{II.11}$$

where ΔE_{ij} represents the error on the energy of the transition $i \to j$ and σ_{ii}^2, σ_{jj}^2 and σ_{ij} are diagonal variance elements, respectively off-diagonal covariance elements, of the error matrix related to the least-squares fit method employed to compute the binding energies.

II.4.2 Binding energies

As the energy of an X-ray transition is equal to the difference of the binding energies of the two atomic levels involved in that transition, a linear system of simultaneous equations could be deduced from the transition energies listed in Table II.1. The system was solved by means of a least-squares-fitting method, using the total errors on the transition energies to weight the different equations. For the binding energies of the subshells N_1 to N_7 and O_2 to O_5, reliable XPS data do exist. In addition, these binding energies are small relative to the energies of the transitions in which the above subshells are involved. Thus, with the least-squares-fit method these values cannot be determined with high precision. For these reasons, the binding energies of these levels were not used as variables but replaced in the corresponding equations by their known values. For the latter, the average values of the binding energies reported in Refs. [32] and [35] were taken, using the half-differences between the two values as uncertainty estimates. For the subshell O_1, however, no value is quoted in [35] for liquid Hg (a binding energy of 134 ± 5 eV is given but for the Hg vapor) and the value reported by Fuggle and Martensson (127 eV) [32] looks dubious because it is inconsistent with the results (about 120 eV) from other sources (e.g. [63], [64]). The binding energy of the $5s_{1/2}$ level was therefore used as an additional free fitting parameter. Thus the system consisted of 31 linear equations with 10 unknowns, namely the electron binding energies of the K-shell and L_{1-3}, M_{1-5} and O_1-subshells. The so-obtained binding energies are presented in Table II.2. Quoted uncertainties originate from the error matrix of the least-squares-fit. They correspond to relative uncertainties of about 5 ppm for the K-shell, 10 ppm for the L-subshells and 80 ppm, respectively 40 ppm, for the M_{1-3} and $M_{4,5}$-subshells. For the O_1-subshell a satisfactory precision of about 0.3 eV (0.2%) was obtained. The biggest relative uncertainties are found for the M_{1-3} and O_1-subshells because these levels occur only in two transitions, whereas other subshells are involved in a number of transitions varying from three for the M_5-subshell up to ten for the L_3-subshell.

Table II.2 – Binding energies in eV of the levels K to M_5 and O_1. Results obtained in the present work are compared to compiled experimental data [63, 64] and to predictions from theoretical calculations [65–67].

Level	Present work	Bearden and Burr [63]	Storm and Israel [64]	Polasik [65]	Huang *et al.* [66] Chen *et al.* [67]*
K	83102.75(47)	83102.3(8)	83102	83110.0	83101.0 83105.6*
L_1	14843.19(15)	14839.3(1.0)	14842	14859.0	14857.6 14858.7*
L_2	14209.61(11)	14208.7(7)	14209	14217.0	14213.9 14214.1*
L_3	12284.60(11)	12283.9(4)	12283	12292.3	12289.8 12289.2*
M_1	3562.55(31)	3561.6(1.1)	3562	3578.3	3583.7
M_2	3280.10(23)	3278.5(1.3)	3280	3292.0	3291.9
M_3	2848.53(24)	2847.1(4)	2847	2861.0	2860.1
M_4	2386.23(9)	2384.9(3)	2385	2393.9	2393.1
M_5	2295.55(11)	2294.9(3)	2295	2303.5	2302.5
O_1	121.81(26)	120.3(1.3)	121		133.6

We tried therefore to extend the measurements to additional M_{1-3} X-ray lines. The energy regions corresponding to the M_1-N_3, M_1-O_3, M_2-N_4, M_2-O_4, M_3-N_5, M_3-O_1 and M_3-O_5 transitions were explored. The measurements were performed with the ADP (101) crystal in second order of diffraction, except for the M_3-N_5 transition which was measured in first order. Although some of these transitions were observed successfully for Th and U with the same von Hamos spectrometer [7], for Hg no significant intensity could be found above the background at the expected positions of the transitions. This is due to the cumulative effects of several factors such as the poorer fluorescence yields of the M-subshells of Hg as compared to those of Th and U, the bigger self-absorption of the Hg M X-rays in the target and to their additional attenuation by the Kapton^{TM} window. For instance, for the Th M_2-N_4 transition, a net intensity of 750 counts /36'000 s on the top of the line was observed in [7]. For Hg, during a 10'000 s test measurement only a flat background of about 1000 counts was observed, without any evidence for the presence of the X-ray line of interest. This is, however, not really surprising since the fluorescence yield of the M_2-subshell is 2 times smaller for Hg than for Th [68] and the self-absorption 2 times bigger. Considering in addition the intensity attenuation caused by the 8 μm thick Kapton^{TM} window, a peak-to-background ratio of only 0.04:1 is indeed expected for the Hg M_2-N_4 transition. Assuming that the minimum intensity of an X-ray line needed for a reliable fit must be at least 10 times bigger than the background fluctuations, an acquisition time of about 170 hours would have been necessary for the measurement of the sole M_2-N_4 transition. We have thus renounced to measure it. The same holds for the M_1-N_3, M_1-O_3, M_2-O_4 and M_3-O_1 transitions for which similar negative results were obtained in exploratory measurements. On the other hand, for Th the M_3-N_5 and M_3-O_5 transitions being about 10 times, respectively 4 times, more intense than the M_2-N_4 one [7], the observation of these transitions in Hg looked more promising. Unfortunately the two lines were found to be hidden by the tail of the much stronger L_3-M_5 transition occuring in fourth order of diffraction, respectively seventh order, at about the same Bragg angles as the first order and second order diffractions of the M_3-N_5 and M_3-O_5 transitions, respectively, making thus these measurements unfeasible, too.

In Table II.2, present binding energies are compared to experimental results from Bearden and Burr [63], semi-empirical values from Storm and Israel [64] and theoretical predictions from different sources [65–67]. Actually, compilations of experimental electron binding energies that are more recent than the one of Bearden and Burr do exist but data given in these papers for core levels of mid-heavy and heavy elements are still those from Bearden and Burr so that we have preferred to quote the original reference. For instance, for Hg the binding energies listed in [69] coincide with Bearden and Burr's values, except those for the outer N- and O-shells that were taken from [32]. From the examination of the table one sees first that present binding energies are systematically higher than those of Bearden and Burr. The biggest discrepancy is observed for the L_1-subshell for wich the deviation amounts to 3.9 eV, which is about 4 times more than the uncertainty quoted by Bearden and Burr for this level. For the other levels, the average deviation is approximately 1 eV whereas the average uncertainty is about 0.8 eV. A better agreement is found with Storm and Israel's values since in this case the average deviation is 0.9 eV and the average uncertainty 1 eV. In particular, for the L_1-subshell the energy quoted by Storm and Israel is almost consistent with ours. It can be also noted that the values given by Bearden and Burr and Storm and Israel for the binding energy of the O_1-subshell are both consistent with our result, whereas the more recent XPS value from [32] used in the above-mentioned recent compilation [69] is significantly bigger (127 eV).

As shown in Table II.2, the binding energies predicted by theory are all higher by 5-20 eV than present experimental results, except for the K-shell for which a satisfactory agreement is found, at least for the values taken from [66, 67]. The largest deviations are observed for the M_1-subshell (20 eV) and the L_1-susbshell (15 eV). The multiconfiguration Dirac-Fock (MCDF) [65] and Dirac-Hartree-Fock-Slater (DHFS) [66,67] calculations give similar results within 1-3 eV except for the K-shell and the M_1-subshell. The MCDF value for the K-shell is indeed significantly bigger than the experimental and DHFS theoretical values, whereas for the M_1-subshell an opposite trend is observed. In both MCDF and DHFS calculations the magnetic interaction energy, retardation energy, vacuum polarization correction and higher-order QED corrections were considered. The MCDF calculations were performed, using the modified special average-level version (MSAL) [70] of the GRASP code [71]. The DHFS calculations from [67] differ from the earlier ones [66] by the use of a more accurate expression for the Breit energy, a Fermi instead of uniform distribution of the nuclear charge and a screened self-energy correction. The improvements brought by the new calculations are not directly visible in Table II.2 but the transition energies provided by the new calculations agree significantly better with the experimental results. For instance, for the $K\alpha_1$ and $K\alpha_2$ transitions, deviations of -1.7 eV and -1.6 eV are found with respect to the experimental values obtained in the present work (see Table II.1, third column), whereas the corresponding deviations for the old DHFS calculations are -6.9 eV and -5.9 eV, respectively. Note that the same comparison made with the MCDF predictions provides also a good agreement, the deviations being only -0.4 eV and -1.4 eV, respectively. A further comparison with the theoretical binding energies quoted in [30] shows that the calculations overestimate the binding energies of the K-shell and the L_{1-3}-subshells by 8.5, 7.6, 7.3 and 7.7 eV, respectively. However, by correcting the zero of the theoretical energy scale by - 7.8 eV, the adjusted edge energies are found to be fully consistent with present results.

II.4.3 Transition widths

The widths of the measured transitions are presented in Table II.3 where they are compared with existing experimental and theoretical data. As in the fits of the transitions $K-N_2$, L_1-N_4 and L_1-O_2 the line widths of the latter could be let free, whereas their energies had to be kept fixed, these transitions are quoted in Table II.3 but not in Table II.1. The values listed in the third column were derived from the level widths obtained by the least-squares-fit method discussed in the next subsection. As shown, these values are all in good agreement with the measured transition widths, except the L_1-N_4 transition for which there is a deviation (1.9 eV) that is somewhat bigger than the combined error (1.6 eV). This discrepancy is probably due to the small intensity and poor separation of the $L_1-N_{4,5}$ quadrupole doublet which made the width determination of the weaker component less reliable.

As mentioned in the introduction, for Hg experimental information concerning the natural line widths of X-ray lines is scarce. In addition, existing data are rather old. For the $K\alpha_{1,2}$ transitions, widths of 68.5 eV and 64.0 eV, respectively, were reported [72–74] that are 5-10% bigger than present results but consistent within the rather large uncertainties quoted by the authors. The values of 68.20 eV and 64.75 eV given by Salem and Lee [75] for the same transitions were derived from a least-squares-fit to existing experimental data till 1976. For the $K\beta_{1,3}$ transitions, the widths given by Salem and Lee are also bigger than ours but consistent within the indicated errors (10%). Interpolation values obtained from the widths of the $K\alpha_{1,2}$ transitions of Au and Pb from [76] are also quoted. In this case, an excellent agreement with our results is observed.

Table II.3 – Line widths in eV of the measured Hg transitions. The values quoted in the third column were derived from the widths of the levels $K-N_5$ and O_1 obtained by the least-squares fit method (see Sect. II.4.3). The notation 61.3(2.2/7) means 61.3 eV ± 2.2 eV with an included statistical error from the fit of ± 0.7 eV.

Transition	Present work	Calc. from present level widths	Experimental data from other sources	Semi-empirical and theoretical data
$K-L_2$	61.3(2.2/7)[a]	60.8(1.8)[b]		
			68.2[c]	
			61.3(3.5)[d]	
$K-L_3$	61.2(2.3/6)[a]	61.2(9)	64.0(9.6)[b]	60.1(1.8)[c]
			64.7[d]	60.5[e]
			60.4(1.1)[f]	
$K-M_2$	65.2(3.3/1.3)[a]	66.9(9)	68.9[d]	68.4[e]
$K-M_3$	61.9(3.3/9)[a]	63.0(9)	65.7[d]	65.0[e]
$K-N_2$	62.7(4.2/2.4)[a]	64.3(1.0)		
$K-N_3$	64.5(3.7/1.4)[a]	61.9(9)		
L_1-M_2	22.6(3/2)[a]	22.6(2)	19.7[d]	28.1[e]
			20.1(8)[g]	
L_1-M_3	18.6(3/2)[a]	18.6(1)	17.4[d]	24.7[e]
			17.9(1.2)[g]	
L_1-M_4	13.3(1.4/1.3)[a]	12.9(4)		16.9[e]
L_1-M_5	12.9(1.0/9)[a]	12.8(4)		16.9[e]
L_1-N_2	20.0(5/5)[a]	19.9(3)	17.2(8)[g]	
L_1-N_3	17.5(4/3)[a]	17.6(3)	15.6(6)[g]	
L_1-N_4	13.5(1.5/1.4)[a]	15.4(4)		

---

[a] DuMond spectrometer. For details see Table II.1.

[b] Nelson *et al.* [72–74].

[c] Krause and Oliver [77].

[d] Salem and Lee [75] (errors vary from 10% for the strongest K lines to 40% for the weakest L lines).

[e] Calculated from the widths Γ_K, $\Gamma_{L1,2,3}$, $\Gamma_{M1,2,3}$ and $\Gamma_{M4,5}$ reported by Chen *et al.* in Refs. [78], [79], [68] and [80], respectively.

[f] Derived by interpolation from the widths reported for Au and Pb by Kessler *et al.* [76].

[g] Derived by interpolation from the widths reported for Au and Tl by Cooper [81].

Table II.3 – *(continuation)*

Transition	Present work	Calc. from present level widths	Experimental data from other sources	Semi-empirical and theoretical data
$L_1 - N_5$	15.5(1.2/1.1)[a]	14.9(4)		
$L_1 - O_2$	19.3(7/7)[a]			
$L_1 - O_3$	18.6(6/6)[a]			
$L_2 - M_1$	21.4(5/5)[h]	21.5(1)		23.9[e]
$L_2 - M_4$	8.39(14/4)[a]	8.44(9)	8.70[d]	8.1[e]
	8.89(30/13)[h]		7.6(2)[g]	
			8.63(26)[i]	
$L_2 - N_1$	15.1(7/7)[a]	14.8(3)		
$L_2 - N_4$	11.0(2/1)[a]	10.9(1)	11.8[d]	
			10.1(3)[g]	
			11.8(6)[i]	
$L_2 - N_6$	6.82(61/56)[a]			
$L_2 - O_1$	14.8(1.0/9)[a]	15.0(4)		
$L_2 - O_4$	7.46(36/27)[a]		7.1(7)[g]	
$L_3 - M_1$	22.1(1/1)[h]	22.1(1)		23.9[e]
$L_3 - M_4$	9.20(21/16)[h]	9.00(11)	8.80[d]	8.2[e]
$L_3 - M_5$	8.87(16/4)[h]	8.92(10)	8.10[d]	8.2[e]
			9.04(18)[i]	
$L_3 - N_1$	15.3(4/4)[a]	15.4(3)		
$L_3 - N_4$	11.5(3/2)[a]	11.5(1)		
$L_3 - N_5$	11.0(2/1)[a]	11.0(1)	10.4[d]	
			10.2(4)[g]	
			11.8(6)[i]	

---

[a] DuMond spectrometer. For details see Table II.1.

[d] Salem and Lee [75] (errors vary from 10% for the strongest K lines to 40% for the weakest L lines).

[e] Calculated from the widths Γ_K, $\Gamma_{L1,2,3}$, $\Gamma_{M1,2,3}$ and $\Gamma_{M4,5}$ reported by Chen *et al.* in Refs. [78], [79], [68] and [80], respectively.

[g] Derived by interpolation from the widths reported for Au and Tl by Cooper [81].

[h] von Hamos spectrometer. For details see Table II.1.

[i] Derived by interpolation from the widths reported for Au and Tl by Williams [82].

Table II.3 – *(continuation)*

Transition	Present work	Calc. from present level widths	Experimental data from other sources	Semi-empirical and theoretical data
$L_3 - N_7$	5.86(66/63)[a]	6.77(13)		
$L_3 - O_1$	15.7(7/7)[a]	15.6(4)		
$L_3 - O_5$	7.53(20/13)[a]			
$M_4 - N_6$	2.79(20/2)[h]	2.87(11)		2.95[j]
$M_5 - N_7$	2.84(19/2)[h]	2.77(11)		2.81[j]

---

[a] DuMond spectrometer. For details see Table II.1.

[h] von Hamos spectrometer. For details see Table II.1.

[j] Derived by interpolation from the widths $\Gamma_{M4,5}$ and $\Gamma_{N6,7}$ reported for Au and Bi by McGuire in Refs [83] and [84, 85], respectively.

For L X-rays, available experimental data are even more rare than for K X-rays. In Salem and Lee's tables values are reported only for the seven strongest L transitions. Quoted values are consistent with present results if one considers the uncertainties assumed in these tables. The mean value of the deviations relative to present results is about 8%, the strongest differences being observed for the transitions $L_1 - M_2$ (-2.9 eV), $L_1 - M_3$ (-1.2 eV) and $L_2 - N_4$ (+0.80 eV). In the region $70 \leq Z \leq 83$, Salem and Lee's least-squares-fit values for L transition widths are based mainly on two old works, those of Cooper [81] and Williams [82]. Unfortunately in these two papers no data is reported for Hg. Values quoted in Table II.3 were thus obtained by interpolation from the widths given for Au and Tl. The eight transition widths derived from Cooper's work are smaller than ours by 5-15%. This is probably due to the fact that the Lorentzian widths given in this paper were obtained by subtracting the instrumental broadening from the observed widths and not by deconvolution. In the still older paper of Williams, only the widths of the four strongest transitions ($L\alpha_1$, $L\beta_1$, $L\beta_2$ and $L\gamma_1$) were determined. The measurements were performed with a double-flat crystal spectrometer, whose resolution depended on the divergence of the incident X-ray beam and finite resolving power of the employed calcite crystals. The influence of the beam divergence was assumed to be negligibly small and the crystal resolving power was not well known so that no correction was made for the instrumental broadening. This explains probably the systematic bigger values obtained by Williams with respect to present results. However, we would like to point out that, despite this systematic deviation, Williams' widths are consistent with ours.

The transition widths reported in the last column of Table II.3 were derived from semi-empirical and theoretical atomic level widths. As shown, the widths of the $K\alpha_{1,2}$ transitions obtained from the semi-empirical level widths quoted by Krause and Oliver [77] agree well with present results. The same holds for the $K\alpha_{1,2}$ widths obtained from the theoretical widths Γ_K [78] and $\Gamma_{L_{2,3}}$ [79] calculated by Chen *et al.* Theoretical predictions for the L_1 transition widths are on the contrary systematically bigger by about 20% than present experimental values. The same trend is observed for the transitions involving M_1 holes, whereas for L_2 and L_3 transitions involving $M_{4,5}$ vacancies in the final states, a satisfactory agreement is found. This observation that theory overestimates the transition widths when $2s$ [3] or $3s$ [4] vacancies are present in the initial or final state results from the difficulty of calculations to provide reliable predictions for the Coster-Kronig rates. In general, the latter are indeed overestimated by theory. For instance, theoretical L_1 Coster-Kronig widths of 14.5 eV, 11.2 eV and 10.7 eV are given in Refs [86] (interpolation between the values quoted for Au and Bi), [87] and [56], respectively. The theoretical Auger widths from the same sources are 2.5 eV, 2.0 eV and 2.1 eV, i.e, 2.2 eV in average. Subtracting the latter average Auger width and the radiative width of the $2s$ level reported by Scofield (1.2 eV) [50] from the experimental width (10.5 eV) of the subshell L_1 quoted by Campbell and Papp [33], one obtains a Coster Kronig width of 7.1 eV which is markedly smaller than the three above-mentioned theoretical values. Finally, the theoretical widths of the transitions $M_4 - N_6$ and $M_5 - N_7$ deduced from the widths of the corresponding levels calculated by McGuire [83–85] are in fair agreement with our experimental values.

II.4.4 Atomic level widths

Using the widths of the measured transitions, we were able to determine the natural widths of the K-shell, L_1 to N_5 and O_1-subshells by means of a similar least-squares-fit-method as the one employed for the determination of the binding energies. In this case the system consisted of thirty equations with the widths of the above mentioned fifteen levels as unknowns. The widths of the $N_{6,7}$-subshells were kept fixed in the fit at the values (0.33 eV and 0.31 eV) given by Campbell and Papp [33]. As the levels O_2 to O_5 occur each in a single transition, they were not included in the least-squares-fit calculations. The level widths obtained with this method are presented in Table II.4 where they are compared to the recommended values of Campbell and Papp [33] as well as to available experimental, semi-empirical and theoretical results from various sources.

Table II.4 – Level widths in eV of the subshells K to N_5 and O_1. Results obtained in the present work are compared to available experimental [33–35], semi-empirical [77] and theoretical data [59, 68, 78–80, 84].

Level	Present work	Campbell and Papp [33]	Experimental data from other sources	Semi-empirical and theoretical data
K	54.7(9)	54.8(4.9)		54.6(1.6)[a] 54.8[b]
L_1	10.3(4)	10.5(2.0)	6.4(2.0) [c]	11.3(1.7)[a] 14.5[b]
L_2	5.90(13)	5.69(57)	6.0(1.0)[c]	6.17(62)[a] 5.7[b]
L_3	6.46(12)	5.71(57)	5.8(8)[c]	5.50(44)[a] 5.7[b]
M_1	15.6(2)	15.1(2.0)		18.2[b] 21.1[d]
M_2	12.2(5)	9.8(1.8)		13.6[b] 14.7[d]
M_3	8.25(48)	8.6(1.6)		10.2[b] 9.7[d]
M_4	2.54(11)	2.28(23)		2.45[b] 2.82[d]
M_5	2.46(11)	2.28(23)		2.45[b] 2.68[d]

---

[a] Krause and Oliver [77].

[b] Chen *et al.*, Γ_K [78], $\Gamma_{L1,2,3}$ [79], $\Gamma_{M1,2,3}$ [68] and $\Gamma_{M4,5}$ [80].

[c] Keski-Rahkonen *et al.* [34] (XAS measurements).

[d] Estimated from an interpolation of the widths Γ_{M1-M5} and Γ_{N1-N5} reported for Au and Bi by McGuire in Refs [59] and [84], respectively.

Table II.4 – *(continuation)*

Level	Present work	Campbell and Papp [33]	Experimental data from other sources	Semi-empirical and theoretical data
N_1	8.93(29)	8.8(9)	$\sim 10^{\mathrm{e}}$	15.4^{d} 7.75^{f}
N_2	9.61(55)	6.55(80)	$\sim 9^{\mathrm{e}}$	14.1^{d} 7.87^{e}
N_3	7.22(50)	5.3(8)	5.5^{e}	12.6^{d} 4.40^{e}
N_4	5.05(17)	4.0(5)	4.4^{e}	8.5^{d} 5.37^{e}
N_5	4.59(15)	3.85(50)	4.0^{e}	8.2^{d} 5.22^{e}
O_1	9.11(41)			

---

[d] Estimated from an interpolation of the widths Γ_{M1-M5} and Γ_{N1-N5} reported for Au and Bi by McGuire in Refs [59] and [84], respectively.

[e] Svensson *et al.* [35] (XPS measurements, results not corrected for spectrometer resolution).

[f] Ohno and Wendin [88].

Errors on present results correspond to the diagonal elements of the error matrix associated to the least-squares-fit method. They vary from about 1% (M_1-subshell) to about 7% (N_3-subshell). The precision depends on the number of transitions in which the considered level is involved, the uncertainties of the widths of these transitions and on the relative value of the level width with respect to the widths of the associated transitions.

The comparison with Campbell and Papp's values shows a fair agreement for most levels, except for the M_2, N_2 and N_3 ones for which significant differences of 2.4 eV, 3.1 eV and 1.9 eV, respectively, are observed, the widths of the three levels quoted by Campbell and Papp being smaller than ours by about 30%. For the $N_{4,5}$ levels, a similar trend is observed but the deviations are smaller (15%). However, despite the observed discrepancies, we are inclined to believe that present results for the M_2 and N_{2-5} levels are reliable for the following reasons. The M_2 level width of Hg recommended by Campbell and Papp was determined by interpolation from the widths of the transitions $L_1 - M_2$ of Au and Tl reported by Cooper [81], using for the width of the $2s$ level their recommended value of 10.5 eV. The so-obtained

M_2 width was then increased by 0.2 eV to account for the too large correction made by Cooper for the instrumental broadening. Since Campbell and Papp's value for the width of the L_1-subshell is close to the one obtained in the present work, the discrepancy observed for the M_2- subshell originates from the width of the $L_1 - M_2$ transition quoted by Cooper which is certainly too small, as discussed in the preceding subsection.

For the $N_{2,3}$-subshells of elements above Z = 70, there are no recent XES data except for actinides and only a limited number of XPS data. In addition, the XPS data evince a considerable scatter. For this reason Campbell and Papp have deduced their recommended $N_{2,3}$ level widths from least-squares-fit curves that run monotonically through the existing XPS data and join smoothly to modern XES data that are available for Th [7] and U [6]. On the low-Z side, the curves were anchored to the Xe $N_{2,3}$ widths obtained from many-body theory (MBT) calculations [89]. In our opinion, it is thus possible that the $N_{2,3}$ level widths quoted by Campbell and Papp for that region of the periodic table are questionable and characterized by bigger errors than the quoted ones. Furthermore, comparing the widths reported by Cooper [81] for the transitions $L_1 - M_{2,3}$, $L_2 - M_4$, $L_2 - N_4$, $L_2 - O_4$ and $L_3 - N_5$ with the results obtained in this work (see Table II.3), an average ratio of 0.92 ± 0.03 is found for the two sets of values. Using this ratio to adjust the widths of the transitions $L_1 - N_{2,3}$ given by Cooper, new values of 18.6 ± 1.0 eV and 16.9 ± 0.8 eV are found for the two transitions widths. Subtracting then from the latter the L_1 level width recommended by Campbell and Papp (10.5 ± 2.0 eV), one obtains $N_{2,3}$ widths of 8.1 ± 2.2 eV and 6.4 ± 2.1 eV that are still smaller than our results but consistent with them.

For the $N_{4,5}$-subshells several difficulties were also encountered by Campbell and Papp. Actually, in the region $70 \leq Z \leq 83$, XPS data are more numerous and cluster quite closely but their results disagree with values derived from measurements of the $L_2 - N_4$ and $L_3 - N_5$ transitions [81,90] which lie 1.5 eV to 3 eV higher. The small number of available data from Auger electron spectroscopy (AES) [91] lie also high relative to the XPS trend. As these XES and AES data are pretty old, Campbell and Papp renounced to use them and preferred to employ the XPS data. However, they mentioned that the so-determined widths could be somewhat too small and that it would be therefore desirable to cross-check them with a modern set of measurements of the $L_2 - N_4$ and $L_3 - N_5$ X-ray line widths.

Existing experimental information for the level widths of Hg is scarce. Data were found only for the L, N and O-subshells. The L-subshells widths were determined by Keski-Rahkonen *et al.* from X-ray absorption spectroscopy (XAS) measurements [34]. The obtained level widths are in agreement with present results for the $2p$ levels but in strong disagreement for the $2s$ level for which a value smaller by 4 eV is reported in that work. For the N and O-subshells XPS data were published by Svensson *et al.* [35]. However, quoted level widths were not corrected for the instrumental broadening and no indication is given for the uncertainties attached to the quoted values. Nevertheless, one sees in Table II.4 that a satisfactory agreement with present results is observed for the N_1 and N_2 levels, whereas for the N_{3-5} levels, the XPS widths are 0.5-1.5 eV smaller than present results. Note that Svensson's values for the N_{3-5} levels are close to Campbell and Papp's ones because, as discussed above, the latter were determined precisely from XPS data, those of Svensson included. In [35], level widths are also reported for the O-subshells. Values of 6 eV, 5.7 eV, 0.86 eV and 1.33 eV are given for the $5p_{1/2}$, $5p_{3/2}$, $5d_{3/2}$ and $5d_{5/2}$ levels of solid Hg. As for the N-subshells, the values were not corrected for the instrumental resolution. Assuming for the L_{1-3} level widths our values of 10.3(4) eV, 5.90(13) eV and 6.46(12) eV, O_{2-5} widths of 9.0(8) eV, 8.1(7) eV, 1.6(4) eV and 1.1(2) eV are obtained from the widths of the transitions $L_1 - O_{2,3}$, $L_2 - O_4$ and $L_3 - O_5$ presented in Table II.3. One sees that except for the $5d_{5/2}$ level, Svensson's values are again 1-3 eV smaller than ours. These discrepancies between the level widths determined in the present work and those derived from XPS measurements are, however, not really surprising since it is well established that several factors complicate the experimental determination of natural lifetime broadenings in XPS core-level spectroscopy. In particular, the asymmetry characterizing XPS peaks makes difficult the determination of the contribution of the lifetime broadening to the observed line shape [92]. This contribution is generally determined by considering the half-width at half-maximum (HWHM) on the low-binding energy side of the XPS peaks instead of the full-width at half-maximum (FWHM). However, lifetime broadenings extracted from HWHM widths are only correct if effects such as, e.g., the couplings of the core-electron transitions to many-electron excitations of the valence electrons, that may affect the positions and intensities of the profile centroids, are negligible.

Considering now the last column of Table II.4, one sees that Krause and Oliver's semi-empirical values for the K-shell and $L_{1,2}$-subshells [77] are in agreement with present level widths. For the L_3-subshell, however, both values are consistent only if the interval of the combined error is extended to 2-σ. Theoretical predictions from Chen *et al.* for the K-shell [78], $L_{2,3}$-subshells [79] and $M_{4,5}$-subshells [80] are well reproduced by our results. On the contrary, due to the above mentioned difficulty of theory to predict precise Coster-Kronig transition probabilities, the M_1 and to a lesser extent the L_1 and $M_{2,3}$ level widths obtained in our work are significantly overestimated by Chen's *et al.* calculations [68, 79]. A comparison with the theoretical level widths reported by McGuire [83–85] shows the same trend for theory to overestimate the experimental results but in this case the deviations are even more pronounced. However, for the $M_{4,5}$ subshells which are not affected by Coster-Kronig transitions, McGuire's predictions are consistent with present results. Data from non-relativistic MBT calculations by Ohno and Wendin [88] were also found for the N-subshells. In this study different approximations were probed. Results quoted in Table II.4 correspond to the so-called A2 approximation corresponding to a frozen-core potential and relaxed Auger energy. As shown, the MBT results are smaller than McGuire's predictions and much closer to the experimental widths found in our work. For the $4p_{3/2}$ level, however, a significantly smaller value than ours is provided by these MBT calculations. Finally, let us mention that a quick survey of the magnitude and trends of theoretical predictions for the total level widths can be obtained from the graphs published by Keski-Rahkonen and Krause [93]. However, as it is rather difficult to extract precise values from the logarithmic scales of these plots, we have renounced to quote these values in Table II.4.

II.5 Summary and concluding remarks

High-resolution measurements of the fluorescence X-ray emission of liquid mercury were performed. X-ray transitions above 11 keV were measured with a transmission DuMond-type crystal spectrometer, transitions below 11 keV with a reflection von Hamos-type crystal spectrometer. From the observed spectra, precise and reliable data for the energies and widths of K, L and M X-ray transitions were determined. Energy shifts and/or line broadenings resulting from M and N-satellites were accounted for in the data analysis. Solving by means of a least-squares-fit method the two linear systems of simultaneous equations built on the transition energies and transition widths obtained from the data analysis, the binding energies and natural widths of most core-levels of Hg could be deduced.

Bearden's transition energies [31] that are still used as references in many modern spectroscopy works were found to be inconsistent with present results for more than 30% of the measured transitions, deviations as big as 20 eV being observed. In contrast to that a perfect agreement was found between our results and theoretical transition energies published recently [30].

For the binding energies of the ten core-levels that could be extracted from our work, a more or less satisfactory agreement was observed with Bearden and Burr's values [63] which, despite their age, still represent the main data base for binding energies of core-levels of mid-Z and high-Z elements. However, present binding energies were found to be systematically higher by about 1 eV, a discrepancy of approximately 4 eV being even observed for the L_1-subshell.

Present transition widths were compared to available experimental, semi-empirical and theoretical data. In general, existing information was found to be scarce and in most cases old. For the K transitions the semi-empirical values from Krause and Oliver [77] are in agreement with our results, whereas the experimental values reported by Salem and Lee [75] lie significantly higher. For the widths of the few L transitions quoted by Salem and Lee, smaller deviations are, however, observed. The comparison with results of theoretical calculations showed a satisfactory agreement except for the transitions involving a $2s$ or $3s$ vacancy in the initial or final state.

The fifteen atomic level widths deduced from our measurements were compared principally to the recommended values reported recently by Campbell and Papp [33]. A fair agreement was found for most levels. The discrepancies observed for the

M_2 and $N_{2,3}$-subshells were discussed and tentative explanations were proposed. Results of theoretical predictions from different sources were also considered. As for the transition widths, it was found that theory provides reliable predictions, except for the levels whose lifetime broadenings are dominated by Coster-Kronig transitions. In these cases, the calculations, except the MBT ones, overestimate considerably the experimental level widths.

Chapter III

Hypersatellite decay of $20 \leqslant Z \leqslant 29$ target elements bombarded by heavy-ions

III.1 Introduction

The radiative decay of hollow K-shell atoms, i.e., atoms with an empty K-shell, leads to the emission of X-rays that are shifted towards higher energies as compared to the parent diagram lines decaying ions with a single vacancy in the K-shell. The K-shell vacancy which is not filled by the radiative transition is called the spectator vacancy because it is not directly involved in the transition. The energy shift is due to the diminution of the electron screening originating from the removal of the second $1s$ electron which leads to enhanced binding energies for the atomic levels. As the enhancement diminishes with the principal quantum number of the atomic levels, the binding energy change of the K-shell is bigger than the one of outer shells, which results into a net increase of the transition energy. More generally, atomic structure calculations show that the energy shifts of X-ray lines emitted by doubly-ionized atoms decrease with the principal quantum number of the shell where the spectator vacancy is located. For this reason L-shell X-ray satellites, i.e., X-rays emitted by ions having an additional spectator vacancy in the L-shell, are more shifted than M-shell satellites, which in turn are more shifted than N-shell satellites. For K X-rays, the strongest energy shift is thus observed when the spectator vacancy is located in the same shell as the initial vacancy involved in the transition, i.e., the K-shell. In this case the shift is much bigger than the one observed for L satellites and for this reason X-rays emitted by doubly K-shell ionized atoms are named K hypersatellites.

The first theoretical investigation of the radiative decay of hollow atoms was done by Heisenberg [94] already 90 years ago but the first experimental evidence concerning the radiative decay of hollow K-shell atoms was reported only in 1953 by the future Nobel prize winner G. Charpak [95]. Charpak's approach consisted to measure in coincidence the two X-rays emitted sequentially by the radiative decay of hollow K-shell ^{55}Mn atoms (Z=25) resulting from the nuclear decay of ^{55}Fe (Z=26) via electron capture (EC), using two gas proportional counters for the coincident detection of the photons. In this pioneering work, the double $1s$ ionization of the Mn atoms resulted directly from the nuclear decay, the first $1s$ electron being captured by the Fe nucleus (EC) and the removal of the second resulting from the atomic inner-shell rearrangement processes following the nuclear decay. Actually the two X-rays detected in coincidence corresponded to a cascade of a K hypersatellite transition followed by a L-satellite transition but the small energy difference between these two different X-rays could not be distinguished by Charpak with the employed gas detectors. A similar coincidence experiment was performed some years later by Briand *et al.* [96] to investigate the radiative decay of double $1s$ vacancy states in ^{71}Ga atoms (Z=31) produced by the K-EC decay of the ^{71}Ge isotope (Z=32). This time, however, Briand and his coworkers used two solid state detectors whose energy-resolution allowed them to partly resolve the $K\alpha_{1,2}$ hypersatellite from its parent diagram line. It is interesting to note here that in the early days of X-ray spectroscopy (XRS) the X-ray line associated to the K^{-2}-$K^{-1}L^{-1}$ transition was usually named $K\alpha_4$ satellite [97] and to our best knowledge the word $K\alpha$-hypersatellite was used for the first time in 1971 by Briand *et al.* in [98].

The probability to produce a double K-shell ionization via nuclear decay processes such as EC, β-decay or α-decay is very weak, typically in the order of 10^{-4}. The same holds for the excitation of the sample with photons, double K-shell photoionization (DPI) probabilities varying between 10^{-2} for light elements down to 10^{-6} for high-Z elements as a consequence of the approximate Z^{-4} dependence of the DPI cross section. In both the nuclear decay and DPI processes, the second $1s$ electron is removed as a result of a shake [99,100] or knockout (KO) process [101]. The shake process is a quantum mechanics effect in which a bound electron can be ionized [shakeoff (SO)] or promoted into an unfilled outer subshell [shakeup (SU)] as a consequence of the sudden change of the atomic potential following the photoabsorption. In the KO mechanism which can be regarded as an inelastic electron-electron scattering, the second electron is ionized by the $1s$ photoelectron in a (e,2e)-like electron collision. The KO process, sometimes also named TS1 process, dominates at low photon energies, whereas at high photon energies the SO mechanism prevails [23,24].

Early DPI works were carried out using conventional X-ray sources [102,103]. The advent of synchrotron radiation facilities about 20 years ago providing intense, monochromatic and energy tunable X-ray beams combined with the development of modern high energy-resolution wavelength-dispersive spectrometers (WDS) gave a new boost to the domain (see e.g. [24,104–107]). The same holds for the more recent advent of X-ray free electrons laser (XFEL) facilities. XFEL beams are already available at LCLS (Linac Coherent Light Source) in Menlo Park, USA, at SACLA (Spring-8 Angström Compact free electron LAser), in Hyogo, Japan and at Fermi FEL/Elettra in Trieste, Italy. Some other facilities are being constructed in several countries such as Germany (European XFEL in Hamburg) and Switzerland (SwissFEL/PSI in Villigen). In the XFEL case, the extremely short (a few femtoseconds), intense (about 10^{11} photons) and micro-focused coherent X-ray pulses permit to produce double K-shell vacancy states via the absorption of two photons by the same atom [108–112]. In the XFEL DPI the first and second 1s electrons are removed sequentially by two subsequent photons belonging to the same XFEL pulse. Actually, the pulse is so short that the second electron is removed before the decay of the first vacancy. For Fe the probability of double K-hole formation via sequential absorption of two photons is about 60 times higher than the one of the single-photon DPI [113].

Double 1s vacancy states can also be produced by impact with electrons, using electron guns [22, 114]. However, as most electron guns cannot be operated above about 20 kV, only low-Z elements were investigated. An alternative method for studying the double K-shell ionization induced by electron impact consists to use as sample the X-ray tube anode itself. This approach allows to extend the electron-induced K-hypersatellite measurements to heavier elements [17, 115]. In collisions with electrons, the double K-shell ionization results from shake and TS2 processes. The TS2 process corresponds to a sequential inelastic scattering of the same incoming electron on two bound electrons. Since the shake and TS2 processes are characterized by small probabilities, K-hypersatellites induced by electron impact are also very weak.

Stronger K-hypersatellite signals can be obtained by bombarding the samples with charged particles such as protons [116], α-particles [18] or heavy ions (HI). In this case, due to the strong Coulomb field of the charged projectile, several inner-shell electrons can be indeed ionized simultaneously. X-ray spectra induced by impact with charged particles exhibit rich satellite and hypersatellite structures. As the multiple ionization cross section varies as Z^2, where Z is the atomic number of the projectile, the satellite and hypersatellite yields resulting from atomic collisions with heavy ions are much higher than those produced by photon and electron impact. However, to unravel the complex structure of HI-induced X-ray spectra, the use of high-resolution detectors such as crystal spectrometers is mandatory. The first observation of Kα hypersatellites originating from heavy ion-atom collisions was reported by Richard *et al.* [117]. This pioneering work was followed by few other studies [25, 118–121]. Some high-resolution measurements of L- and M-hypersatellites of mid-heavy and heavy elements [26–28] were also performed.

Energies of hypersatellite transitions are more sensitive than diagram transitions to the Breit interaction, quantum electrodynamics (QED) corrections and relativity effects. Precise energy measurements of hypersatellite X-rays are therefore very useful to probe the goodness of atomic structure calculations. From the hypersatellite-to-diagram line yield ratios, the double-to-single K-shell ionization cross section ratios can be derived for the investigated HI-atom collisions. This permits to check the reliability of the predictions from different theoretical models such as the SCA (Semi-Classical Approximation) and CTMC (Classical Trajectory Monte-Carlo (CTMC) models. Well established double K-shell ionization cross sections are also needed for the interpretation of the X-ray radiation from the Universe [21], for plasma diagnostics [20], for the development of new X-ray sources [122] and also for the understanding of the X-ray emission from matter irradiated by photon beams of extreme fluences such as XFEL beams [108]. The $K\alpha_1^h$ hypersatellite corresponds to the spin-flip transition ($^1S_0$-$^3P_1$) which is forbidden by the E1 selection rules in the pure LS-coupling scheme. The $K\alpha_1^h$ transition is, however, allowed in the jj-coupling scheme. The $K\alpha_2^h$ hypersatellite corresponds to the transition ($^1S_0$-$^1P_1$) which is allowed by the E1 selection rules in both coupling schemes. As a consequence, the $K\alpha_1^h/K\alpha_2^h$ intensity ratio allows to probe the intermediacy of the coupling scheme across the periodic table [17, 18]. A further interest of hypersatellite X-ray lines resides in their natural line widths from which the mean lifetimes of double $1s$ vacancy states can be derived and compared to theory.

In the present study, the $K\alpha$-hypersatellite X-ray spectra of Ca, V, Fe and Cu bombarded by fast C and Ne ions were measured in high energy-resolution. For the two lightest elements, the $K\beta$-hypersatellites could be also observed. Ca and three $3d$ elements were chosen as target samples because for these elements some experimental photon and electron hypersatellite data were available, while HI hypersatellite information is still scarce in this part of the periodic table.

The chapter is organized as follows: in the next section the experimental setup used for the measurements is presented. The third section concerns the data analysis and, in particular, the problems encountered during the analysis of the complex X-ray spectra and the adopted solutions. Results concerning the energies, line widths and double $1s$ ionization cross sections are presented and discussed in the fourth section, whereas the main results of this work and their significance are summarized in the fifth section.

III.2 Experiment

The experiment was carried out at the Paul Scherrer Institute (PSI) in Villigen, Switzerland, within a collaboration with the group of Prof. M. Budnar from the Jozef Stefan Institute of Ljubljana. The Ca, V, Fe and Cu K-shell single and double vacancy states were produced by bombarding the samples with 12 MeV/amu carbon and 9 MeV/amu neon beams. The sample X-ray emission was measured by means of high resolution X-ray spectroscopy using the von Hamos curved crystal spectrometer of Fribourg [38].

III.2.1 Spectrometer

In the von Hamos geometry (see Fig. **??**), the X-ray emission from the target is diffracted by a cylindrically bent crystal and the diffracted beam is collected with a position sensitive detector. The crystal views the target through a narrow vertical rectangular slit which is kept fixed in space and represents the effective source of radiation. The latter is thus a line-like source having the same dimensions as the slit. The slit, front plane of the detector and axis of curvature of the crystal are all located in the same vertical plane. The dispersion axis of the spectrometer is parallel to the crystal curvature axis, whereas the cylindrical crystal curvature provides a vertical focusing of the diffracted beam, which permits to increase drastically the collection efficiency of the diffracted X-rays.

For a single position of the crystal and detector, a certain angular range is subtended by the crystal so that a several tens of eV wide energy domain can be measured with the von Hamos spectrometer in a scanless mode of operation. The covered energy domain is limited mainly by the length ℓ_{det} (in the direction of dispersion) of the employed position-sensitive detector. For a given Bragg angle ϑ the energy range δE covered by the spectrometer is given approximately by:

$$\delta E \cong \frac{\ell_{det}}{4R} \cdot \sin(2\vartheta) \cdot E, \tag{III.1}$$

where R stands for the distance (measured perpendicularly to the dispersion axis) between the crystal and detector surfaces, i.e., the radius of curvature of the crystal, and E the energy of the measured X-rays. To cover a wider energy domain, the central Bragg angle is modified by translating the crystal and the detector along axes which are parallel to the direction of dispersion, the translation distance of the detector being twice that of the crystal.

For each crystal-detector translation, the target is also moved along an axis perpendicular to the dispersion axis so that the target remains aligned with the slit center to crystal center direction. Furthermore, the target displacement and the orientation of the slit around its vertical axis are mechanically correlated so that the slit is always perpendicular to the target-to-crystal direction. Note that the target being placed behind the slit, the target width seen by the crystal depends on the target alignment with respect to the slit-crystal direction and is significantly bigger than the slit width. This may also contribute to enhance the spectrometer luminosity in the case where the incoming particle beam is rather wide like in the present experiment. The crystal, detector and target translations as well as the target alignment are carried out by means of remote-controlled stepping motors with a sensitivity of 5 μm for the crystal and detector translation, 2.5 μm for the target translation and 0.225° for the target alignment.

For the present experiment, the spectrometer was equipped with two crystals. For the Ca and V measurements, a LiF(200) crystal (2d = 4.0280 Å) was used while for the Fe and Cu measurements a $SiO_2(2\bar{2}3)$ crystal (2d = 2.7500 Å) was employed. The LiF(200) crystal plate was 9.9 cm high, 5 cm wide and 0.6 mm thick while the corresponding dimensions of the $SiO_2(2\bar{2}3)$ crystal were 10 cm x 5 cm x 0.4 mm. Both crystals were glued on aluminium blocks machined to a concave cylindrical surface with a radius of $R = 25.4$ cm. For the detection of the diffracted X-rays, a front illuminated deep depleted CCD camera was used. The CCD chip consisted of 1024 × 256 pixels with a pixel resolution of 27 μm and a depletion depth of 50 μm. The CCD camera was cooled down to -60 ^0C. For each sample several energy domains corresponding to different detector positions were needed to cover the whole energy range corresponding to the K X-ray spectrum. The detector positions were chosen so that neighbouring energy domains were partly overlapping.

III.2.2 Samples

The vanadium, iron and copper targets consisted of thin 20 mm high x 6 mm wide metallic foils with purities of 99.8+%, 99.85% and 99.97%, respectively. For calcium, thin foils were prepared by laminating 99.0% pure lumps with an in-house roller press until the appropriate thickness was reached. The obtained samples were then cut to have the same dimensions as the metallic foils. As calcium is highly hygroscopic and reacts with moisture contained in air, the calcium samples were stored in vacuum until they were mounted on the target holder in the spectrometer chamber. For the measurements, each target was tilted around a vertical axis passing through the target center so that the normal to the target front surface coincided with the bisector of the angle between the incoming heavy-ion beam and the slit-to-crystal direction. This target alignment was kept at the same value for the whole K X-ray spectrum of a given target so that the $K\alpha$ and $K\beta$ diagram and hypersatellite lines were all measured with the same angle between the incoming beam and the target surface.

The hypersatellite transitions of interest being rather weak as compared to their parent diagram transitions, hypersatellite spectra with a good enough statistics needed the use of thick enough samples. Too thick samples, however, would have led to large particle energy losses with two adverse side effects: first an overheating of the targets whose temperature could reach the melting point and secondly difficulties in the interpretation of the results due to the strong variation of the heavy-ion energy in the sample (see next Sect.). As the ionization cross section varies non linearly with the projectile energy, a meaningful comparison with theory requires indeed that the average projectile energy in the sample E_{av} remains reasonably close to the incident energy E_{in}. Thus, the target thicknesses were chosen (see Table III.1) as a compromise between a high enough intensity of the sample X-ray emission and a reasonably small loss of the projectile energy in the sample.

Table III.1 – Target thicknesses [mg/cm^2]

Projectile	Calcium	Vanadium	Iron	Copper
C^{4+}	6.41	16.94	16.95	17.11
Ne^{6+}	1.86	2.94	3.15	2.61

III.2.3 Heavy-ion beams

The C^{4+} and Ne^{6+} ions produced by a 10-GHz CAPRICE ECR source were injected into the variable energy Philips cyclotron of PSI and accelerated to final energies of 143.0 MeV and 179.0 MeV, respectively. The intensity of the heavy-ion beams was in the range of 100–200 nA. The beam spot size on the targets was typically 9 mm-high and 6 mm-wide. During the deceleration of the heavy ions in the samples, the remaining electrons of the projectiles were removed so that the investigated collisions can be considered as collisions between neutral atoms and fully stripped heavy ions.

The specific energy loss dE/ds of the projectiles in the target was parametrized by means of the following relation:

$$\frac{dE}{ds} = -c \cdot E^{-\nu}. \tag{III.2}$$

The constants c and ν were deduced from a double logarithmic interpolation of specific energy loss values computed with the *SRIM* code developed by Ziegler and Biersack [123]. The energy of the projectile after a penetration depth s can be deduced from Eq. III.2:

$$E(s) = [E_{in}^{\nu+1} - c(\nu+1) \cdot s]^{\frac{1}{\nu+1}}, \tag{III.3}$$

so that the energy of the emerging projectiles is given by:

$$E_{out} = E(s = \frac{h}{\rho \cdot cos\phi}), \tag{III.4}$$

where h is the target thickness in $[g/cm^2]$, ρ the target specific weight in $[g/cm^3]$ and ϕ the angle between the normal to the target surface and the direction of the incoming heavy-ion beam.

The average projectile energy in the sample depends on the single, respectively double, K-shell ionization cross section which in turn varies as a function of the projectile energy and on the photon mass absorption coefficient of the target for the X-ray transition of interest. The average energy of the projectiles in the target was determined using the following expression:

$$E_{av} = \frac{\int_0^{\frac{h}{\rho}} E(\frac{x}{cos\phi}) \cdot \sigma_{K,KK}[E(\frac{x}{cos\phi})] \cdot \exp[-\mu(E_X) \cdot \rho \cdot \frac{x}{sin(\vartheta+\phi)}]dx}{\int_0^{\frac{h}{\rho}} \sigma_{K,KK}[E(\frac{x}{cos\phi})] \cdot \exp[-\mu(E_X) \cdot \rho \cdot \frac{x}{sin(\vartheta+\phi)}]dx}, \tag{III.5}$$

where σ_K or σ_{KK} stands for the single or double K-shell ionization cross section and μ represents the mass absorption coefficient in $[cm^2/g]$ for the X-ray transition of interest of energy E_X. The cross sections σ_K and σ_{KK} were calculated within the SCA model using the code IONHYD of Trautmann and Rösel [124], whereas the mass absorption coefficients were taken from the NIST database XCOM [125].

Table III.2 – Energies of incoming and emerging projectiles for the four investigated targets as well as average energies corresponding to the X-ray transitions of interest. For details, see text.

Projectile	Target	Angle ϕ [deg]	E_{out} [MeV]	$E_{av}(K\alpha)$ [MeV]	$E_{av}(K\alpha^h)$ [MeV]	$E_{av}(K\beta)$ [MeV]	$E_{av}(K\beta^h)$ [MeV]
C	Ca	19.575	135.8	140.0	139.9	139.9	141.9
143.0 MeV	V	27.225	125.8	136.9	136.6	136.5	141.4
	Fe	24.525	125.5	136.2	136.0	135.8	140.6
	Cu	29.250	126.0	136.1	135.9	135.8	139.9
Ne	Ca	19.575	172.0	175.7	175.6	175.6	176.5
179.0 MeV	V	27.225	169.2	174.4	174.3	174.3	175.5
	Fe	24.525	168.5	174.0	174.0	173.9	174.9
	Cu	29.250	170.6	174.9	174.9	174.9	175.4

The so-obtained average energies are listed in Table III.2. One sees that for each collision type, the average energies corresponding to the $K\alpha$ and $K\beta$ diagram lines and the $K\alpha^h$ hypersatellites are nearly the same. The average energies of the $K\beta$ hypersatellites are slightly bigger because the energies of these transitions lie above the K-absorption edges, which increases their self-absorption as compared to the other transitions. As a consequence, for $K\beta^h$ transitions the contribution to the observed intensity of the front part of the target, where the projectile energy is higher, is somewhat bigger than that of the rear part, which results into an increase of the average projectile energy.

As shown in Table III.2, the energy E_{out} of the emerging projectiles varies, depending on the target species and thickness, between about 125 MeV and 135 MeV for C and between 168 MeV and 172 MeV for Ne. To minimize the background due to the production of nuclear reactions in the beam stopper, the latter was made of Pb. For this heavy element, the threshold energies (Coulomb barriers) for nuclear reactions lie indeed relatively high (72 MeV and 114 MeV for the C and Ne projectiles, respectively) so that the nuclear cross sections for the above mentioned emerging projectile energies are far below their maximum. In addition, the beam stopper was placed reasonably far from the CCD detector (see Fig. III.1) and a supplementary γ-ray shielding was installed between the beam dumper and the CCD detector.

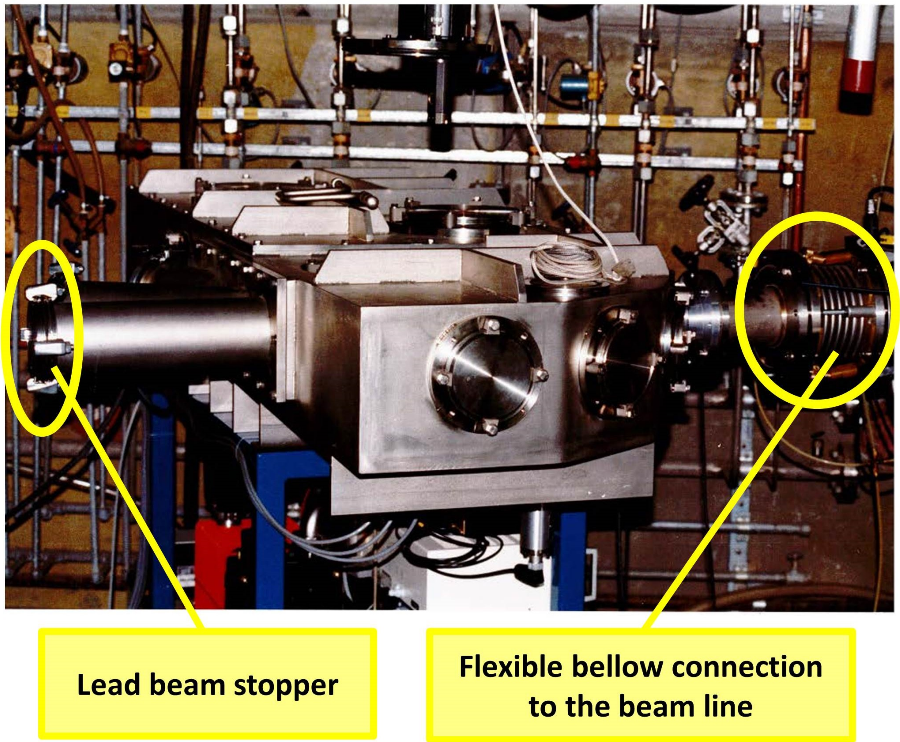

Figure III.1 – Photograph of the von Hamos spectrometer as installed in the experimental hall A of the Philips variable energy cyclotron of PSI. The cartoon bubble on the left shows the location of the lead beam stopper and the one on the right the connection of the spectrometer chamber to the beam line via a flexible bellow.

III.3 Data analysis

III.3.1 Energy calibration and instrumental broadening

Energy calibration of the spectrometer

For the energy calibration of the von Hamos spectrometer, measurements of the photoinduced $K\alpha_{1,2}$ diagram transitions of the four samples were performed. The sample fluorescence was produced using the Bremsstrahlung from a Cr anode side-window X-ray tube. The reference energies of 3691.719(49) eV, 4952.916(59) eV, 6404.0062(99) eV and 8047.8227(26) eV reported in [30] for the $K\alpha_1$ transitions of Ca, V, Fe and Cu, respectively, were assigned to the fitted centroids of the corresponding X-ray lines. The energy calibration of the heavy-ion-induced X-ray spectra was then performed using the following formula:

$$E_i = \frac{n}{n_o} \cdot \frac{\tan(\vartheta_o)}{\tan(\vartheta_i)} \cdot \sqrt{\frac{1 + [\tan(\vartheta_i)]^2}{1 + [\tan(\vartheta_o)]^2}} \cdot E_o, \tag{III.6}$$

where E_i represents the energy corresponding to the pixel p_i, n and n_0 are the diffraction orders with which the X-ray spectrum to be calibrated and reference X-ray line were measured, and ϑ_o and ϑ_i stand for the Bragg angles related to the fitted centroid pixel p_0 of the reference X-ray line and pixel p_i of the heavy-ion-induced spectrum. The Bragg angles are given by:

$$\tan(\vartheta_0) = \frac{2 \cdot R}{x_{det,0} - (512 - p_0 \cdot b) \cdot w_{pixel}} \tag{III.7}$$

and

$$\tan(\vartheta_i) = \frac{2 \cdot R}{x_{det} - (512 - p_i \cdot b) \cdot w_{pixel}}, \tag{III.8}$$

where x_{det} and $x_{det,0}$ correspond to the distances between the slit and CCD center for the CCD positions corresponding to the measurements of the heavy-ion spectrum and reference line, respectively, b represents the binning factor (see next subsection, $b = 1$ for the case of no binning) and w_{pixel} stands for the pixel size.

Instrumental broadening

For all samples the instrumental response was found to be well reproduced by a Gaussian function. The Gaussian width of the instrumental response is mainly due to the slit width, the Darwin width and/or crystal mosaicity and the spatial resolution of the detector. The slit width affects the instrumental resolution and luminosity of the spectrometer in opposite ways. In this experiment, a slit width w_{slit} of 0.2 mm was thus adopted as a compromise between a high enough energy resolution and acceptable luminosity. The contribution of the slit width and CCD pixel size to the energy resolution of the spectrometer are given by the relations II.3 and II.4 presented in the Sect. II.6.

Actually, the instrumental energy broadening was not calculated but determined experimentally from the fits of the above-mentioned X-ray tube-based measurements. The $K\alpha_1$ diagram X-ray transitions taken as references were fitted with Voigt functions. In the fits, the Lorentzian natural line widths were kept fixed at the values recommended by Campbell and Papp [33], whereas the standard deviations σ of the Gaussians representing the instrumental response of the spectrometer were used as free fitting parameters. The values of σ obtained from the fits are listed in Table III.3.

Table III.3 – Experimental broadening parameter σ in [eV] as determined from the fits of the $K\alpha_1$ transitions used for the energy calibration

Projectile/Crystal	Calcium	Vanadium	Iron	Copper
C^{4+}/LiF (200)	0.699(7)	1.152(13)		
C^{4+}/SiO$_2$(2$\bar{2}$3)			0.943(20)	1.444(18)
Ne^{6+}/LiF (200)	0.718(4)	1.222(11)		
Ne^{6+}/SiO$_2$(2$\bar{2}$3)			0.956(15)	1.341(17)

One can see in Table III.3 that, except in one case, the instrumental broadenings σ measured during the Ne experiment are slightly bigger than those determined during the C experiment and not consistent with the latter within the combined errors. This is possibly due to the fact that the slit was a little bit more open during the second experiment which was performed about one year later.

As the instrumental broadening is expected to vary smoothly with the photon energy, a linear function was assumed for $\sigma(E)$. Thus, for each crystal the latter was approximated by a straight line defined by the points $(E_{K\alpha1(Ca)}, \sigma_{Ca})$ and $(E_{K\alpha1(V)}, \sigma_V)$ for the $LiF(200)$ crystal and $(E_{K\alpha1(Fe)}, \sigma_{Fe})$ and $(E_{K\alpha1(Cu)}, \sigma_{Cu})$ for the $SiO_2(2\bar{2}3)$ crystal.

The FWHM energy resolution ΔE=2.35·σ corresponding to the average values of the standard deviations quoted in Table III.3 is depicted for both crystals in Fig. III.2 together with the calculated energy broadening contributions due to the slit width and spatial resolution of the CCD detector. As shown in Fig. III.2, the energy broadening originating from the CCD is about 10× smaller than the one due to the slit. For this reason, the 27 μm resolution of the CCD detector was not really needed and a software binning of four adjacent column pixels was performed off-line in order to obtain higher count rates in the one-dimensional energy spectra.

It is also interesting to note that the slit and CCD contributions represent together almost 90% of the total experimental broadening for the $SiO_2(2\bar{2}3)$ crystal and only about 60% for the LiF(200) crystal. This is due to the fact that for the LiF(200) crystal the Darwin width is significantly bigger than the one of the $SiO_2(2\bar{2}3)$ crystal. For instance at 6 keV, the Darwin widths of the two crystals amount to 37.3 μrad and 11.8 μrad, respectively. In addition, whereas quartz can be considered as a perfect crystal, the LiF crystal is partly mosaic, which contributes to further increase the contribution of the crystal to the observed total broadening.

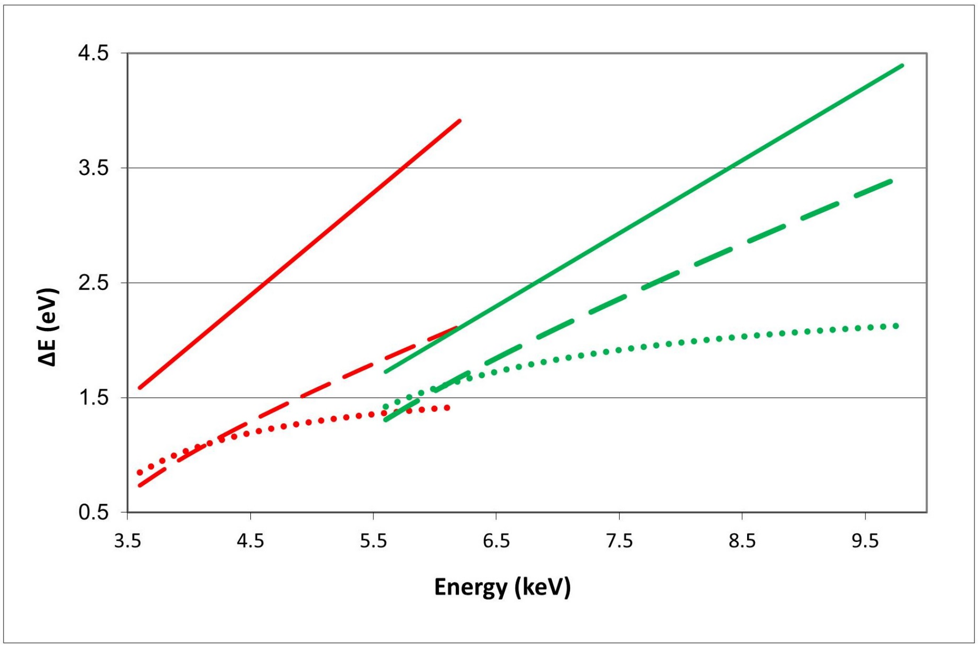

Figure III.2 – FWHM energy resolution of the von Hamos spectrometer as a function of the photon energy for the LiF (200) (red solid line) and $SiO_2(2\bar{2}3)$ (green solid line) crystals. The slit (red and green dashed lines) and CCD (red and green dotted lines) contributions are also depicted. Note that the CCD contribution is multiplied by 10.

III.3.2 Data correction and normalization

Beam intensity

The beam intensity was monitored by measuring the $K\alpha, \beta$ x-ray emission of the target with a 500 μm-thick Si PIN photodiode. The latter was placed on the crystal support above the crystal so that it viewed the target through the slit as the crystal. For each sample, the photodiode was oriented so that its entrance window was perpendicular to the direction defined by the slit and crystal center. In the ADC spectrum of the photodiode, an energy window was set on the $K\alpha, \beta$ x-ray lines of the target and the x-ray yields collected in this window served to monitor the beam intensity. Furthermore, a gate was set on the ADC to control the photodiode data acquisition. Actually this gate trigged by the CCD shutter signal blocked the photodiode data acquisition when the CCD shutter was closed. Thus, data were collected synchronously with the CCD detector and the photodiode. For each target, the x-ray yields of the partial spectra corresponding to consecutive CCD positions were normalized to the intensity of the first energy region using the $K\alpha, \beta$ yields measured by the photodiode for the different regions.

To take under control the possible neutron activation of the spectrometer chamber by the neutrons produced in the beam stopper, a neutron detector was placed behind the latter. The number of neutrons collected during each measurement corresponding to a particular CCD position was also used to crosscheck the $K\alpha, \beta$ X-ray-yield provided by the photodiode for this measurement.

Beam profile

A simple ray-tracing shows that in the von Hamos slit geometry, the different pixels' columns of the CCD detector do not see the same part of the sample, the pixels' columns of the left part of the CCD viewing the right part of the sample and vice-versa. If the intensity distribution of the heavy-ion beam is not homogeneous, the inhomogeneity is reflected in the X-ray yields measured by the CCD, which can distort the shape of the measured X-ray spectrum. However, if the beam intensity profile along the transverse direction is known, the CCD spectrum can be corrected by normalizing the intensity of each column of pixels to the intensity of a column of pixels taken as reference using the ratio of the beam intensities integrated over the profile intervals viewed on the target by the column of interest and the column of reference.

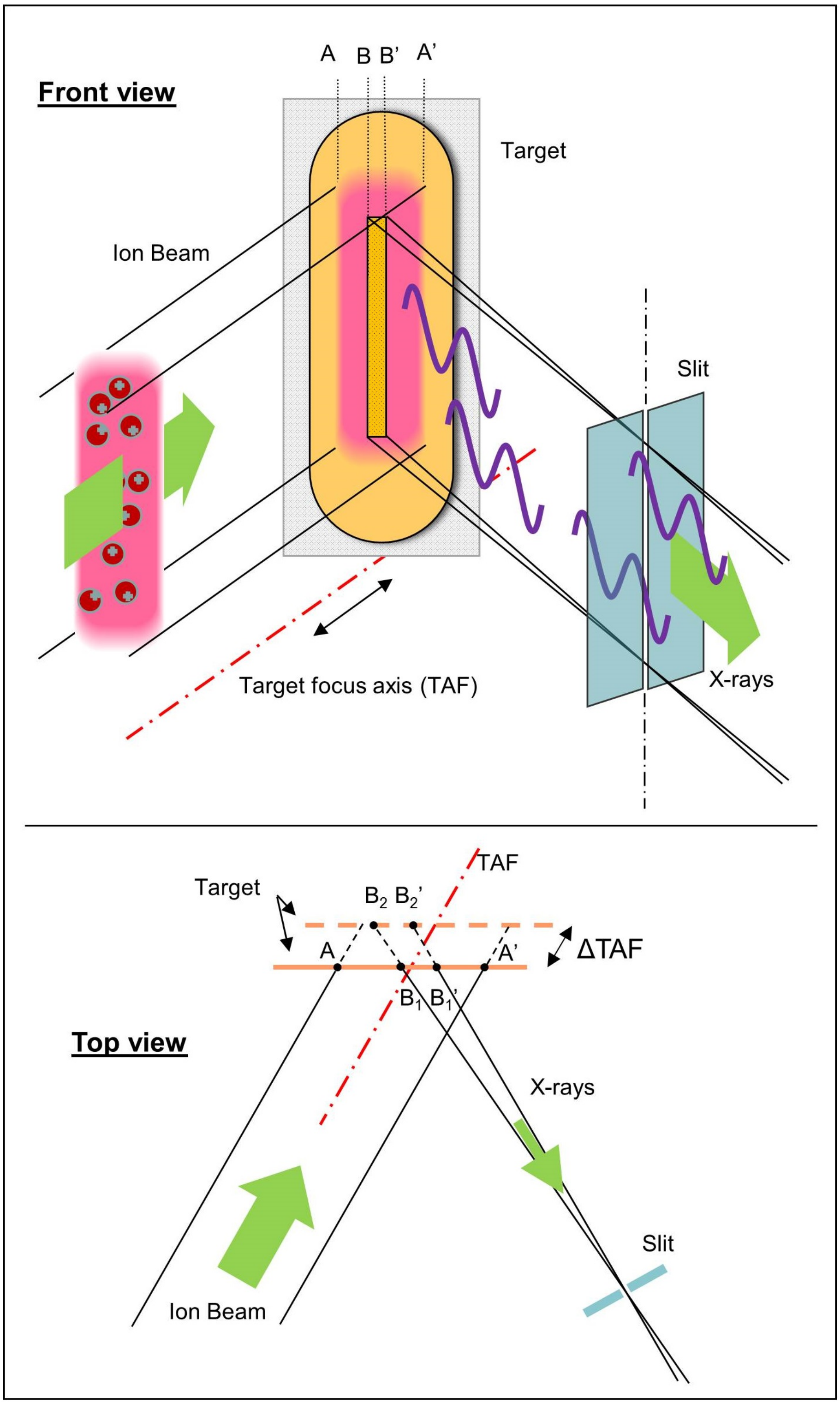

Figure III.3 – Schematic representation of the target regions corresponding to the beam impact and to the area viewed by the crystal through the slit. The target focus axis (TAF) is parallel to the direction of the incoming beam. When moving the target along this axis, the surface viewed by the crystal changes from (B_1B_1') for the 1st position of the target to (B_2B_2') for the 2nd position, while the activated sample area remains the same (AA').

The beam intensity profile was determined with the von Hamos spectrometer itself. A narrow vertical stripe covering the $K\alpha_1$ X-ray line was first selected on the CCD. Then, the integrated intensity of this CCD stripe was measured for several successive positions of the sample moved along the direction of the beam. As shown in Fig. III.3, moving the sample along the beam axis and measuring the sample X-ray emission at a constant Bragg angle amounts indeed to probing the horizontal distribution of the beam intensity. The so-obtained intensity points were then interpolated with a polynomial. The left and right limits of the profile interval seen by each column of pixels were determined with an ray-tracing code for all detector positions needed to cover the whole K X-ray spectrum of the considered sample. For illustration, the beam intensity profile corresponding to the carbon-calcium collision is depicted in Fig. III.4 together with the profile intervals seen by the pixels' columns 1 and 1024 for the first and ninth detector positions. The spacing between the two intervals corresponding to the first region is bigger than the one of the ninth region, because the distance between the slit and the crystal center is smaller for the 1^{st} region than for the 9^{st} one.

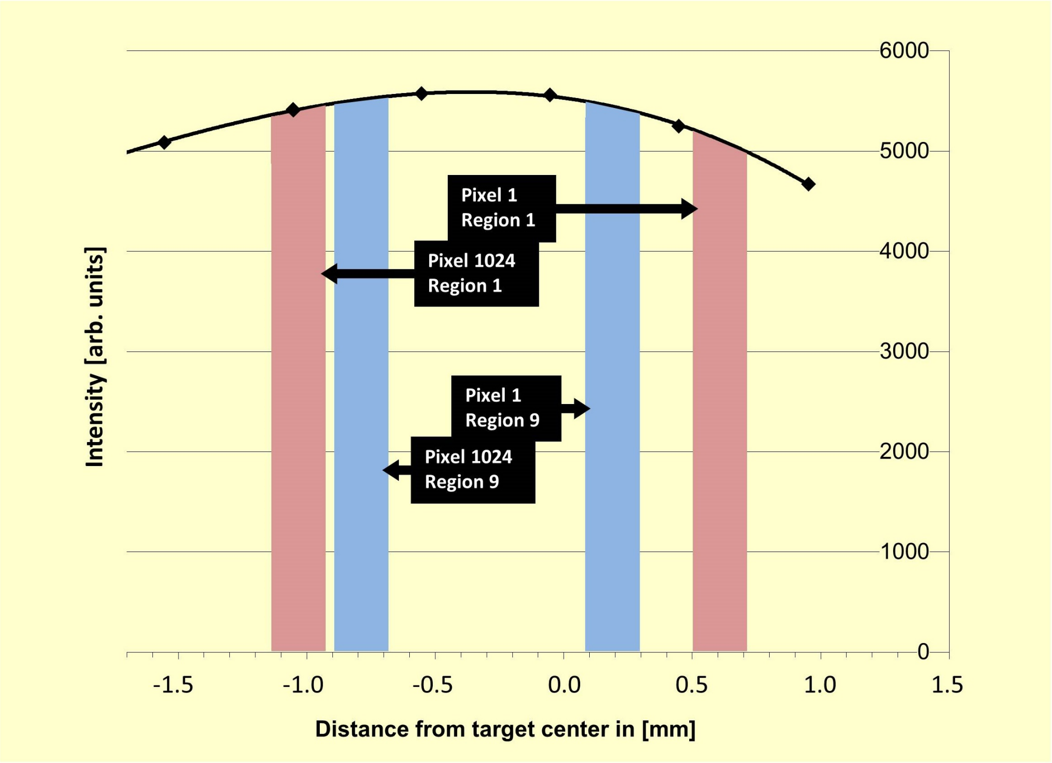

Figure III.4 – C beam intensity profile employed to correct the $K\alpha$ X-ray spectrum of Ca shown in Fig. III.5. The red and blue vertical stripes represent the target areas seen by the pixels' columns 1 and 1024 for the CCD positions 1 (3650 eV-3750 eV) and 9 (4350 eV–4450 eV).

The correction for the inhomogeneity of the beam intensity presented above is reliable providing the following two assumptions are satisfied. First, short-time fluctuations of the beam intensity and position are negligible and, second, the active surface of the target is not (or only very slowly) damaged by the beam impact. Both assumptions were checked and, in fact, we observed that slow drifts of the beam position and small intensity variations did exist. To minimize the size of the resulting systematic errors, relatively short measurements of the whole K X-ray spectra were performed. These measurements were repeated several times and the different scans were then summed together, leading to a smoothing of the beam fluctuation effects. Furthermore, measurements of the beam intensity profile were performed periodically.

Solid angle and effective size of the target

In the von Hamos geometry the solid angle of the spectrometer varies with the Bragg angle and the one-dimensional energy spectra corresponding to the sums of the filtered two-dimensional CCD images projected onto the dispersion axis have to be corrected to account for this variation. For a given Bragg angle, i.e., photon energy, the solid angle reads:

$$\Omega(E) = \int_{-\Delta\vartheta_D(E)/2}^{\Delta\vartheta_D(E)/2} \int_{\alpha_{min}(E)}^{\alpha_{max}(E)} \sin(\theta) d\theta d\psi. \tag{III.9}$$

In the above formula, $\alpha_{min}(E)$=$[\pi - \alpha_{av}(E)]/2$, $\alpha_{max}(E)$=$[\pi + \alpha_{av}(E)]/2$ and $\Delta\vartheta_D(E)$ represents the Darwin width for the photon energy E. The angle $\alpha_{av}(E)$ is defined by:

$$\alpha_{av}(E) = 2 \cdot \arctan[\frac{h_{av}(E)}{2 \cdot l(E)}], \tag{III.10}$$

where h_{av} represents the average height of the crystal seen by the active part of the target contributing to the production of the observed fluorescence and the length l is defined by:

$$l(E) = \frac{R}{sin[\vartheta(E)]} + \frac{d}{cos[\vartheta(E)]}, \tag{III.11}$$

where R is the radius of curvature of the crystal, d the distance from the slit to the TAF-axis and ϑ the Bragg angle.

The Darwin widths were calculated with the version 2.3 of the computer code XOP (X-Ray Oriented Programs) [126]. In the calculation of the solid angle, the height h of the crystal was replaced by h_{av} because, depending on the detector position, some points of the target may not see the full height of the crystal but only a part of it. To calculate $h_{av}(E)$, the vertical coordinates $z_{t,max}(E)$ and $z_{t,min}(E)$ of the target points seen by the top and bottom pixels of the considered CCD column were first calculated. The height $h_t(E)$=$z_{t,max}(E)$-$z_{t,min}(E)$ was compared to the height of the beam spot h_{beam} and the effective height of the radiation source $h_{eff}(E)$ was determined by the condition $h_{eff}(E)$=Min$[h_t(E), h_{beam}]$. The effective source height $h_{eff}(E)$ was then divided into 1000 small vertical segments and the crystal height seen by each segment considered as a point-like source was computed. Finally, h_{av} was determined by calculating the average value of the 1000 partial heights. For example, the average heights calculated for the centroids of the $K\alpha$ diagram line and $K\alpha^h$ hypersatellite of Ca measured with the LiF(200) crystal were found to be 5.24 cm and 5.72 cm, respectively and the corresponding solid angles 12.1 μsr and 10.1 μsr. It can be noted that, in spite of $h_{av}(E^h_{K\alpha}) > h_{av}(E_{K\alpha})$, the solid angle corresponding to the $K\alpha^h$ hypersatellite is smaller than the one of the $K\alpha$ diagram line. This is due to the fact that $l(E^h_{K\alpha}) > l(E_{K\alpha})$ and $\Delta\vartheta_D(E^h_{K\alpha}) < \Delta\vartheta_D(E_{K\alpha})$.

As mentioned above, the effective height of the radiation source varies as a function of the photon energy, i.e., the Bragg angle ϑ. The same holds for the source width $w_{eff}(E)$. The latter is given by:

$$w_{\mathit{eff}}(E) = \frac{w_{slit}}{\sin[\vartheta(E) + \phi]}. \tag{III.12}$$

The effective area of the photon source is then:

$$S_{\mathit{eff}}(E) = h_{\mathit{eff}}(E) \cdot w_{\mathit{eff}}(E). \tag{III.13}$$

Finally, to account for the variation of the solid angle and effective source size as a function of the photon energy, each point of the measured spectra was multiplied by the normalization factor $F_{\Omega,S_{eff}}(E)$ defined by:

$$F_{\Omega,\mathsf{S}_{\mathit{eff}}}(E) = \frac{\Omega(E_{ref}) \cdot S_{\mathit{eff}}(E_{ref})}{\Omega(E) \cdot S_{\mathit{eff}}(E)}. \tag{III.14}$$

where E_{ref} represents the energy corresponding to the pixel 512 of the first detector position. The distances l, Darwin widths $\Delta\vartheta_D$, solid angles Ω, effective source areas S_{eff} and normalization factors $F_{\Omega,S_{eff}}$ computed for the X-ray lines of interest are presented in Table III.4.

Table III.4 – Distance l, Darwin width $\Delta\vartheta_D$, solid angle Ω, effective source area S_{eff} and normalization factor $F_{\Omega,S_{eff}}$ for the X-ray lines of interest. The energy quoted in the 1^{st} row of each element stands for the energy corresponding to the reference pixel (pixel 512 of the 1^{st} detector position). For details, see text.

Crystal	Target	X-ray line	l [cm]	$\Delta\vartheta_D$ [μrad]	Ω [μsr]	S_{eff} [mm^2]	$F_{\Omega,S_{eff}}$
LiF	Ca	3715 eV	35.12	78.5	11.85	1.86	1.000
(200)		Kα	34.98	81.0	12.11	1.85	0.984
		Kα^h	36.17	64.3	10.15	1.89	1.149
		Kβ	37.01	57.8	9.27	1.92	1.238
		Kβ^h	38.81	59.1	9.53	1.97	1.174
	V	4970 eV	44.2	38.2	5.90	1.98	1.000
		Kα	44.04	37.8	5.85	1.98	1.009
		Kα^h	45.84	36.7	5.55	2.01	1.047
		Kβ	47.82	35.7	5.25	2.04	1.091
		Kβ^h	50.21	38.6	5.49	2.08	1.023
SiO_2	Fe	6442 eV	39.76	10.7	1.74	1.93	1.000
(2$\bar{2}$3)		Kα	39.54	10.9	1.77	1.92	0.988
		Kα^h	40.88	9.23	1.49	1.95	1.156
	Cu	8079 eV	48.47	5.40	0.793	2.02	1.000
		Kα	48.26	5.92	0.872	2.01	0.914
		Kα^h	49.86	5.40	0.778	2.04	1.009

Reconstruction of the spectra

As mentioned before, the whole energy range corresponding to the K-shell diagram and hypersatellite lines could not be measured with a single CCD position. Therefore, the full spectra were reconstructed by putting together the partial spectra measured at several consecutive and partly overlapping CCD positions, each partial spectrum having been normalized beforehand for the differences in acquisition times and beam intensities and corrected for the beam profile, solid angle and effective target size according to the procedures discussed above. In some cases, significant differences were found between the intensities of overlapping energy regions. These discrepancies are probably due to small variations of the beam intensity profile that occurred between two consecutive beam profile measurements.

In such cases, the $(n+1)^{th}$ spectrum was adjusted to the n^{th} one by multiplying it by a scaling factor determined from the difference of intensity between the two overlapping regions. For illustration, the reconstructed whole X-ray spectrum corresponding to the C^{4+}-Ca collision is depicted in Figure III.5 (top panel). The bottom panel shows the partial spectra corresponding to the nine different CCD positions needed to cover the full energy range of interest. In the energy range from 4250 eV to 4380 eV corresponding to the Kβ hypersatellite region, the statistical fluctuations are smaller because this region was measured with a significantly longer acquisition time.

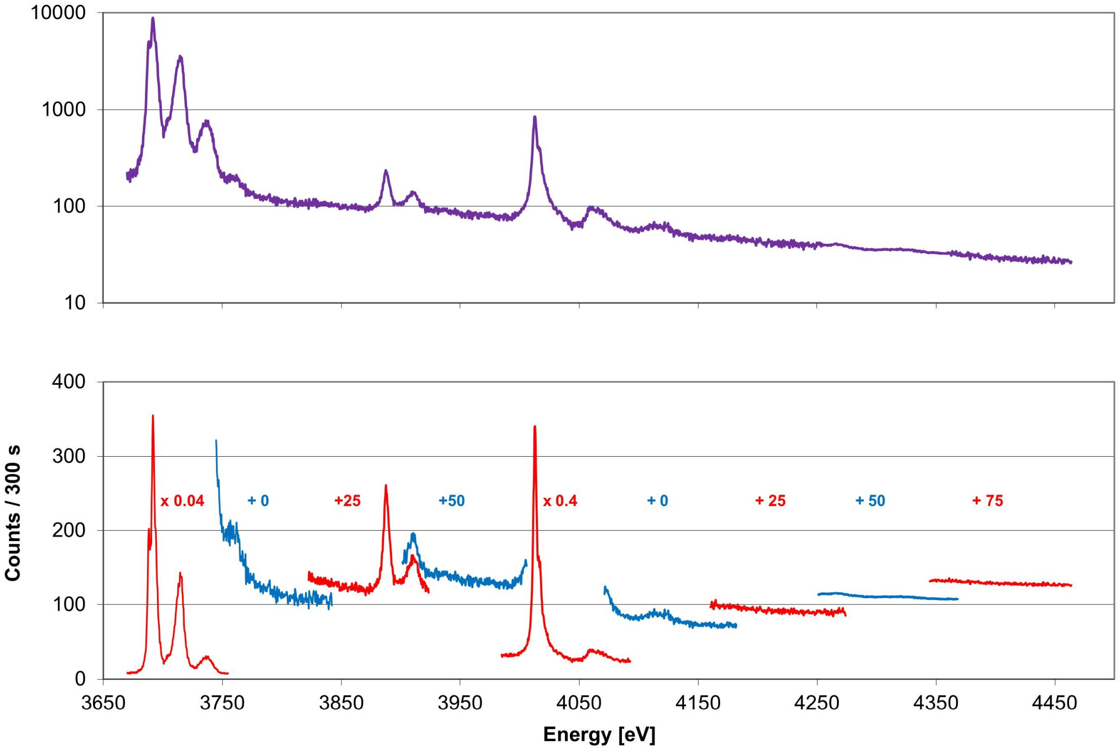

Figure III.5 – Reconstructed K X-ray spectrum of Ca produced by impact with 143 MeV C ions. In the top panel, the full spectrum is represented within the same logarithmic intensity scale. The partial spectra corresponding to the different CCD positions needed to cover the whole energy range are plotted in the bottom panel. In this case the intensity scale is linear but the intensities of the $K\alpha$ and $K\beta$ diagram lines were multiplied by 0.04 and 0.4, respectively, and offsets in the intensity scale were employed for the different regions to better show the overlapping regions.

III.3.3 Fitting procedure

General considerations

The spectra were analyzed by means of a least squares fit method using the software package PeakFit®. As the natural line shape of an X-ray transition corresponds to a Lorentzian function and the instrumental broadening can be well reproduced by a Gaussian, Voigt profiles which result from the convolution of Gauss and Lorentz functions [49] were employed to reproduce the shapes of the measured X-ray lines.

For each spectrum, the energies, Lorentzian widths and intensities of the measured lines as well as the parameters of the linear background were used as free fitting parameters, whereas the standard deviation of the instrumental response was kept fixed at the value detemined by interpolation from the known linear function $\sigma_{instr}(E)$ (see Sect. III.3.1). However, due to the number of transitions to be analyzed in each spectrum and the intensities of the transitions of interest which covered several orders of magnitude, convergence problems were encountered during the fitting procedure. In order to circumvent these difficulties, the following steps were taken.

The reconstructed spectra were divided into two or more parts containing structures of comparable intensities. The energies and Lorentzian widths of the most intense X-ray lines were first extracted by fitting the first part of the spectrum and the obtained values were then used as fixed parameters in the fit of the other parts. Finally the whole spectrum was fitted simultaneously while releasing progressively the previously fixed parameters. Such an iterative procedure allowed us to obtain in most cases a steady convergence of the fits.

The goodness of the fits was probed by comparing the obtained intensity ratios I($K\alpha_2$)/I($K\alpha_1$) to the values quoted in the Tables of Scofield [50]. The same was done for the I($K\beta_{1,3}$)/I($K\alpha_{1,2}$) yield ratios. In this case, however, the intensities of the $K\beta_{1,3}$ transitions were corrected beforehand for the change of the target self-absorption, crystal peak reflectivity and CCD efficiency (see Sect. III.3.4). The natural widths of the diagram $K\alpha_1$ and $K\alpha_2$ lines were also kept fixed in these fits at the values recommended by Campbell and Papp [33]. This was necessary to get correct $K\alpha_{1,2}$ intensities because the close-lying M-satellite structures could not be resolved, the energy shifts of these satellites being smaller than the natural line widths of the parent diagram lines. The L-satellite structures were fitted using a number of components as small as possible in order to shorten the fitting time.

This was a reasonable choice since the L-satellite transitions did not represent the main interest of the present study.

In the fits of the photoinduced $K\alpha_{1,2}$ lines measured for the energy calibration of the spectrometer and the determination of the experimental broadening, slight asymmetries were observed on the low energy sides of the lines measured with the $LiF(200)$ crystal. Such asymmetries were already observed in prior experiments. They originate from the LiF crystal itself. The energy shifts, relative intensities and widths of the asymmetries could be well determined from the analysis of the calibration measurements and they were kept fixed in the fits of the heavy-ion-induced spectra of Ca and V.

To get reliable results for the intensities of the weak hypersatellites, a particular attention was devoted to the background in the fits of the hypersatellite spectra. The high-energy tails of the intense $K\alpha_{1,2}$ diagram and $K\alpha_{1,2}L^n$ satellite lines which occur below the $K\alpha^h$ hypersatellites as well as the low-energy tails of the $K\beta_{1,3}$ diagram and $K\beta_{1,3}L^n$ satellite lines which occur above were included in the fits, keeping their energies, widths and intensities at the values provided by the fits of the corresponding regions.

M-satellites which are not resolved from their parent diagram lines but appear as slight asymmetries on the high energy sides of the latter were considered in the fits of the diagram lines with additional Voigtians. The energy separation between the $(n+1)^{th}$- and n^{th}-order M-satellites was assumed to be nearly constant for any n-value and equal to the energy difference between the 1^{st} order M-satellite and the parent diagram line. The latter energy difference was deduced from the corresponding photoinduced spectrum where 1^{st} order M-satellites were also observed as a result of shake processes. The intensity of the 1^{st} order M-satellite was let free in the fit while the relative intensities of the higher-order satellites were kept fixed at values determined from the intensity of the first satellite assuming a binomial distribution for the M-satellite yields.

$K\alpha_1^h$ hypersatellites are forbidden by the electric-dipole selection rules in the L-S coupling scheme. As this scheme prevails for light elements, $K\alpha_1^h$ hypersatellites are significantly weaker than $K\alpha_2^h$ hypersatellites for low-Z elements as those investigated in the present experiment. For this reason, the $K\alpha_1^h$ lines were difficult to extract from the background and the partly overlapping $K\alpha_2^hL$ satellite structure, in particular for Ca and V. Good initial guess values which were taken from available literature references were thus needed for the energies and relative intensities of these weak transitions. The guess values were first kept fixed in the fitting procedure and, whenever possible, let free in subsequent iterations.

Specific points concerning the fitting of the spectra corresponding to the different collisions are given hereafter.

Collision $\mathbf{C^{4+} \to Ca}$

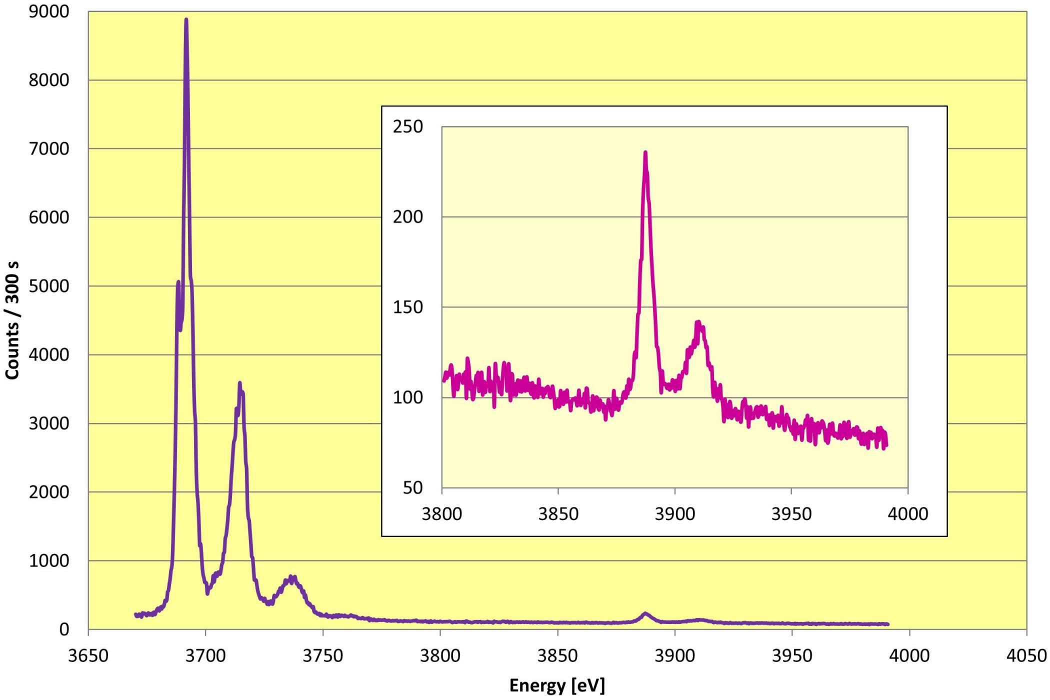

Figure III.6 – C-induced $K\alpha$ spectrum of Ca. The hypersatellite region is shown enlarged in the inset.

The measured $K\alpha$ spectrum is depicted in Fig. III.6. From the left to the right, one can distinguish the $K\alpha_{1,2}$ diagram line doublet, the $K\alpha_{1,2}L^1$ (at about 3720 eV) and $K\alpha_{1,2}L^2$ (3740 eV) satellites and the $K\alpha_2^h$ hypersatellite (3890 eV). The weak bump around 3760 eV corresponds to the 3^{rd} order L-satellite and the second peak in the hypersatellite region to the overlapping $K\alpha_1^h$ hypersatellite and $K\alpha_2^hL^1$ hypersatellite-satellite. As mentioned before, the natural widths of the $K\alpha_1$ and $K\alpha_2$ lines were kept fixed in the fit at the values recommended by Campbell and Papp [33]. This was needed to analyse properly the unresolved M-satellite structure. The latter could be well reproduced by two Voigtians.

The fit of the hypersatellite region is shown in Fig. III.7. The well defined Kα_2^h hypersatellite line was fitted with one Voigtian whose energy, intensity and Lorentzian width were used as free fitting parameters. The second bump around 3910 eV was

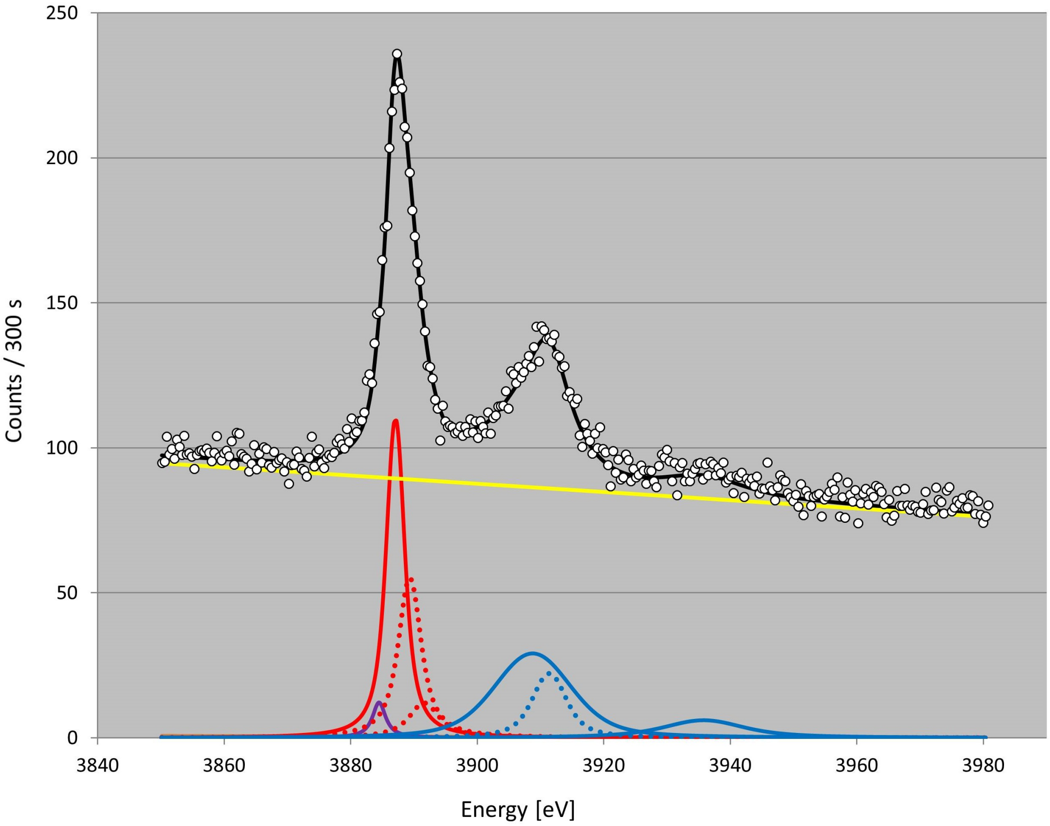

Figure III.7 – Fit of the C-induced $K\alpha$ hypersatellite spectrum of Ca. The top part of the Fig. shows the measured spectrum (open circles) and the total fit (black curve). The fitted components are depicted in the lower part where the red solid line represents the $K\alpha_2^h$ hypersatellite, the red dotted lines the unresolved 1^{st} and 2^{nd} order M-satellites and the blue solid lines the 1^{st} and 2^{nd} order L-satellites of the $K\alpha_2^h$ hypersatellite. The complex satellite structure corresponding to the decay of quadruple $K^{-2}L^{-1}M^{-1}$ vacancy states was fitted with a single Voigtian (blue dotted line). The violet line on the low energy side of the $K\alpha_2^h$ hypersatellite accounts for the asymmetric response of the LiF crystal (see text). The Voigtian corresponding to the extremely weak $K\alpha_1^h$ hypersatellite (at about 3904 eV) cannot be seen within the employed intensity scale.

fitted with two Voigtians, one for the $K\alpha_2^hL$ hypersatellite satellite and another one for the multiplet transitions decaying $K^{-2}L^{-1}M^{-1}$ multi-vacancy states. A single Voigtian was used to fit the $K\alpha_1^h$ hypersatellite. However, due to the very small intensity of this line, only the energy could be let free. The Lorentzian width was kept fixed at the same value as the one of the Kα_2^h hypersatellite using the *share* option provided by the PeakFit® program, and its intensity was fixed to 2.3% of that of the the Kα_2^h transition according to the theoretical intensity ratio

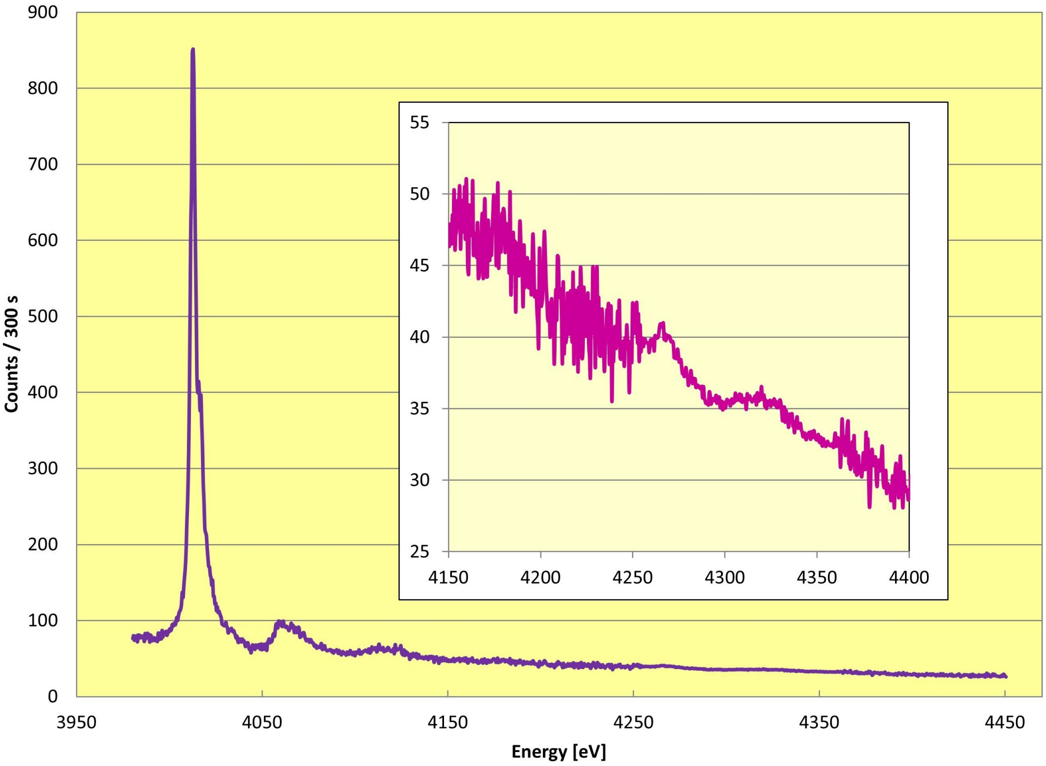

Figure III.8 – C-induced $K\beta$ spectrum of Ca. The hypersatellite region is shown enlarged in the inset.

reported in Ref. [127].

The $K\beta$ spectrum is shown in Fig. III.8. The strongest line corresponds to the $K\beta_{1,3}$ diagram line. The asymmetry on the high-energy side is due to the unresolved M-satellites. The asymmetry is more pronounced than the one observed for the $K\alpha$ line because the energy shift of M-satellites increases with the principal quantum number n of the transition electron in the initial state, i.e., n=2 for the $K\alpha_{1,2}$ transitions and n=3 for the $K\beta_{1,3}$ transitions. The second and third components which are visible correspond to the 1^{st} and 2^{nd} order L-satellites. They are much weaker than in the $K\alpha$ spectrum because they lie above the K-absorption edge (4038.5 eV) and are therefore strongly attenuated by the target self-absorption effect. The same holds for the $K\beta^h$ hypersatellite which is visible in the inset at about 4270 eV, whereas the component around 4320 eV corresponds to the 1^{st} order L-satellite of the $K\beta^h$ hypersatellite. The statistical fluctuations in the hypersatellite energy region (4250 eV-4350 eV) are smaller because for this region data were collected with a longer acquisition time.

In the fit of the $K\beta_{1,3}$ diagram line the Lorentzian width was first fixed at the value quoted in [33] and the M-satellite structure was fitted with three Voigtians, assuming a binomial distribution for the intensity of the 1^{st}, 2^{nd} and 3^{rd} order M-satellites. In the second fit iteration, the Lorentzian width of the diagram line was also released. In the analysis of the Kβ^h spectrum, all parameters except the known instrumental broadening were let free in the fit.

Collision Ne^{6+} → Ca

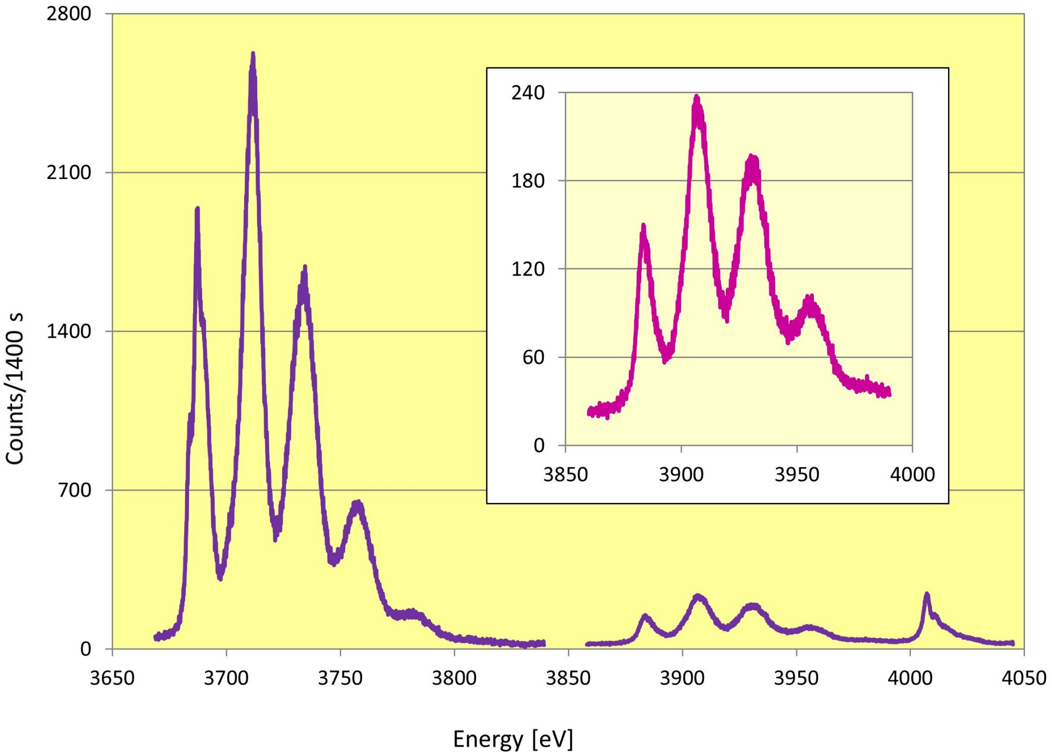

Figure III.9 – Ne-induced $K\alpha$ spectrum of Ca. The hypersatellite region is shown enlarged in the inset. The asymmetric peak at about 4010 eV corresponds to the $K\beta_{1,3}$ diagram line and its M-satellite structure. The region around 3850 eV was not measured.

The Ne-induced $K\alpha$ and $K\beta$ X-ray spectra of Ca are depicted in Fig. III.9 and Fig. III.10, respectively. As the multiple ionization cross section increases with the squared atomic number of the projectile, the observed L- and M-satellite structures are much stronger than in the corresponding C-induced spectra. As shown in Fig. III.9, the 1^{st} order L-satellite is even stronger than its parent $K\alpha$ diagram line. The same holds for the $K\alpha^h$ and $K\beta^h$ hypersatellite lines (see insets of Figs. III.9 and III.10) but not for the $K\beta$ diagram line because the latter and its L-satellites lie below and above the K-absorption edge, respectively. Three and four Voigtians were needed to reproduce the M-satellite structures of the $K\alpha$ and

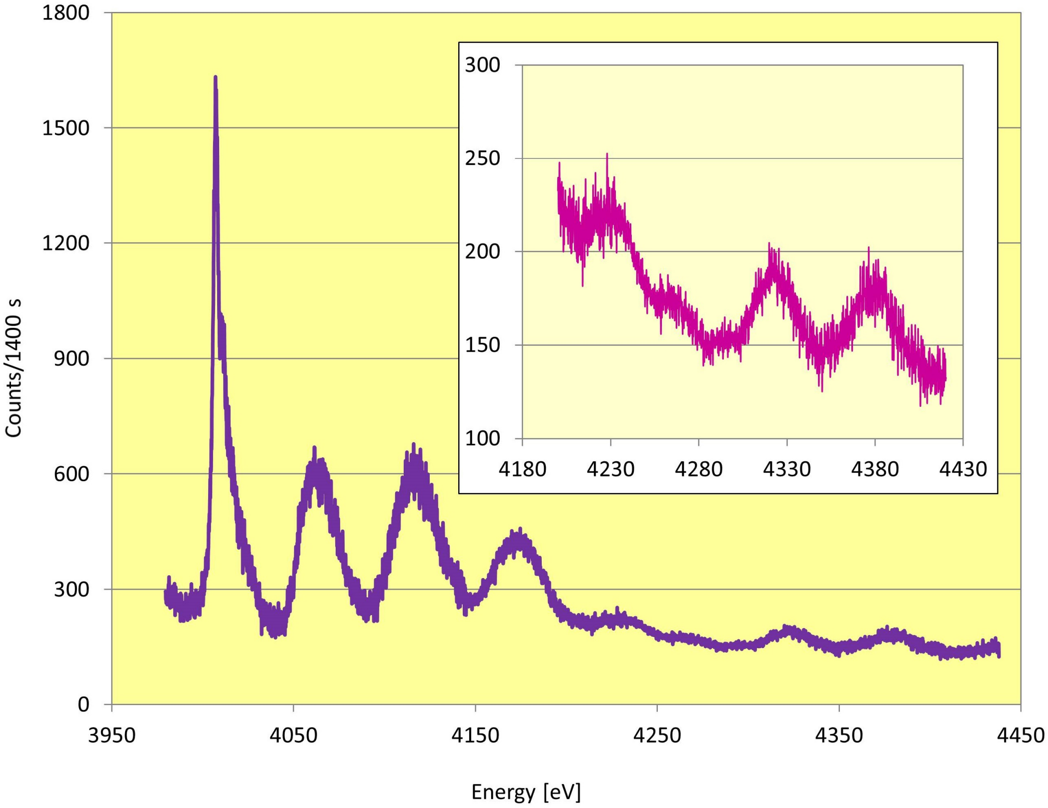

Figure III.10 – Ne-induced $K\beta$ spectrum of Ca. The hypersatellite region is shown enlarged in the inset where one can distinguish the following transitions: the 4^{th} order L-satellite of the $K\beta_{1,3}$ line at 4230 eV, the $K\beta^h_{1,3}$ hypersatellite at about 4270 eV and the 1^{st} and 2^{nd} order L-satellites of the latter at 4330 eV and 4380 eV, respectively.

$K\beta$ diagram lines, the relative intensities of the 2^{nd} and higher orders M-satellites being fixed at values corresponding to a binomial distribution. Except the 5^{th} order L-satellite which could be fitted with a single Voigtian, the L-satellites were fitted with two Voigtians, one for the L-satellite structure itself and another one for the underlying M-satellite structure.

As shown in Fig. III.11, the Kα^h_2 hypersatellite was fitted with four components, one for the hypersatellite and three for the unresolved M-satellite structure. The Kα^h L^{1-3} satellites could be well reproduced with two Voigtians per peak. For the Kα^h L^4, a single Voigtian was needed. As the 1^{st} order L-satellite of the Kα^h_2 hypersatellite is much stronger than the underlying Kα^h_1, any attempt to fit the weak hypersatellite was found to be hopeless so that the energy, natural width and relative intensity of this line had to be kept fixed in the final fit of the hypersatellite spectrum. The K$\beta^h_{1,3}$ hypersatellite was neither easy to fit because

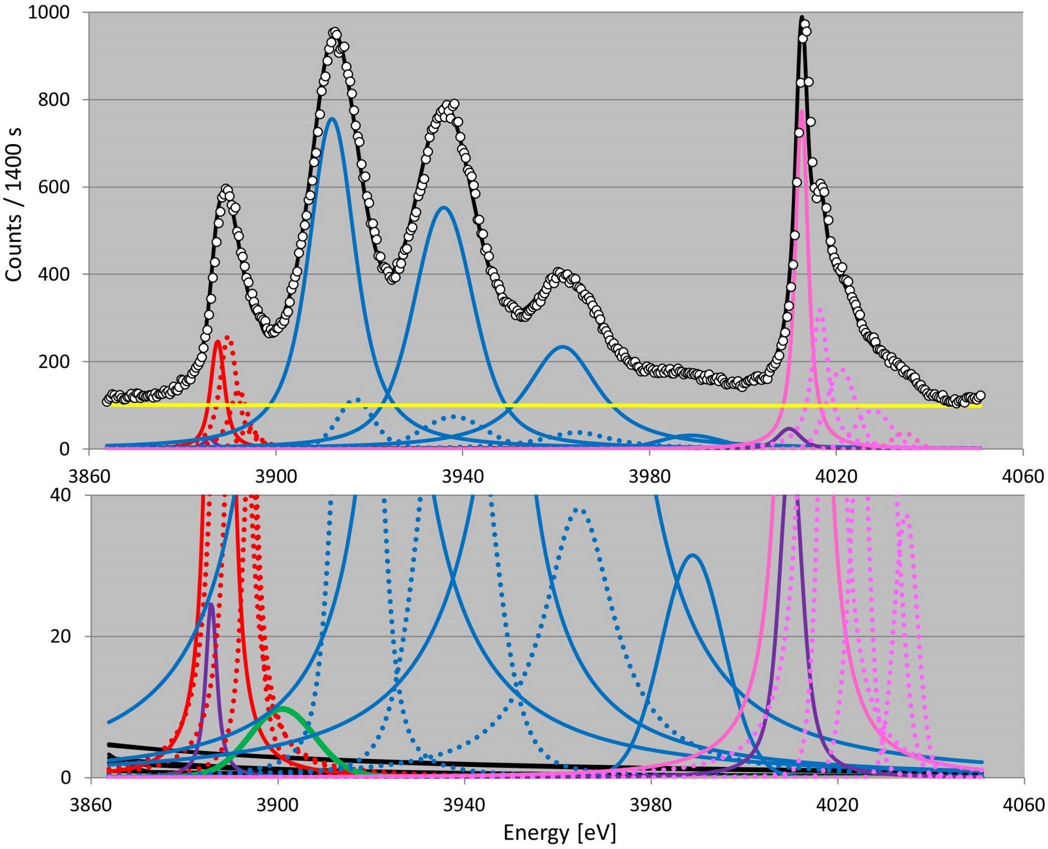

Figure III.11 – Fit of the Ne-induced $K\alpha$ hypersatellite spectrum of Ca. The top part of the Fig. shows the measured spectrum (open circles) and the total fit (black curve). A zoom view of the tails of the fitted components is presented in the lower part of the Fig. The red solid line represents the $K\alpha_2^h$ hypersatellite and the pink solid line the $K\beta$ diagram line. The blue solid lines stand for the L-satellites of the $K\alpha_2^h$ hypersatellite and the red, blue and pink dotted lines to the M-satellites accompanying the above mentioned transitions. The Voigtians in violet account for the asymmetric response of the crystal. They were found to be only needed for the fit of the $K\alpha_{1,2}$ and $K\beta_{1,3}$ diagram lines and $K\alpha_2^h$ hypersatellite. The green curve around 3900 eV (bottom panel) corresponds to the forbidden $K\alpha_1^h$ hypersatellite transition.

it is surrounded by two stronger lines, namely the $K\beta_{1,3}L^4$ satellite below it and the $K\beta^hL^1$ hypersatellite satellite above it (see the inset of III.10). The most reliable analysis was obtained by fitting this line with two juxtaposed Voigtians, the second Voigtian accounting for the asymmetry related to the unresolved M-satellites. The two L-satellites of the $\mathrm{K}\beta_{1,3}^h$ hypersatellite were fitted similarly, using two Voigtians for each component.

Other collisions

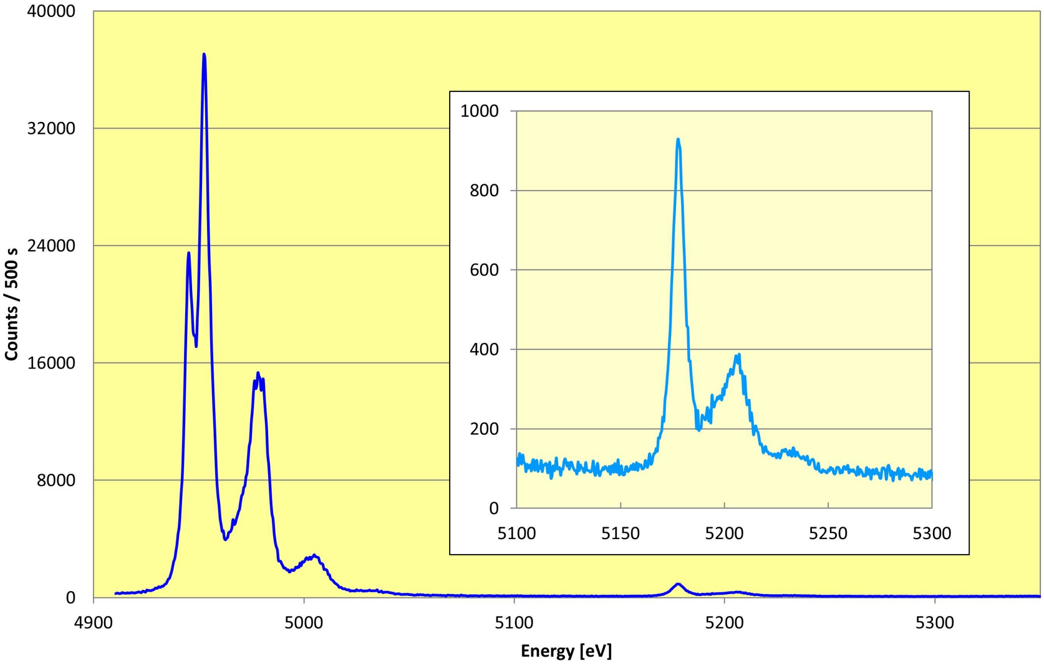

Figure III.12 – C-induced $K\alpha$ spectrum of V. The hypersatellite region is shown enlarged in the inset. The broad asymmetric peak at about 5200 eV corresponds to the $K\alpha_1^h$ hypersatellite and first order L-satellite of the $K\alpha_2^h$ hypersatellite which are overlapping and the peak at 5230 eV to the 2^{nd} order L-satellite of the $K\alpha_2^h$ hypersatellite.

The measured $K\alpha$ and $K\beta$ X-ray spectra of V induced by impact with C-ions are shown in Figs. III.12 and III.13, those induced by impact with Ne-ions in Figs III.14 and III.15. For illustration, the fits of the C-induced $K\alpha$ diagram and $K\alpha^h$ hypersatellite spectra of V are depicted in Fig. III.16 and III.17, respectively.

The C-induced and Ne-induced $K\alpha$ X-ray spectra of Fe and Cu were fitted using similar methods as the ones discussed for Ca. For illustration, the corresponding experimental spectra which were measured with the $SiO_2(2\bar{2}3)$ crystal are presented in Figs III.18-III.21. As it can be seen, the satellite and hypersatellite structures of these spectra are less intense than the ones observed in the Ca and V spectra. This is due to the fact that the multiple ionization cross section diminishes with the atomic number of the target element approximately as Z^{-4}.

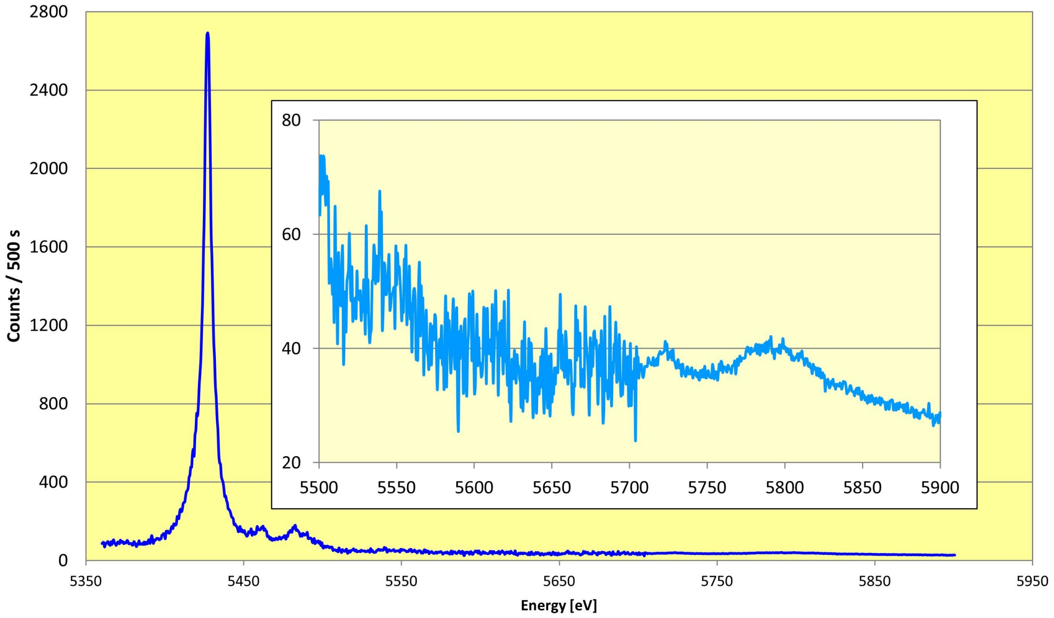

Figure III.13 – C-induced $K\beta$ diagram and hypersatellite spectrum of V. The $K\beta_{1,3}L$ satellites and $K\beta^{h}_{1,3}$ hypersatellite which lie above the K-absorption edge are strongly attenuated by the self-absorption effect.

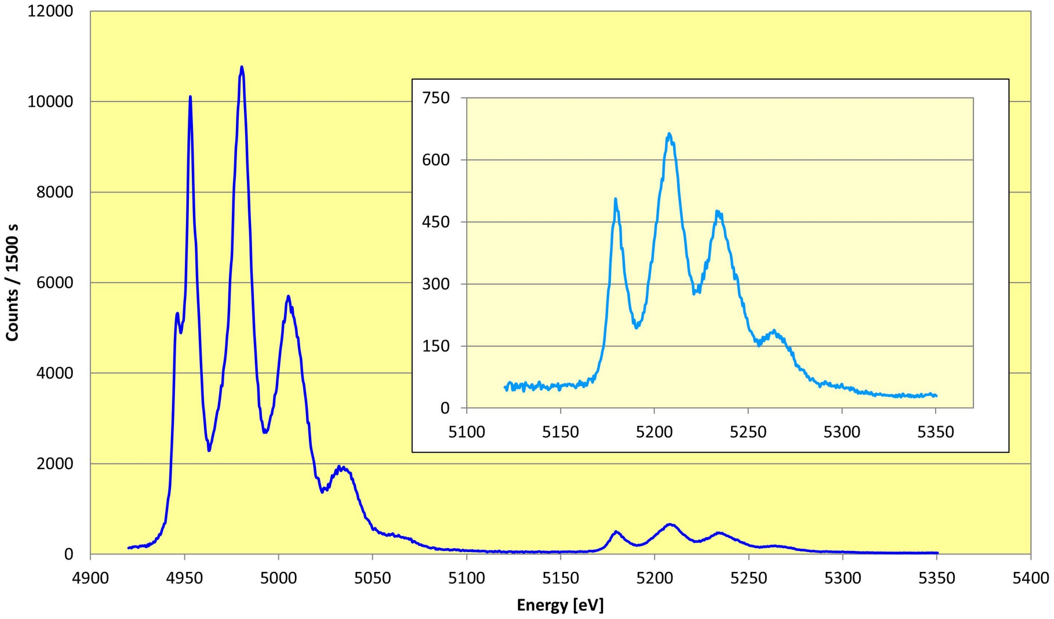

Figure III.14 – Ne-induced $K\alpha$ diagram and hypersatellite spectrum of V.

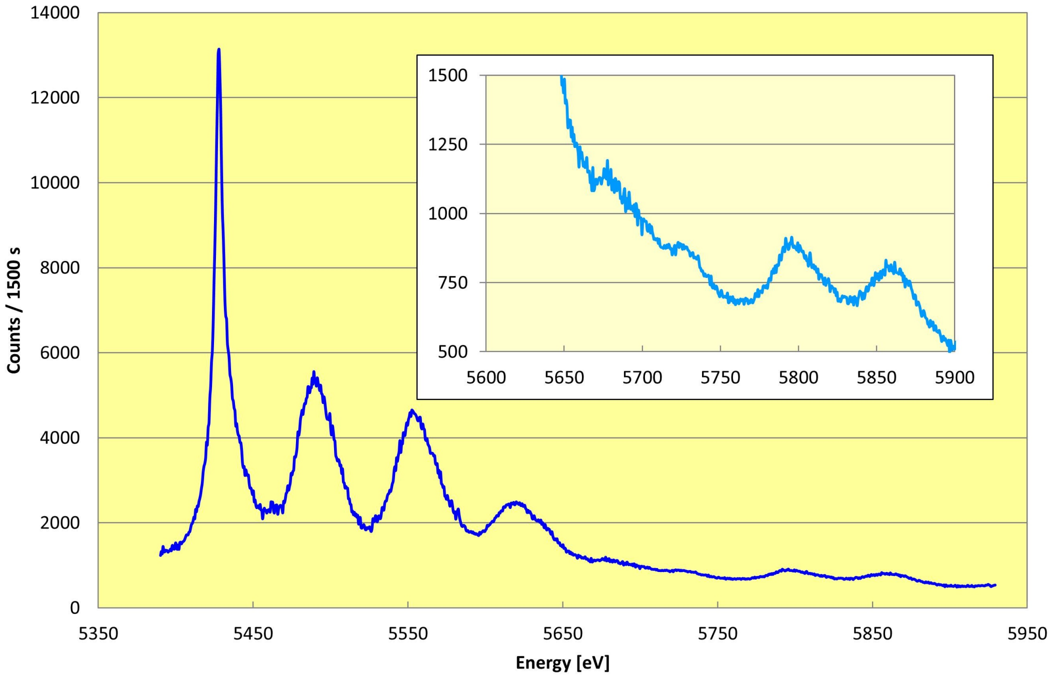

Figure III.15 – Ne-induced $K\beta$ diagram and hypersatellite spectrum of V.

III.3.4 Target self-absorption, crystal reflectivity and CCD efficiency

Target self-absorption

For target thicknesses of a few mg/cm^2 as the ones used in the present experiment, the absorption of the sample X-rays by the target itself is not negligible. This so-called self-absorption effect varies with the energy of the emitted X-rays and has thus to be considered to get reliable hypersatellite-to-diagram line intensity ratios. The correction is, however, not straightforward because the specific target activity cannot be considered as constant across the target thickness, the energy of the heavy ions decreasing with the target depth and the ionization cross section depending on the projectile energy.

The energy $E(s)$ of the projectiles at the target depth s was calculated using the formula III.3 presented in Sect. III.2.3. The ratio of the real target activity A to the activity A_0 of a hypothetical target without absorption was then determined with the following equation:

$$\frac{A}{A_0} = \frac{\int_0^{\frac{h}{\rho}} \sigma_{K,KK}[E(\frac{x}{cos\phi})] \cdot \exp[-\mu(E_X) \cdot \rho \cdot \frac{x}{sin(\vartheta+\phi)}]dx}{\int_0^{\frac{h}{\rho}} \sigma_{K,KK}[E(\frac{x}{cos\phi})]dx}, \tag{III.15}$$

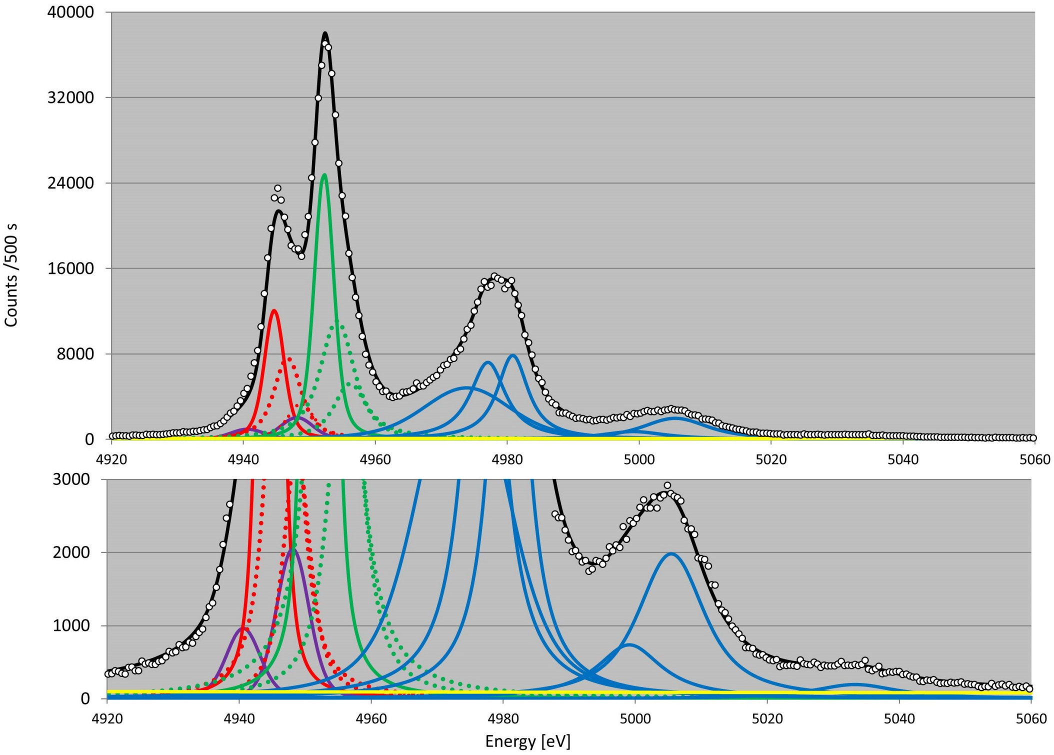

Figure III.16 – Fit of the C-induced $K\alpha$ diagram spectrum of V. The red solid and dotted lines correspond to the $K\alpha_2$ diagram transition and its unresolved M-satellites, the green solid and dotted lines to the $K\alpha_1$ diagram and M-satellites and the blue lines to the $K\alpha_{1,2}$ 1^{st} and 2^{nd} order L-satellites. The 1^{st} order L-satellite was fitted with three Voigtians, the 2^{nd} order satellite whose shape is less asymmetric could be fitted with two Voigtians. The violet lines account for the asymmetric response of the LiF crystal.

where σ_K and σ_{KK} represent the single and double K-shell ionization cross sections, μ the mass absorption coefficient in $[cm^2/g]$ for the X-ray line of energy E_X, ρ the specific weight of the target in $[g/cm^3]$ and ϑ and ϕ the Bragg angle and target alignment angle, respectively. The mass absorption coefficients were taken from the NIST database XCOM [125] and the cross sections σ_K and σ_{KK} were calculated within the SCA model using the code IONHYD of Trautmann and Rösel [124]. The obtained ratios A/A_0 are given in Table III.5 together with the corresponding self-absorption correction factors F_A. As shown, for Ca and V the self-absorption corrections are the biggest for the $K\beta^h$ hypersatellite lines because these transitions lie above the corresponding K-absorption edges where an abrupt

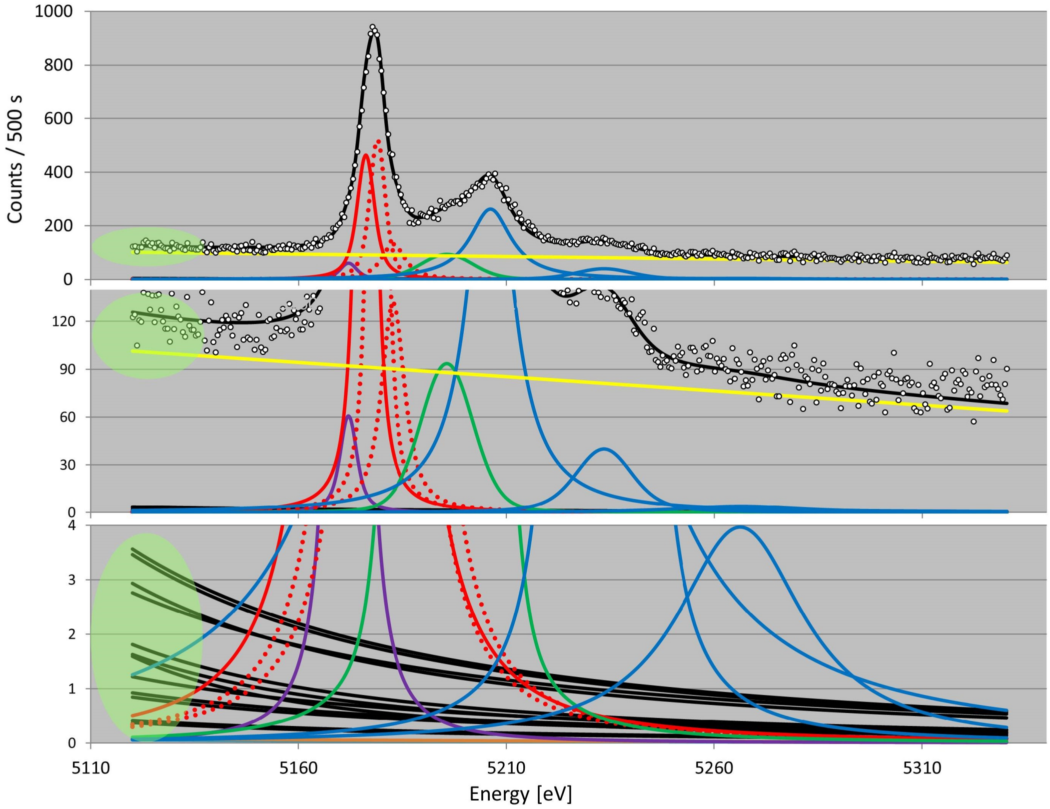

Figure III.17 – Fit of the C-induced $K\alpha^h$ hypersatellite spectrum of V. The red solid and dotted lines stand for the $K\alpha_2^h$ hypersatellite and its unresolved M-satellite structure which was reproduced with two Voigtians, the blue solid lines represent the $K\alpha_2^h$ 1^{st} and 2^{nd} order L-satellites and the blue solid line stands for the $K\alpha_1^h$ hypersatellite and close lying M satellites. As this complex line is already overlapping with the $K\alpha_2^h L^1$ line, the $K\alpha_1^h$ M-satellites could not be fitted separately. The violet line on the low energy side of the $K\alpha_1^h$ hypersatellite was inserted in the fit to take into account the asymmetric response of the LiF crystal.

and big increase of the mass attenuation coefficient μ occurs. Furthermore, the corrections are somewhat larger for the collisions with C-ions than with Ne-ions, because about 5 times thinner samples were used in the Ne measurements (see Table III.1 in Sect.III.2.2).

Crystal peak reflectivity

The peak reflectivity of the crystal varies as a function of the photon energy. As a consequence, this reflectivity variation should also be considered for a correct determination of the hypersatellite-to-diagram line yield ratios. The peak reflec-

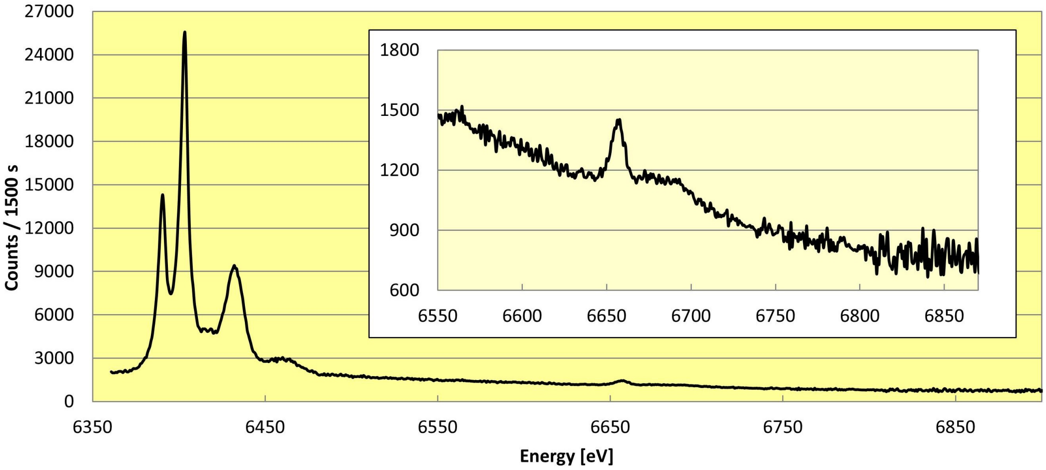

Figure III.18 – C-induced $K\alpha$ diagram and hypersatellite spectrum of Fe.

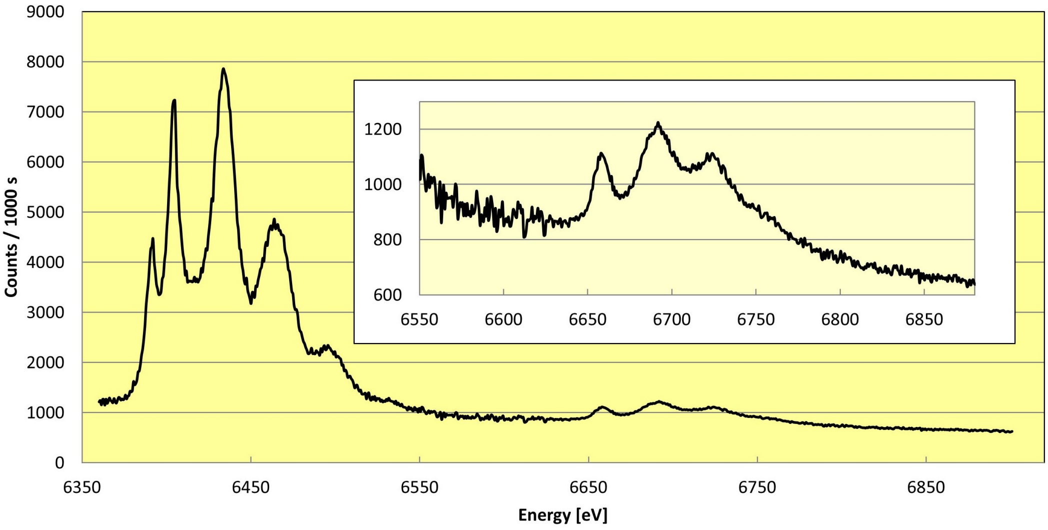

Figure III.19 – Ne-induced $K\alpha$ diagram and hypersatellite spectrum of Fe.

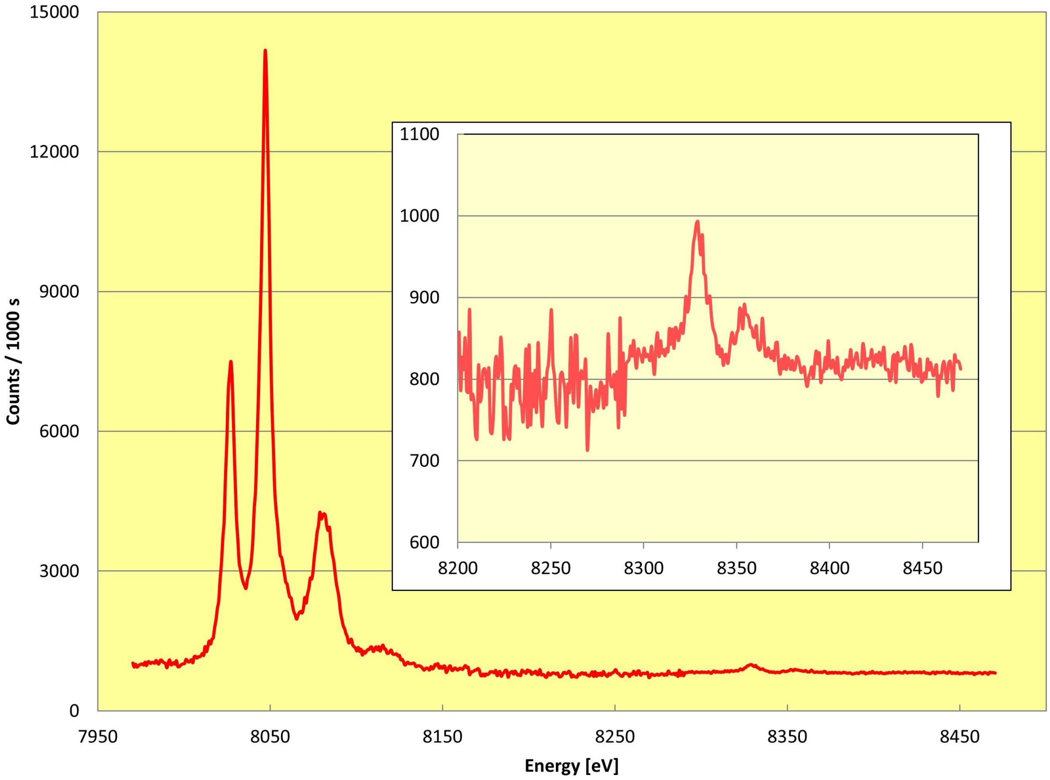

Figure III.20 – C-induced $K\alpha$ diagram and hypersatellite spectrum of Cu.

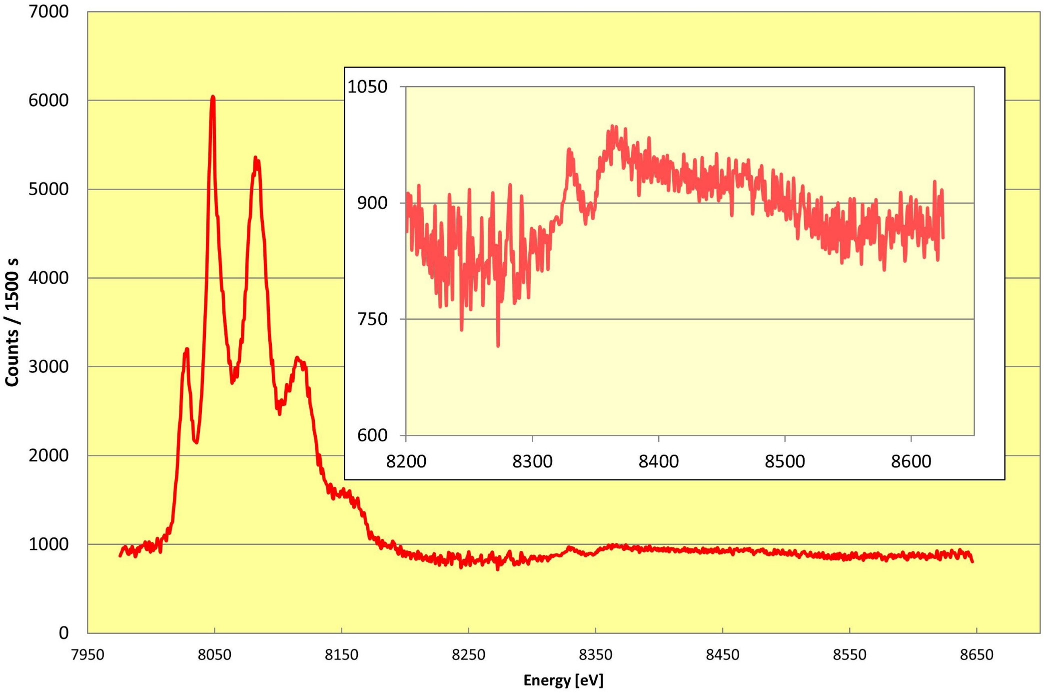

Figure III.21 – Ne-induced $K\alpha$ diagram and hypersatellite spectrum of Cu.

Table III.5 – Absorption coefficients μ, ratios A/A_0 of the target activities with and without absorption for both heavy-ion beams and corresponding self absorption correction factors F_A. For details, see text.

Target	X-ray line	μ [cm^2/g]	A/A_0 C-ions	F_A C-ions	A/A_0 Ne-ions	F_A Ne-ions
Ca	Kα	151.6	0.631	1.000	0.868	1.000
	Kα^h	131.5	0.661	0.955	0.881	0.985
	Kβ	120.8	0.680	0.928	0.889	0.976
	Kβ^h	893.0	0.156	4.045	0.459	1.891
V	Kα	95.5	0.467	1.000	0.861	1.000
	Kα^h	84.3	0.495	0.943	0.874	0.985
	Kβ	74.1	0.532	0.878	0.886	0.972
	Kβ^h	525.3	0.093	5.021	0.465	1.852
Fe	Kα	71.0	0.563	1.000	0.890	1.000
	Kα^h	63.7	0.587	0.959	0.899	0.990
Cu	Kα	51.9	0.636	1.000	0.928	1.000
	Kα^h	46.9	0.658	0.967	0.934	0.994

tivities of the two crystals were calculated for each transition of interest with the XOP software package [126]. As K X-rays are not polarized, the average value of the peak reflectivities calculated by the XOP code for photons linearly polarized in the horizontal plane (the so-called s-polarized X-rays in the XOP code) and vertical plane (p-polarized X-rays) was used to correct the fitted X-ray line intensities. The calculated average peak reflectivities R_P are reported in Table III.6 together with the corresponding correction factors F_R. Note that for p-polarized X-rays, the peak reflectivity tends to zero when the Bragg angle approaches 45 deg. This explains the abrupt diminution of the peak reflectivity of the LiF crystal for the $K\beta^h$ hypersatellite of Ca (ϑ=46.2 deg.) and the small peak reflectivities of the SiO_2 crystal for the Fe $K\alpha^h$ hypersatellite (ϑ=42.6 deg.) and especially the Fe $K\alpha$ diagram line (ϑ=44.8 deg.). In the latter case, the peak reflectivity for p-polarized X-rays is indeed negligibly small (0.08%).

CCD efficiency

The fitted X-ray line yields were further corrected to account for the variation of the CCD efficiency as a function of the photon energy. For tender X-rays ranging

Table III.6 – Peak reflectivities R_p of the LiF(200) and SiO$_2$(2$\bar{2}$3) crystals for the X-ray lines of interest and corresponding correction factors F_R as well as CCD efficiencies ϵ_{CCD} and associated correction factors F_ϵ. The total correction factors F_{tot} are also quoted. For details, see text.

Crystal	Target	X-ray line	R_p	F_R	ϵ_{CCD}	F_ϵ	F_{tot} C-ions	F_{tot} Ne-ions
LiF (200)	Ca	Kα	0.923	1.000	0.902	1.000	1.000	1.000
		Kα^h	0.892	1.036	0.909	0.992	0.981	1.012
		Kβ	0.859	1.075	0.912	0.989	0.987	1.038
		Kβ^h	0.656	1.407	0.917	0.984	5.600	2.618
	V	Kα	0.920	1.000	0.920	1.000	1.000	1.000
		Kα^h	0.944	0.974	0.917	1.003	0.921	0.962
		Kβ	0.957	0.961	0.912	1.009	0.851	0.942
		Kβ^h	0.969	0.951	0.903	1.019	4.866	1.795
SiO$_2$ (2$\bar{2}$3)	Fe	Kα	0.432	1.000	0.782	1.000	1.000	1.000
		Kα^h	0.501	0.862	0.760	1.029	0.851	0.868
	Cu	Kα	0.779	1.000	0.643	1.000	1.000	1.000
		Kα^h	0.821	0.949	0.619	1.039	0.953	0.980

between 3.5 keV and 8.5 keV which lie far above the K-absorption edge of Si, the CCD efficiency is expected to vary only smoothly with the photon energy. The CCD efficiency ϵ_{CCD} was determined using the following formula:

$$\begin{aligned}\epsilon_{CCD} = &\exp\left[-\mu_{SiO_2}(E_X)\cdot\rho_{SiO_2}\cdot\frac{h_{SiO_2}}{sin(\vartheta)}\right]\cdot\\ &\left\{1-\exp\left[-\mu_{Si}(E_X)\cdot\rho_{Si}\cdot\frac{h_{Si}}{sin(\vartheta)}\right]\right\}\quad ,\end{aligned}\tag{III.16}$$

where $\mu_{SiO_2}(E_X)$ and $\mu_{Si}(E_X)$ represent the total mass attenuation coefficients of SiO$_2$ and Si for the X-ray energy E_X, ρ_{SiO_2} and ρ_{Si} the specific weights of SiO$_2$ and Si, h_{SiO_2} and h_{Si} the thicknesses of the thin Silicon dioxide layer and silicon chip and ϑ the Bragg angle. The first term of the equation reflects the absorption of the X-rays by the thin SiO$_2$ layer which is always present on the surface of front illuminated CCD chips. The front illuminated deep depleted CCD camera employed in the present experiment was already fully characterized in a previous project [46]. In this former work, thicknesses h_{SiO_2}=1 μm and h_{Si}=40 μm were found. The latter values were thus used in Eq.III.16, while the mass attenuation coefficients were again taken from the XCOM database [125].

The CCD efficiencies calculated with Eq.III.16 for the energies of the diagram and hypersatellite lines investigated in the present project are listed in Table III.6 together with the corresponding correction factors F_ϵ. The total correction factors F_{tot}=F_A·F_R·F_ϵ are also quoted in Table III.6

III.4 Results and discussion

III.4.1 Energies

Table III.7 – Energies of the diagram and hypersatellite lines deduced from the fits. Present values are compared to existing experimental and theoretical values. The experimental values from other sources were obtained by irradiating the targets with synchrotron radiation (SR), Bremsstrahlung from X-ray tubes (BS), heavy-ions (HI) and electrons (e^-). Values are given in [eV]. The uncertainties indicated in the brackets correspond to the total errors, i.e, to the errors from the fits and the energy calibration. As in Refs. [17, 128–130] energy shifts instead of absolute energies are reported, the corresponding transition energies were determined by adding the quoted shifts to the experimental energies of the parent diagram lines taken from Ref. [30].

Target	X-ray line	Present C-beam	Present Ne-beam	Experimental data from other sources	Theoretical data from other sources
Ca	Kα_2	3688.13(7)	3688.19(7)	3688.128(49) [30]	3687.56(43) [30]
	Kα_1	3691.72(7)	3691.59(7)	3691.719(49) [30]	3690.98(41) [30]
	K$\beta_{1,3}$	4012.76(5)	4012.83(5)	4012.76(38) [30]	4014.56(43) [30]
	Kα_2^h	3887.68(7)	3887.90(8)	3887.50(9)^1 [24]	3889.5 [105]
				3883.5(6)^1 [105]	3884.8 [131]
				3840.0(1)^2 [132]	3885.9 [128]
				3890^3 [133]	3885.5 [130]
					3848.5 [117]
	Kα_1^h	3898.8(1.9)	-	3899.80(15)^1 [24]	3896.3 [131]
					3897.5 [128]
					3898.0 [130]
	K$\beta_{1,3}^h$	4268.7(1.0)	4269.8(1.5)	-	4267.7 [129]
					4267.9 [130]

---

^{1} SR; ^{2}BS; ^{3}HI; ^{4}e$^-$

Table III.7 – *(continuation)*

Target	X-ray line	Present C-beam	Present Ne-beam	Experimental data from other sources	Theoretical data from other sources
V	Kα_2	4944.98(11)	4944.84(6)	4944.671(59) [30]	4943.59(45) [30]
	Kα_1	4952.21(11)	4952.23(3)	4952.216(59) [30]	4951.79(42) [30]
	K$\beta_{1,3}$	5427.28(12)	5427.16(2)	5427.320(71) [30]	5428.14(69) [30]
	Kα_2^h	5178.12(6)	5178.5(2)	5177.65(8)^1 [24]	5175.1 [107]
				5176.6(1)^1 [107]	5176.9 [102]
				5178.1(5)^1 [105]	5179.4 [105]
				5178(2)^2 [102]	5178.1 [134]
				5180(2)^2 [134]	5176.2 [128]
	Kα_1^h	5193.5(3)	-	5192.0(9)^1 [24]	5192.2 [102]
				5191.7(1)^1 [107]	5190.9 [128]
	K$\beta_{1,3}^h$	5723.1(6)	5724.4(1.7)	-	5722.7 [129]
Fe	Kα_2	6390.35(10)	6391.13(11)	6391.026(10) [30]	6389.51(46) [30]
	Kα_1	6403.13(10)	6403.97(10)	6404.006(10) [30]	6403.13(43) [30]
	Kα_2^h	6657.52(14)	6658.20(11)	6659.70(11)^1 [107]	6655.7 [107]
				6658(2)^2 [102]	6658.2 [102]
				6655(2)^4 [135]	6657.0 [131]
				6653(2)^2 [134]	6660 [134]
				6660^2 [132]	6658 [130]
				6659(2)^2 [136]	
	Kα_1^h	6675.7(9)	-	6678.8(2)^1 [107]	6678.0 [102]
				6675(2)^4 [135]	6676.0 [128]
				6672(2)^4 [17]	6675.9 [131]
				6679(3)^2 [136]	6676 [130]

---

^{1} SR; ^{2}BS; ^{3}HI; ^{4}e$^-$

Table III.7 – *(continuation)*

Target	X-ray line	Present C-beam	Present Ne-beam	Experimental data from other sources	Theoretical data from other sources
Cu	Kα_2	8027.66(6)	8026.99(10)	8027.842(3) [30]	8028.38(48) [30]
	Kα_1	8048.01(5)	8047.90(12)	8047.823 (3) [30]	8048.11(45) [30]
	Kα_2^h	8329.9(2)	8330.1(1.4)	8329.1(1)^1 [107] 8331(3)^4 [135]	8329.3 [107] 8329.8 [128] 8330 [130]
	Kα_1^h	8354.4(6)	8355.8(1.5)	8352.6(2)^1 [107] 8352(3)^4 [135] 8351(3)^4 [17]	8353.4 [128] 8354 [130]

---

^{1} SR; ^{2}BS; ^{3}HI; ^{4}e$^-$

The fitted energies of the diagram and hypersatellite lines observed in the present work are presented in Table III.7 where they are compared to other experimental and theoretical values found in the literature.

For the diagram lines, our results are compared to the experimental energies reported recently by Deslattes et al. [30] and to the theoretical values quoted in this reference. For the C-induced $K\alpha_2$ line of V, $K\alpha_2$ and $K\alpha_1$ lines of Fe as well as for the Ne-induced $K\alpha_2$ line of Cu, energy differences of 0.31 eV, 0.68 eV, 0.88 eV and 0.85 eV, respectively, are observed which are bigger than the quoted errors. These discrepancies are probably due to inaccurate fits of the close-lying and partly unresolved M-satellite structures. For all other diagram lines, the agreement between our values and the experimental ones quoted in [30] is fully satisfactory, the square root of the mean value of the squared deviations being about 0.10 eV for both beams, i.e., similar to the present experimental uncertainties.

As it can be seen in Table III.7, the energies of the Ne-induced hypersatellite transitions are in general somewhat bigger than those obtained with the C beam. This trend is probably due to inaccurate fits of the unresolved M-satellite structures. As these satellite structures lie on the high energy side of the hypersatellites and are more pronounced in the case of the Ne-beam, some shifts towards bigger energies of the hypersatellite centroids can be indeed expected if the Voigtians used to reproduce the complex M-satellite structures does not reflect exactly the shapes of the latter. However, it is hard to draw a definitive conclusion from this trend because most of the observed energy differences are consistent with zero within the calculated uncertainties.

Four experimental values concerning the energy of the Ca $K\alpha_2^h$ hypersatellite were found in the literature. The two first values were obtained with synchrotron radiation [24, 105], the third one with an X-ray tube [132] and the fourth one with oxygen ions [133]. The first result (3887.50 eV±0.09 eV) reported by Hoszowska *et al.*, which is the most precise, is in agreement with the results obtained in the present work with both beams, whereas the value obtained by Oura *et al.* [105] is about 4.3 eV smaller. This energy difference is about 5 times bigger than the corresponding combined 1-σ error (0.8 eV). Note that the energy of (3690.4 eV±0.4 eV) quoted in [105] for the $K\alpha_{1,2}$ doublet which could not be resolved is fully consistent with the weighted average (3690.5 eV±0.1 eV) of the present $K\alpha_1$ and $K\alpha_2$ energies. Thus, the origin of the discrepancy cannot be explained by an offset between the energy calibration of the two measurements. The fourth $K\alpha_2^h$ energy (3690 eV) [133] which, like ours, was determined with heavy-ions, is consistent with our result if one assumes for this measurement, for which no error is indicated, an uncertainty of about 2 eV. In contrast to that, the $K\alpha_2^h$ energy (3840.0 eV±0.1 eV) resulting from the X-ray tube measurement performed by Verma [132] is obviously too small and not reliable. The same holds for the theoretical Hartree-Fock-Slater prediction (3848 eV) reported in [117]. Other theoretical $K\alpha_2^h$ energies found in the literature vary between 3885.5 eV [128] and 3889.5 eV [105], i.e., are in a quite satisfactory agreement with the average value (3887.79 eV±0.06 eV) obtained in the present work. For the $K\alpha_1^h$ a single other experimental value was found (3899.80 eV ± 0.15 eV) [24] which is also in agreement with our result. For the $K\beta_{1,3}^h$ hypersatellite energies, only theoretical values were found. Our experimental energies are bigger by 1-2 eV than the latter but consistent with them within the calculated uncertainties.

For V, the average value of the $K\alpha_2^h$ energy obtained in the present work with the C and Ne beams is 5178.3(1) eV, a result which is well in line with the energies of 5178.1(7) eV and 5177.4 eV corresponding to the average values of the experimental and theoretical energies reported in [24], [102], [105], [134] and [127]. Our result, however, is 1.7 eV bigger than the value of (5176.1±0.1) eV obtained by Diamant *et al.* [107] with synchrotron radiation. For the $K\alpha_1^h$ hypersatellite, which could be observed only with the C-beam, our result is bigger by about 1.5 eV than those obtained with synchrotron radiation [24, 107] but nearly consistent with them within the combined errors.

For Fe, the mean value of the experimental $K\alpha_2^h$ energies found in the literature [102, 107, 128, 134, 136] is 6657.5 eV with a standard deviation σ of 2.6 eV. This value is consistent with the average energy of 6657.9(1) eV obtained in the present work. The agreement is even better with the average value of the theoretical predictions from [102, 107, 131, 133, 134] which amounts to 6657.8 eV (σ=1.4 eV). In our experiment, the $K\alpha_1^h$ hypersatellite could be observed only with the C beam. An energy of 6675.7(9) eV was obtained from the fit. This result is also consistent with the mean values of the experimental [17, 107, 135, 136] and theoretical [102, 127, 131, 133] energies from other groups which amount to 6676.2 eV (σ=2.9 eV) and 6676.3 eV (σ=1.1 eV), respectively.

For Cu, the average $K\alpha_2^h$ energy found in our work is 8330.0(8) eV. This result is consistent with the value of 8329.1(1) obtained by Diamant *et al.* [107] with synchrotron radiation and with the one (8331 eV±3 eV) determined by Salem [135] by electron bombardment. A fair agreement is also observed with the theoretical predictions from [107] (8329.8 eV) and [131] (8330 eV). For the weaker $K\alpha_1^h$ hypersatellite, we have found an average value of 8355.1(8) eV which is nearly consistent with the experimental values of 8352(3) eV and 8351(3) eV reported in [135] and [17], respectively. Our value, however, is consistent with the one reported by Diamant *et al.* [107] (8352.6 eV±0.2 eV) only within a 3-σ error interval.

Although absolute energies are very useful for X-ray spectroscopy, relative energies or energy shifts are more adequate for comparison with theory because they permit to cope with the difficulties related to the origin of the energy scale. The energy shifts Δ_{α_1}, Δ_{α_2} and $\Delta_{\beta_{1,3}}$ of the $K\alpha_1^h$, $K\alpha_2^h$ and $K\beta_{1,3}^h$ hypersatellites with respect to their parent diagram lines are presented in Table III.8 where our results are compared to the experimental values obtained by Hoszowska *et al.* [24] for Ca and V and Diamant *et al.* [107] for Fe and Cu. Theoretical energy shifts from Costa *et al.* are also listed for the $K\alpha_{1,2}^h$ [128] and $K\beta_{1,3}^h$ [129] hypersatellites. The average of the absolute values of the deviations between our shifts and the experimental ones from [24, 107] and the theoretical ones from [128, 129] are 1.4 eV and 1.6 eV, respectively. The first deviation is 2.5 times bigger than the average value (0.6 eV) of the combined errors, indicating that the uncertainties of our results, or the ones quoted in [24, 107], might be somewhat underestimated.

We have found that the energy shifts $\Delta_{\alpha,\beta}$(Z) of the hypersatellites could be well reproduced by the following simple empirical formula:

Table III.8 – Energy shifts Δ_{α_2}=E(Kα_2^h)-E(Kα_2), Δ_{α_1}=E(Kα_1^h)-E(Kα_1) and $\Delta_{\beta_{1,3}}$=E(K$\beta_{1,3}^h$)-E(K$\beta_{1,3}$) obtained in the present work. Experimental values from other sources as well as theoretical predictions are also quoted for comparison. Values obtained from the formulas III.17 and III.24 are presented in the two last columns. All energy shifts are quoted in eV.

Target		Present	Other exp.	Theory	Eq. III.17	Eq. III.24
Ca	Δ_{α_2}	199.6(4)	199.4(1) [24]	197.8 [128]	199.3	204.9
	Δ_{α_1}	207.1(1.9)	208.1(2) [24]	205.8 [128]	203.8	209.4
	$\Delta_{\beta_{1,3}}$	256.5(9)	-	254.2 [129]	252.3	255.6
V	Δ_{α_2}	233.4(1)	233.0(1) [24]	231.6 [128]	233.3	235.0
	Δ_{α_1}	241.3(3)	239.8(1) [24]	238.6 [128]	238.8	240.7
	$\Delta_{\beta_{1,3}}$	296.5(9)	-	295.4 [129]	299.9	293.7
Fe	Δ_{α_2}	267.1(1)	268.7(1) [107]	266.3 [128]	267.7	267.4
	Δ_{α_1}	272.6(9)	274.8(2) [107]	272.0 [128]	274.3	273.6
Cu	Δ_{α_2}	302.7(7)	301.3(1) [107]	301.9 [128]	302.4	295.5
	Δ_{α_1}	307.1(8)	304.8(2) [107]	305.6 [128]	310.1	304.3

$$\Delta_{\alpha,\beta}(Z) = \frac{E_{\alpha,\beta}(Z)}{Z^{\gamma_{\alpha,\beta}}} \quad , \tag{III.17}$$

where $E_{\alpha,\beta}(Z)$ represents the energy of the parent diagram line, Z the atomic number of the considered element and $\gamma_{\alpha,\beta}$ a scaling factor which was determined by a least squares fit to our measured energy shifts, i.e., by solving the following equation:

$$\frac{d}{d\gamma_{\alpha,\beta}} \sum_Z \left[\frac{E_{\alpha,\beta}(Z)}{Z^{\gamma_{\alpha,\beta}}} - \Delta_{\alpha,\beta}(Z) \right]^2 = 0 \ . \tag{III.18}$$

After calculating the derivative, Eq. III.18 can be written as:

$$\sum_Z \frac{ln(Z) \cdot E_{\alpha,\beta}(Z) \cdot \Delta_{\alpha,\beta}(Z)}{Z^{\gamma_{\alpha,\beta}}} - \sum_Z \frac{ln(Z) \cdot E^2_{\alpha,\beta}(Z)}{Z^{2 \cdot \gamma_{\alpha,\beta}}} = 0 \ . \tag{III.19}$$

Solving numerically Eq. III.19, the following γ-values were obtained: $\gamma_{\alpha_2} = 0.974$, $\gamma_{\alpha_1} = 0.967$ and $\gamma_{\beta_{1,3}} = 0.924$. The different energy shifts were then calculated using the corresponding γ-values in Eq. III.17. The results are listed in the 6^{th} column of Table III.8. As shown, this empirical scaling law reproduces the measured energy shifts quite satisfactorily, the average of the absolute values of the deviations being 1.9 eV. It was further found that this very simple formula can reproduce with a precision of a few eV the hypersatellite energy shifts of elements even if the atomic numbers of the latter are significantly smaller or bigger than the ones ($20 \leq \mathrm{Z} \leq 29$) employed in the computation of the scaling factors γ. For instance, for the $K\alpha_2^h$ hypersatellites of Al (Z=13) and Kr (Z=36), shifts of 121.8 eV and 382.2 eV are obtained from Eq. III.17, whereas the corresponding theoretical values found in [128] amount to 124.3 eV and 387.0 eV, respectively.

The hypersatellite energy shifts were also estimated with a more scientifically sound method based on the definition of the energy of an X-ray transition. The energy of the $K\alpha$ transition is given by:

$$E(K\alpha) = E_{1s^{-1}} - E_{2p^{-1}} \ , \tag{III.20}$$

where $E_{1s^{-1}}$ and $E_{2p^{-1}}$ represent the total energies of the considered ionized atom with one hole in the K-shell, respectively in the L_2- or L_3-subshell. If the total energy of the neutral atom is chosen as the origin of the energy scale, the energies $E_{1s^{-1}}$ and $E_{2p^{-1}}$ are both positive and $E_{1s^{-1}} \geq E_{2p^{-1}}$. From these definitions, it can be easily shown that $E_{1s^{-1}}$ and $E_{2p^{-1}}$ coincide with the absolute values of the binding energies of the 1s and 2p electrons.

The energy of the $K\alpha^h$ hypersatellite transition reads analogously:

$$E(K\alpha^h) = E_{1s^{-2}} - E_{1s^{-1}2p^{-1}} \ . \tag{III.21}$$

The energy of the initial state $E_{1s^{-2}}$ can be approximated by:

$$E_{1s^{-2}}(Z) = 2 \cdot E_{1s^{-1}}(Z) + \epsilon_K \cdot \Big[E_{1s^{-1}}(Z{+}1) - E_{1s^{-1}}(Z)\Big] \ , \tag{III.22}$$

where ϵ_K is a constant comprised between 0 and 1 which accounts for the screening diminution resulting from the removal of the second K-shell electron. For 3d transition elements, this constant was found to be 0.570 [107]. The energy of the final state $E_{1s^{-1}2p^{-1}}$ can be written in a similar way:

$$E_{1s^{-1}2p^{-1}} = E_{1s^{-1}} + E_{2p^{-1}} + \epsilon_L \cdot \Big[E_{2p^{-1}}(Z{+}1) - E_{2p^{-1}}(Z)\Big] \ . \tag{III.23}$$

The energy shift Δ_α of the $K\alpha^h$ hypersatellite is obtained by subtracting Eq. III.20 from Eq. III.21. Inserting the relations III.22 and III.23 in the calculations, one finds:

$$\begin{aligned}\Delta_\alpha(Z) = \epsilon_K \cdot \Big[E_{1s^{-1}}(Z{+}1) - E_{1s^{-1}}(Z)\Big] - \\ \epsilon_L \cdot \Big[E_{2p^{-1}}(Z{+}1) - E_{2p^{-1}}(Z)\Big] \ .\end{aligned} \tag{III.24}$$

The coefficients $\epsilon_{L_{2,3}}$ which are not known were determined from our experimental shifts by means of a least squares fit method, using the following equation:

$$\begin{aligned}\frac{d}{d\epsilon_{L_{2,3}}} \sum_Z \Big\{ \Delta_{\alpha_{2,1}}(Z) - \epsilon_K \cdot \Big[E_{1s^{-1}}(Z{+}1) - E_{1s^{-1}}(Z)\Big] + \\ \epsilon_{L_{2,3}} \cdot \Big[E_{2p^{-1}_{1/2,3/2}}(Z{+}1) - E_{2p^{-1}_{1/2,3/2}}(Z)\Big]\Big\}^2 = 0 \ .\end{aligned} \tag{III.25}$$

The solutions of the above equation can be determined analytically. After some simple algebra one gets:

$$\epsilon_{L_{2,3}} = \frac{\sum\limits_Z \epsilon_K \cdot \Big[E_{1s^{-1}}(Z+1) - E_{1s^{-1}}(Z)\Big] - \sum\limits_Z \Delta_{\alpha_{2,1}}(Z)}{\sum\limits_Z \Big[E_{2p^{-1}_{1/2,3/2}}(Z{+}1) - E_{2p^{-1}_{1/2,3/2}}(Z)\Big]} \ . \tag{III.26}$$

Using the value of 0.570 reported in [107] for ϵ_K and the electron binding energies quoted in [137] for the $1s_{1/2}$, $2p_{1/2}$ and $2p_{3/2}$ atomic levels, one obtains from Eq. III.26 $\epsilon_{L_2} = 0.995$ and $\epsilon_{L_3} = 0.935$. Inserting these values in Eq. III.24, one can determine finally the energy shifts of the $K\alpha^h_{1,2}$ hypersatellites. The latter are quoted in the last column of Table III.8. Here again a quite satisfactory agreement is observed, the square root of the mean squared deviations relative to our experimental shifts being 2.6 eV.

The same method was employed for the calculation of the energy shifts of the $K\beta^h$ hypersatellites. The single change consisted in replacing $\epsilon_{L_{2,3}}$ by $\epsilon_{M_{2,3}}$ in Eq. III.26. As the differences of the $3p$ electron binding energies between the investigated elements (atomic number Z) and their next neighbours (atomic number Z+1) are only a few eV, i.e., are similar in size to the errors of the measured energy shifts, the least squares fit method was found to provide inaccurate results and was therefore not employed. However, as values close to one were found for the coefficients $\epsilon_{L_{2,3}}$, a value of one was assumed in Eq. III.24 for $\epsilon_{M_{2,3}}$. As it can be seen in Table III.8, this assumption looks reasonable since the observed deviations between the so-obtained $K\beta^h$ energy shifts and our experimental values are only -0.9 eV for Ca and -2.8 eV for V.

III.4.2 Widths

The Lorentzian widths of the weak $K\alpha_1^h$ hypersatellites had to be kept fixed in the data analysis to get reliable fits. The $K\alpha_1^h$ widths were fixed at the same values as the ones of the stronger $K\alpha_2^h$ hypersatellites. This is justified because the differences between the widths of the L_2 and L_3 atomic levels are small [33] with respect to the total widths of the hypersatellites. On the other hand, for $3d$ transition elements, it is well known that the $K\beta_{1,3}$ X-ray lines evince strong asymmetries on their low energy sides. Such asymmetries being due to non-lifetime effects, the full widths at half maximum of these transitions can no longer be interpreted as natural line widths. Similar asymmetries are also expected for the $K\beta_{1,3}^h$ hypersatellites even if the asymmetries in this case are somewhat smeared out by the bigger line widths of the hypersatellites as compared to those of the parent diagram lines. For these reasons, only the natural line widths of the $K\alpha_2^h$ hypersatellites are discussed hereafter.

As a consequence of the Heisenberg uncertainty principle, the energy of an atomic level is not infinitely precise but is described by a Lorentzian function whose full width at half maximum corresponds to the so-called natural width of the level. As the energy of an X-ray transition is given by the difference of the energies of the two atomic levels involved in this transition and because the convolution of two Lorentzian functions is still a Lorentzian whose width is given by the sum of the widths of the two convolved functions, the natural width of an X-ray transition is obtained by summing the widths of the initial and final states. Assuming furthermore that the mean lifetime of a double K-shell vacancy state is two times shorter than the one of the singly-ionized K-shell state [138], i.e., that $\Gamma_{KK} \cong 2\Gamma_K$, the natural width of the $K\alpha_2^h$ hypersatellite transition reads:

$$\Gamma(K\alpha_2^h) \cong 3 \cdot \Gamma_K + \Gamma_{L_2} \quad , \tag{III.27}$$

where Γ_K and Γ_{L2} stand for the widths of the K and L_2 atomic levels.

Table III.9 – Natural line widths in [eV] of the $K\alpha_2^h$ hypersatellites obtained in the present work by averaging the Lorentzian widths provided by the fits for the two beams. Other available experimental (Exp.) and theoretical (Theo.) values are also quoted for comparison as well as the widths derived from Eqs. III.27 and III.28.

Target	Present	Exp. [24]	Exp. [107]	Theo. [19]	Eq. III.27	Eq. III.28
Ca	4.4(2)	3.72(18)	-	3.63	2.52	3.82
V	5.9(2)	5.54(19)	5.5(1)	5.46	3.66	5.23
Fe	7.3(4)	-	6.1(2)	6.46[a]	4.71	6.31
Cu	7.4(8)	-	6.9(8)	7.09[b]	5.51	6.89

---

[a] determined by a linear interpolation of the values quoted for Cr (Z=24) and Co (Z=27)

[b] determined by a linear interpolation of the values quoted for Co (Z=27) and Zn (Z=30)

The Lorentzian widths of the $K\alpha_2^h$ hypersatellites obtained in the present experiment are presented in Table III.9 together with other existing experimental and theoretical values. Predictions based on the approximation III.27, in which the values recommended by Campbell and Papp [33] for the widths of the K and L_2 levels were employed, are also quoted. Present widths correspond to the mean values of the Lorentzian widths obtained with the C and Ne beams. In average, the differences between the widths obtained for the two beams were found to be nearly equal to the combined errors, i.e., to the errors quoted in the second column of Table III.9. The experimental values reported in the third and fourth columns were determined using synchrotron radiation. One can note that for V, the single common element investigated in [24] and [107], the two results are fully consistent. The theoretical predictions listed in the fifth column were taken from [19]. In these calculations which are in general in good agreement with the experimental values from [24, 107], the influences of the open-shell valence configuration (OVC) and the outer-shell ionization (OIE2) following the double photoionization process were taken into consideration.

All measurements of hypersatellite widths performed so far have led to the conclusion that the approximation III.27 underestimates significantly the real widths of hypersatellites. Table III.9 shows that this is also the case in the present experiment. However, if the ratio of the real widths to the widths obtained from Eq. III.27 is plotted as a function of the atomic number Z, ones finds that the ratio diminishes almost linearly with Z. One can thus re-scale Eq. III.27 in the following way:

$$\Big[\Gamma(K\alpha_2^h)\Big]_{cor} = (3\cdot\Gamma_K + \Gamma_{L_2})\cdot(a\cdot Z + b)\ . \tag{III.28}$$

Fitting the above formula to the experimental widths from [24] and [107], values a = -0.03 and b = 2.11 are found for the coefficients of the linear regression line. Inserting these results in Eq. III.28, one obtains the widths reported in the last column of Table III.9. As shown, the new values are well in line with the experimental and theoretical widths reported in [24, 107] and [19], respectively.

From Table III.9 it can be further seen that, except for Fe, present $K\alpha_2^h$ widths are consistent or nearly consistent with other experimental and theoretical values. However, present results are all bigger than the ones obtained with synchrotron radiation, indicating that the single Voigtian functions employed in our fits to reproduce the unresolved M-satellite structures do not completely account for the broadening of the hypersatellite lines induced by the additional M-shell spectator vacancies.

III.4.3 Relative intensities

Table III.10 – Relative intensities of the Kα hypersatellites in percent. Errors on the last digits are given in brackets. Values presented in columns 2 & 3 were obtained from the fitted intensities, those given in columns 4 & 5 correspond to the latter ratios corrected to account for the target self-absorption, crystal reflectivity and CCD efficiency.

Target	I(K$\alpha_{1,2}^h$)/I(K$\alpha_{1,2}$)		[I(K$\alpha_{1,2}^h$)/I(K$\alpha_{1,2}$)]$_{cor}$	
	C	Ne	C	Ne
Ca	2.77(29)	7.39(86)	2.72(46)	7.48(1.21)
V	2.05(21)	4.97(82)	1.89(33)	4.78(95)
Fe	1.94(25)	4.91(51)	1.65(31)	4.26(65)
Cu	1.49(18)	3.82(54)	1.42(25)	3.74(68)

The $K\alpha$ hypersatellite-to-parent diagram line intensity ratios deduced from the fits are presented in the second and third columns of Table III.10. As mentionned before, the intensities belonging to the unresolved M-satellites and the ones corresponding to the parent diagram or hypersatellite lines could not be unambiguously

Table III.11 – Ratios in percent of the Kα_1^h to Kα_2^h hypersatellite intensities obtained in the present work. For comparison, experimental values reported in [24] and [107] and theoretical predictions from [128] and [131] are also quoted.

Target	Present		Other exp.		Other theo.	
	C	Ne	[24]	[107]	[128]	[131]
Ca	2.8(9)	-	3.5(1.3)	-	2.7	2.9
V	7.1(1.2)	-	7.7(1.5)	8(1)	9.9	11.8[a]
Fe	14.5(2.4)	12.6(1.4)	-	16(3)	18.9	21.7
Cu	31.3(1.8)	32.6(9.1)	-	29(2)	32.5	34.9[b]

---

[a] linear interpolation between Ti (Z=22) and Cr (Z=24)
[b] linear interpolation between Fe (Z=26) and Zn (Z=30)

assigned in the fitting procedure. This resulted in slight energy shifts towards higher energies (see Table III.7) and to somewhat too big Lorentzian widths (see Table III.9) of the heavy-ion-induced diagram and hypersatellite lines. For this reason, the quoted yield ratios were determined by considering the sums of the diagram or hypersatellite line intensities and those of the corresponding unresolved M-satellites. The uncertainties quoted in the brackets of the second and third columns correspond to the combined errors from the fits and from the corrections factors applied to the measured spectra before the fitting procedure (see Sect. III.3.2), correction factors for which a total relative uncertainty of 10% was assumed.

The additional corrections accounting for the target self absorption, crystal reflectivity and CCD efficiency were applied after the fitting procedure using the correction factors F_{tot} quoted in Table III.6. The so-obtained corrected intensity ratios are listed in the right part of Table III.10. Here uncertainties of 5% and 10% were assumed for the CCD efficiency and crystal peak reflectivity corrections, respectively. For the self absorption correction, an accuracy of 10% was estimated for the XCOM mass attenuation coefficients [125], which resulted in relative uncertainties varying from 1.0% (Ne-Cu collision) up to 9.1% (C-V collision) for the self-absorption correction factors F_A.

Relative uncertainties close to 100% or even bigger were found for the corrected $K\beta_{1,3}^h/K\beta_{1,3}$ yield ratios of Ca and V. This is due to the fact that the errors on the fitted $K\beta_{1,3}^h$ intensities, which are already large due to the poor intensities of these transitions, become even bigger when multiplied by the corresponding self-absorption correction factors F_A. As the $K\beta_{1,3}^h$ hypersatellites lie above the K absorption edges, the corresponding correction factors F_A are indeed huge, in particular for the measurements performed with the C beam for which thicker targets were employed. For this reason, the $K\beta$ hypersatellite-to-parent diagram line yield ratios were not included in Table III.10, the obtained values being not enough reliable for a relevant comparison with the corresponding $K\alpha^h/K\alpha$ yield ratios.

For the collisions for which the $K\alpha_1^h$ intensity could be let free in the fitting procedure, the $K\alpha_1^h$ to $K\alpha_2^h$ yield ratios were also determined. The results are presented in Table III.11 together with other existing experimental and theoretical values. As shown a nice agreement is observed in most cases.

III.4.4 Ratios of double-to-single ionization cross sections

The intensity I_X of an X-ray transition measured with the von Hamos spectrometer reads:

$$I_X = I_b \cdot n \cdot h \cdot \sigma \cdot \omega \cdot \frac{A}{A_0} \cdot \Omega \cdot R_p \cdot \epsilon_{CCD} \quad , \tag{III.29}$$

where I_b represents the beam intensity, n the number of target atoms per unit volume, h the target thickness, σ the ionization cross section, ω the fluorescence yield, A/A_0 a correction factor which accounts for the target self-absorption effect, Ω the solid angle of the spectrometer which includes the effective target size, R_p the crystal peak reflectivity and ϵ_{CCD} the CCD efficiency. As the spectra were normalized by the beam intensity, for a given target the $K\alpha$ hypersatellite-to-diagram line yield ratio is given by:

$$\frac{I(K\alpha^h)}{I(K\alpha)} = \frac{\sigma_{KK}}{\sigma_K} \cdot \frac{\omega_{KK}}{\omega_K} \cdot F_A^{-1} \cdot F_{\Omega,S_{eff}}^{-1} \cdot F_R^{-1} \cdot F_\epsilon^{-1} \quad , \tag{III.30}$$

where ω_K and ω_{KK} represent the fluorescence yields of the singly- and doubly-ionized K-shell of the target atoms, and F_A, $F_{\Omega,S_{eff}}$, F_R and F_ϵ are the correction factors discussed in Sect. III.3.2 and Sect. III.3.4.

From the above equation, the ratio of the double-to-single K-shell ionization cross sections can be written as:

$$\frac{\sigma_{KK}}{\sigma_K} = \frac{I(K\alpha^h)}{I(K\alpha)} \cdot F_A \cdot F_{\Omega,S_{eff}} \cdot F_R \cdot F_\epsilon \cdot \frac{\omega_K}{\omega_{KK}} = \left[\frac{I(K\alpha^h)}{I(K\alpha)}\right]_{cor} \cdot \frac{\omega_K}{\omega_{KK}} \ . \tag{III.31}$$

Inserting in Eq. III.31 the corrected intensity ratios $[I(K\alpha^h)/I(K\alpha)]_{cor}$ listed in Table III.10 and the ratios ω_K/ω_{KK} (see Table III.12) determined from the singly- and doubly-ionized K-shell fluorescence yields reported in Refs. [58] and [131], respectively, the double-to-single K-shell ionization cross section ratios could be determined. The results are presented in Tables III.13 (collisions with C ions) and III.14 (collisions with Ne ions). For comparison the corresponding ratios obtained from calculations performed with the Semi-Classical Approximation (SCA) and from Classical Trajectory Monte Carlo (CTMC) simulations are also quoted.

In the investigation of the K-shell ionization induced by impact with charged particles, it is usual to introduce the so-called reduced velocity η_K of the projectile which is defined by:

$$\eta_K = \frac{v_p^2}{u_K^2} \ , \tag{III.32}$$

where v_p is the projectile velocity and u_K the orbital velocity of the K-shell electron in the target atom. Using some simple algebra, the dimensionless parameter η_K can be written as:

$$\eta_K \cong 40.4 \cdot \frac{E_p^*}{(Z - S_K)^2} \ , \tag{III.33}$$

where E_p^* is the specific kinetic energy of the projectile in [MeV/amu], Z the atomic number of the target atom and S_K the Slater screening factor for the K-shell (S_K=0.3).

The rapidity ξ_K of a collision is defined as the ratio of the time needed by the projectile to traverse the K-shell of the target atom (r_K/v_p) and the characteristic time of the K-shell electron ($\hbar/E_K$) [139]. Thus, the parameter ξ_K reads:

$$\xi_K = \frac{\frac{r_K}{v_p}}{\frac{\hbar}{E_K}} = \frac{2}{\theta_K} \cdot \sqrt{\eta_K} \ , \tag{III.34}$$

where r_K is the radius of the K-shell, E_K the binding energy (absolute value) of the K-shell electron and θ_K the so-called external screening factor for the target K-shell electron. The latter parameter is given by:

$$\theta_K = \frac{E_K}{R_\infty \cdot (Z - S_K)^2} \ . \tag{III.35}$$

In the above formula E_K should be entered in eV and R_∞ represents the absolute value of the ground state energy of the Hydrogen atom, i.e., $R_\infty = 13.6$ eV.

The collision is said slow when $\xi_K \ll 1$ and fast when $\xi_K \gg 1$. When the rapidity parameter $\xi_K \cong 1$, the collisions are referred to as intermediate velocity collisions. The values θ_K, η_K and ξ_K of the collisions studied in the present work are presented in Table III.12. As shown, for all collisions the rapidity parameter is bigger than 1 but not much bigger. As a consequence, the investigated collisions can be considered as moderately fast. For such collisions, the inner-shell ionization is dominated by two processes, namely the direct Coulomb ionization (DCI), denominated also impact-induced ionization, and the electron capture (EC). The probability to remove the second 1*s* electron by a shake process produced by the sudden change of the electronic screening resulting from the first *K*-shell ionization is indeed expected to be negligibly small as compared to the probabilities of the DCI and EC processes. From calculations performed by Mukoyama and Taniguchi within the Sudden Approximation model [100], the probabilities to excite via a shakeoff or shakeup process a 1*s* electron as a result of a sudden 1*s* vacancy production is only 0.007% for Ca, 0.005% for V, 0.004% for Fe and 0.003% for Cu. The same holds for the knock-out (KO or TS1) process, i.e., the removal of the second 1*s* electron as a result of a collision with the first ionized 1*s* electron.

Table III.12 – Reduced velocities η_K and rapidities ξ_K of the investigated collisions. The external screening factors θ_K and the fluorescence yield ratios ω_K/ω_{KK} are also quoted.

Target	θ_K	ω_K/ω_{KK}	η_K		ξ_K	
			C ions	Ne ions	C ions	Ne ions
Ca	0.765	0.880	1.214	0.914	2.88	2.50
V	0.780	0.934	0.894	0.684	2.42	2.12
Fe	0.792	0.967	0.694	0.532	2.10	1.84
Cu	0.802	0.950	0.556	0.429	1.86	1.63

In the DCI process, the ionization is due to the Coulomb interaction between the charged projectile and the bound electrons of the target atom. Several bound electrons can be involved simultaneously in the interaction so that the target atom is usually left in a multiply ionized state after the collision. In the EC process, one or more bound electrons of the target atom can be captured by the bare or nearly bare projectile. Actually, as the electron capture probability varies as n_p^{-3} [140], where n_p is the principal quantum number of the projectile level into which the electron is captured, the EC into the $1s$ orbital of the projectile prevails and the EC process contribution is only sizeable in the case of fully stripped ions or H-like ions.

In our experiment the initial charges of the C and Ne ions were 4+ and 6+, respectively. However, when energetic ions travel through a medium, their charge state varies as a function of the penetration depth and, at a certain depth, a charge equilibrium which is independent from the initial charge state of the ion is attained. The average charge equilibrium Z_{eff} of an ions travelling through a medium can be approximated using the following empirical relation [141, 142]:

$$Z_{eff} = Z_p \cdot \left[1 + \left(\frac{3.86 \cdot \sqrt{E_{out}/M_p}}{Z_p^{0.45}}\right)^{-1/0.6}\right]^{-0.6} , \tag{III.36}$$

where Z_p and M_p are the atomic number and atomic mass of the projectile and E_{out} the kinetic energy of the latter at the exit of the target foil. Using in the above relation the kinetic energies of the emerging projectiles E_{out} given in Table III.2, the average equilibrium charge was found to be nearly the same for all targets, namely 5.8+ for the C ions and 9.4+ for the Ne ions. Thus, in our investigation the projectiles interacting with the target atoms were either fully stripped ions or H-like ions. As a consequence, the EC process was not negligible and the observed $K\alpha$ diagram X-ray lines originated either from a single K-shell ionization or from a single capture of a K-shell electron, while the $K\alpha^h$ hypersatellite lines arose from a double K-shell ionization or a double K-shell electron capture or from the combination of a single K-shell ionization and a single K-shell electron capture.

The SCA model introduced by Bang and Hansteen [143] is an intermediate approach between classical physics and quantum mechanics in which the projectile is treated classically and the target atom using quantum theory. The SCA model is based on the first order time-dependent perturbation theory. In the present study, the modified SCA version of Trautmann and Rösel [124] using screened hydrogen-like wave functions (HWF) for the description of the target atom electrons was employed to calculate the single and double K-shell ionization cross sections. In the calculations performed within the separated-atom (SA) picture, the recoil of the target atom was considered and the projectile was assumed to have a point-like

Table III.13 – Comparison between the double-to-single K-shell ionization cross section ratios σ_{KK}/σ_K obtained in the present work with the C ions and theoretical predictions from the SCA and CTMC models. All ratios are given in %. The SCA calculations were performed using hydrogen-like wave functions (HWF) and Dirac Hartree Fock wave functions (DHF). In the CTMC calculations the ratios were computed for the direct Coulomb ionization (DCI) only and for the DCI and electron capture (EC) contributions (DCI+EC). The theoretical cross section ratios quoted in the last column were obtained using the SCA DHF model for the impact ionization cross sections and the CTMC calculations corrected by the scaling factor α for the electron capture cross sections. The cross sections were normalized beforehand to account for the effective charge of the projectiles. For details, see the text.

Target	σ_{KK}/σ_K					
	Present	SCA HWF	SCA DHF	CTMC DCI	CTMC DCI+EC	SCA/CTMC DCI+α·EC
Ca	2.40(44)	1.47	1.78	3.27(7)	4.74(7)	2.01
V	1.77(33)	1.36	1.56	2.43(7)	4.12(7)	1.90
Fe	1.59(32)	1.19	1.35	2.06(8)	3.60(7)	1.71
Cu	1.35(26)	1.01	1.11	1.42(7)	2.70(6)	1.26

charge distribution and to move along a classical hyperbolic trajectory. The corresponding cross section ratios $(\sigma_{KK}/\sigma_K)_{SCA\ HWF}$ are quoted in the 3^{rd} columns of Tables III.13 and III.14.

In a more recent version of the SCA code, the radial hydrogenic wave functions were replaced by more realistic relativistic Hartree-Fock wave functions (DHF) for both bound and continuum states [144]. As this change resulted into a much better agreement between experiment and theory for the ionization probabilities of the L-shell [145] and especially the M-shell [146], SCA DHF calculations were also carried out for the present study. As shown in Tables III.13 and III.14, the double-to-single ionization cross section ratios $(\sigma_{KK}/\sigma_K)_{SCA\ DHF}$ are bigger than the ones obtained with the SCA HWF calculations and closer to the experimental ratios. Actually, as the uncertainties on the experimental ratios are rather large (about 18%), the theoretical SCA DHF predictions are in agreement with the experimental values except for the C-Ca collision. However, for all collisions the ratios predicted by the SCA DHF model are systematically smaller than the experimental values.

Table III.14 – Same as Table III.13 but for the collisions with the Ne ions.

Target	σ_{KK}/σ_K					
	Present	SCA HWF	SCA DHF	CTMC DCI	CTMC DCI+EC	SCA/CTMC DCI+α·EC
Ca	6.58(1.16)	4.99	5.79	5.41(8)	10.63(7)	6.34
V	4.96(94)	4.31	4.91	4.10(8)	8.84(6)	5.46
Fe	4.12(69)	3.57	3.95	2.86(8)	6.55(6)	4.41
Cu	3.55(69)	2.88	3.09	1.93(12)	4.88(8)	3.46

As the above mentioned deviations might be due to the fact that the EC process is not considered in the SCA model, the cross section ratios were also calculated using classical trajectory Monte Carlo (CTMC) simulations [147, 148] from which both the impact-induced ionization and electron capture cross sections can be obtained. For each collision, 500'000 particle trajectories were simulated. The calculations were performed within the frozen atom picture. The charge of the atomic nucleus was calculated using the Slater recipe but the interaction between the two K-shell electrons was neglected. The collision trajectories were calculated for all processes creating a singly- or doubly-ionized $1s$ state of the target atoms, namely the impact-induced single K-shell ionization (SI), the single $1s$ target electron capture (SC), the impact-induced double K-shell ionization (DI), the double $1s$ target electron capture (DC) and the combination of an impact-induced single K-shell ionization and a single $1s$ target electron capture (SI+SC).

In the CTMC approach, the cross section is given by [148]:

$$\sigma_R = \frac{N_R}{N} \cdot \pi \cdot b_{max}^2 \ , \tag{III.37}$$

where $R =$ SI, SC, DI, DC or SI+SC, N_R stands for the number of collisions satisfying the criteria for the process R, N is the total number of calculated trajectories and b_{max} the largest value of the impact parameter for which impact ionization or charge transfer can occur. The error (standard deviation) of the cross section σ_R reads [148]:

$$\Delta\sigma_R = \sqrt{\frac{N - N_R}{N \cdot N_R}} \cdot \sigma_R \ . \tag{III.38}$$

For both the SCA and CTMC calculations, the cross sections were computed for three beam energies, namely for 135, 140 and 145 MeV in the case of C and 170, 175 and 180 MeV in the case of Ne. The theoretical cross sections corresponding to the average beam energies quoted in Table III.2 were then determined by linear interpolation.

The SI and DI cross sections provided by the CTMC calculations for the C-Ca collision are for instance 144'400(600) b and 4'719(99) b, respectively, whereas the SC, DC and SI+SC cross sections amount to 70'980(440) b, 1'117(49) b and 4'738(100) b, respectively. The ratios $\sigma_{SC}/(\sigma_{SI}+\sigma_{SC})$ and $(\sigma_{DC}+\sigma_{SI+SC})/(\sigma_{DI}+\sigma_{DC}+\sigma_{SI+SC})$ are thus about 33% and 55%, respectively, which indicates that the electron capture process is indeed not negligible for this collision. The SI and DI cross sections predicted for the same collision by the SCA HWF model are 119'800 b and 1'760 b, those obtained from the SCA DHF calculations 153'600 b and 2'670 b, respectively. One sees that the CTMC SI cross section is similar to the one provided by the SCA DHF model but the CTMC DI cross section is almost 1.8 times bigger and thus probably overestimated. The same trend is also observed for the other targets and this explains why the CTMC DCI cross section ratios quoted in the 5^{th} column of Table III.13 are bigger than the SCA ones.

For the Ne-Ca collision, the CTMC cross sections are σ_{SI} = 241'600(1000) b, σ_{SC} = 388'900(1300) b, σ_{DI} = 13'060(190) b, σ_{DC} = 30'640(310) b and σ_{SI+SC} = 41'870(350) b. For comparison, the corresponding SI and DI cross sections predicted by the SCA HWF and SCA DHF models are 367'600 b and 18'320 b, and 454'550 b and 26'280 b, respectively. For the Ne-Ca collision, the SI and DI CTMC cross sections are thus smaller by a factor 1.9 for SI and 2.0 for DI than the SCA DHF ones, so that the CTMC DCI σ_{KK}/σ_{K} cross section ratio is somewhat smaller (about 7%) than the SCA DHF one. For the collisions between Ne and the three other targets, the differences between the DI cross sections predicted by the CTMC and SCA DHF are more pronounced so that the CTMC DCI cross section ratios are significantly smaller than the SCA DHF ones, the relative deviations increasing with Z from 20% for V up to 60% for Cu.

As mentioned before, the average equilibrium charge Z_{eff} of the C beam in all four targets was found to be 5.8+. This means that 80% of the C ions were fully stripped and 20% of them had still one 1s electron. As the calculations were performed for bare ions, the obtained DCI and EC cross sections should be corrected to account for the percentage of non completely stripped projectiles. In other words, as the DCI cross sections are proportional to the squared charge of the projectile, the SI and DI cross sections should be multiplied by $(5.8/6)^2 = 0.93$, the DC cross sections by 0.8 and the SC cross sections by (0.8 x 2 + 0.2 x 1)/2 = 0.9 since two 1s holes are available for 80% of the projectiles but only one for the remaining 20% C^{5+} ions. As a consequence, for the collisions with the C ions, the total cross sections including both the DCI and EC contributions were calculated using the following relations:

$$\sigma_K = 0.93 \cdot \sigma_{SI} + 0.90 \cdot \sigma_{SC} \ , \tag{III.39}$$

$$\sigma_{KK} = 0.93 \cdot \sigma_{DI} + 0.80 \cdot \sigma_{DC} + 0.84 \cdot \sigma_{SI+SC} \ . \tag{III.40}$$

Similarly, for Ne the average equilibrium charge was found to be 9.4+, which means that in this case only 40% of the ions were fully stripped and 60% of them corresponded to Ne^{9+} ions. Thus, for the Ne beam the SI and DI cross sections should be multiplied by 0.88, the DC cross sections by 0.4 and the SC cross sections by (0.4 x 2 + 0.6 x 1)/2 = 0.7. For the collisions with Ne, the total cross sections were thus calculated as follows:

$$\sigma_K = 0.88 \cdot \sigma_{SI} + 0.70 \cdot \sigma_{SC} \ , \tag{III.41}$$

$$\sigma_{KK} = 0.88 \cdot \sigma_{DI} + 0.40 \cdot \sigma_{DC} + 0.62 \cdot \sigma_{SI+SC} \ . \tag{III.42}$$

The CTMC cross section ratios calculated using the above equations are presented in the 6^{th} columns of Tables III.13 and III.14. From the comparison of the CTMC DCI cross section ratios which remain unchanged when Z_p is replaced by Z_{eff} and the CTMC DCI+EC ones, one sees that, as assumed, the consideration of the EC process increases the cross section ratios. Actually the increase is too large since the CTMC DCI+EC cross section ratios are clearly too big, about 2.2 times bigger than the experimental ones for C and 1.6 times bigger for Ne. This is, however, not really surprising because it is well known that the EC cross sections [140] are considerably overestimated by theory [149]. In order to take into consideration this overestimation of the theoretical EC cross sections, we have scaled the CTMC EC predictions, corrected beforehand for the effective charge of the ions, by multiplying them with a constant parameter α. The same value of α was assumed for the C and Ne ions. The scaling parameter α was determined by minimizing the sum of the squared differences between the experimental cross section ratios σ_{KK}/σ_K and the scaled theoretical cross section ratios, i.e, by solving the following equation:

$$\frac{d}{d\alpha}S(\alpha)=\frac{d}{d\alpha}\left\{\sum_{i=1}^{4}\left[\left(\frac{\sigma_{KK}}{\sigma_K}\right)_{exp_i}-\frac{0.93\cdot\sigma_{DI_i}+\alpha\cdot(0.80\cdot\sigma_{DC_i}+0.84\cdot\sigma_{(SI+SC)_i})}{0.93\cdot\sigma_{SI_i}+\alpha\cdot0.90\cdot\sigma_{SC_i}}\right]^2+\right.$$
$$\left.\sum_{i=5}^{8}\left[\left(\frac{\sigma_{KK}}{\sigma_K}\right)_{exp_i}-\frac{0.88\cdot\sigma_{DI_i}+\alpha\cdot(0.40\cdot\sigma_{DC_i}+0.62\cdot\sigma_{(SI+SC)_i})}{0.88\cdot\sigma_{SI_i}+\alpha\cdot0.70\cdot\sigma_{SC_i}}\right]^2\right\}=0\ . \tag{III.43}$$

where the index i stands for the collision number, i.e., $i = 1$ for the C-Ca collision, $i = 2$ for the C-V collision, ..., $i = 8$ for the Ne-Cu collision.

The scaling factor α was first determined by using the CTMC cross sections for both the DCI and EC cross sections. A value $\alpha = 0.051$ was obtained and for this α-value the sum of the squared deviations S(α) was found to be $9.84 \cdot 10^{-4}$. In a second attempt, we used the SCA DHF cross sections for the impact-induced single and double ionization and the CTMC cross sections for the single and double electron capture processes. This resulted into a bigger and thus more realistic value for α (0.107) and the sum S(α) was found to be about 8 times smaller ($1.30 \cdot 10^{-4}$), indicating a clearly better agreement with the experimental values. The theoretical σ_{KK}/σ_K cross section ratios determined this way are presented in the 7^{th} columns of Tables III.13 and III.14. As it can be seen, a nice agreement with experiment is observed in this case, all ratios quoted in the 2^{nd} (experimental ratios) and 7^{th} columns being consistent within the quoted experimental errors, the mean value of the deviations $\sqrt{\frac{S(\alpha)}{8}}$ being 0.40%, i.e., 1.5 times smaller than the average experimental uncertainty (0.60%).

III.5 Summary and concluding remarks

We have investigated the radiative decay of double K-shell vacancy states produced in solid Ca, V, Fe and Cu targets by impact with about 10 MeV/amu C and Ne ions. The K hypersatellite X-ray lines were measured by means of high energy resolution spectroscopy using a von Hamos curved crystal spectrometer whose energy resolution varied between 0.70 eV for Ca and 1.44 eV for Cu. The experiment was carried out at the Philips variable energy cyclotron of PSI. From the fits of the X-ray spectra corrected beforehand for the beam intensity fluctuations and the beam intensity profile on the target as well as for the variation with the energy of the solid angle of the spectrometer, the energies, line widths and relative intensities of the hypersatellite lines could be determined.

In general, the values obtained in the present work for the energies of the hypersatellites were found to be in satisfactory agreement with other existing experimental data and theoretical predictions. On the other hand, if one compares our values with the most recent and most precise hypersatellite energies determined using synchrotron radiation one finds that the average of the absolute values of the deviations amount to 0.9 eV for the $K\alpha_2^h$ hypersatellites and to 2.0 eV for the $K\alpha_1^h$ hypersatellites, whereas the averaged combined errors amount to 0.3 eV and 1.2 eV, respectively. In that sense, the two sets of energies are not consistent within the quoted $1-\sigma$ errors. The main reason for this discrepancy resides probably in the fact that the shapes of the close-lying M-satellites of the hypersatellites were not reproduced perfectly by the single or double Voigtians used in the fits to account for these unresolved satellite structures. One can thus conclude that the hypersatellite energies and energy shifts obtained in the present work are characterized by an accuracy of 1 eV for the $K\alpha_2$ hypersatellites and 2 eV for the weaker $K\alpha_1$ hypersatellites, which is quite satisfactory for X-ray spectroscopy measurements performed with heavy ion beams.

In average, the hypersatellite line widths obtained in our work overestimate the values determined from synchrotron radiation measurements by about 13%. This is again due to the flawed fits of the close-lying M-satellites induced by the strong multiple ionization characterizing atomic collisions involving heavy ions. In measurements performed with synchrotron radiation the M satellite induced broadening is much less crucial because the additional M-shell ionization can be produced only by shake and knockout processes which are two to three orders of magnitude weaker than the DCI and EC processes.

The main objective of the present work was to determine the single-to-double K-shell ionization cross sections for the eight investigated collisions. The cross section ratios were deduced from the corrected relative intensities of the hypersatellites. The results were found to be on one hand consistent with the theoretical predictions provided by the SCA model based on Dirac Hartree Fock wave functions but, on the other hand, systematically bigger than the latter. This was explained by the fact that the electron capture process which is not considered in the SCA model plays an important role in the investigated collisions as shown by CTMC calculations and leads to bigger cross section ratios. However, when the EC process is taken into consideration, the theoretical cross section ratios become significantly bigger than the experimental ones because, as shown in the literature, the EC cross sections are strongly overestimated by theory. The difficulty was circumvented by correcting the EC contribution with a scaling factor α which was determined by a least-squares fit method. Finally, using the SCA DHF model for the determination of the DCI cross sections and the CTMC predictions corrected by the scaling factor α=0.11 for the EC cross sections, a nice agreement between theory and experiment was found for the σ_{KK}/σ_K cross section ratios.

List of Figures

List of Tables

REFERENCES

[1] L.V. Azároff, *in Elements of X-Ray Crystallography.* McGraw-Hill Book Company, 1968.

[2] J.-Cl. Dousse and J. Hoszowska, *in High-resolution XAS/XES, Chapt. 2: Crystal Spectrometers.* CRC Press, Taylor & Francis Group, 2015.

[3] P.-A. Raboud, M. Berset, J.-Cl. Dousse and Y.-P. Maillard, *Phys. Rev. A*, vol. 65, p. 022512, 2002.

[4] O. Mauron *et al.*, *Phys. Rev. A*, vol. 67, p. 032506, 2003.

[5] K. Fennane *et al.*, *Phys. Rev. A*, vol. 88, p. 052506, 2013.

[6] J. Hoszowska, J.-Cl. Dousse, and Ch. Rhême, *Phys. Rev. A*, vol. 50, p. 123, 1994.

[7] P.-A. Raboud, J.-Cl. Dousse, J. Hoszowska, and I. Savoy, *Phys. Rev. A*, vol. 61, p. 012507, 1999.

[8] K. Fennane *et al.*, *Phys. Rev. A*, vol. 92, p. 022507, 2015.

[9] B. Galley and J.-Cl. Dousse, *Phys. Rev. A*, vol. 50, p. 3058, 1994.

[10] J. Hoszowska *et al.*, *Phys. Rev. Lett.*, vol. 107, p. 053001, 2011.

[11] Ch. Herren and J.-Cl. Dousse, *Phys. Rev. A*, vol. 53, p. 717, 1996.

[12] A. Mühleisen, M. Budnar, and J.-Cl. Dousse, *Phys. Rev. A*, vol. 54, p. 3852, 1996.

[13] Ch. Herren and J.-Cl. Dousse, *Phys. Rev. A*, vol. 56, p. 2750, 1997.

[14] J. Szlachetko *et al.*, *Phys. Rev. Lett.*, vol. 97, p. 073001, 2006.

[15] J. Szlachetko *et al.*, *Phys. Rev. A*, vol. 75, p. 022512, 2007.

[16] Y.-P. Maillard, J.-Cl. Dousse, J. Hoszowska, *Eur. Phys. J. D*, vol. 57, p. 157, 2010.

[17] J.P. Briand *et al.*, *J. Phys. B: At. Mol. Phys.*, vol. 9, p. 1055, 1976.

[18] B. Boschung *et al.*, *Phys. Rev. A*, vol. 51, p. 3650, 1995.

[19] M. Polasik *et al.*, *Phys. Rev. Lett.*, vol. 107, p. 073001, 2011.

[20] C.A. Back *et al.*, *Phys. Rev. Lett.*, vol. 87, p. 275003, 2001.

[21] S.M. Kahn *et al.*, *Astron. Astrophys.*, vol. 365, p. L312, 2001.

[22] K. Fennane *et al.*, *Phys. Rev. A*, vol. 79, p. 032708, 2009.

[23] J. Hoszowska *et al.*, *Phys. Rev. Lett.*, vol. 102, p. 073006, 2009.

[24] J. Hoszowska *et al.*, *Phys. Rev. A*, vol. 82, p. 063408, 2010.

[25] J. Rzadkiewicz *et al.*, *Phys. Lett. A*, vol. 264, p. 186, 1999.

[26] M. Czarnota *et al.*, *Eur. Phys. J. D*, vol. 57, p. 321, 2010.

[27] M. Czarnota *et al.*, *Phys. Rev. A*, vol. 88, p. 052505, 2013.

[28] M. Czarnota *et al.*, *Rad. Phys. Chem.*, vol. 68, p. 121, 2003.

[29] T. Papp, J. L. Campbell, J. A. Maxwell, J.-X. Wang, and W. J. Teesdale, *Phys. Rev. A*, vol. 45, p. 1711, 1992.

[30] R. D. Deslattes *et al.*, *Rev. Mod. Phys.*, vol. 75, p. 35, 2003.

[31] J. A. Bearden, *Rev. Mod. Phys.*, vol. 39, p. 78, 1967.

[32] J. C. Fuggle and N. Martensson, *J. El. Spectrosc. Relat. Phenom.*, vol. 21, p. 275, 1980.

[33] J. L. Campbell and T. Papp, *At. Data Nucl. Data Tables*, vol. 77, p. 1, 2001.

[34] O. Keski-Rahkonen, G. Materlik, B. Sonntag and J. Tulkki, *J. Phys. B : At. Mol. Phys.*, vol. 17, p. 121, 1984.

[35] S. Svensson *et al.*, *J. El. Spectrosc. Relat. Phenom.*, vol. 9, p. 51, 1976.

[36] R. Nyholm and N. Martensson, *Phys. Rev. B*, vol. 36, p. 20, 1987.

[37] M. Szlachetko, M. Berset, J.-Cl. Dousse, J. Hoszowska, and J. Szlachetko, *Rev. Sci. Instrum.*, vol. 84, p. 093104, 2013.

[38] J. Hoszowska, J.-Cl. Dousse, J. Kern, Ch. Rhême, *Nucl. Instrum. Methods Phys. Res. A*, vol. 376, p. 129, 1996.

[39] J.-Cl. Dousse and J. Hoszowska, *Phys. Rev. A*, vol. 56, p. 4517, 1997.

[40] W. Schwitz, *Nucl. Instrum. Methods*, vol. 154, p. 95, 1978.

[41] W. Beer, P. F. A. Goudsmit, and L. Knecht, *Nucl. Instrum. Meth. A*, vol. 219, p. 322, 1984.

[42] O. I. Sumbaev, *Sov. Phys. JETP*, vol. 5, p. 1042, 1957.

[43] R. C. Sharma *et al.*, *Nucl. Instrum. Methods*, vol. 130, p. 305, 1975.

[44] R. D. Deslattes, E. G. Kessler, Jr., *in Atomic Inner-Shell Physics.* Ed. by B. Crasemann (Plenum Press, New York), 1985.

[45] R. D. Deslattes, M. Tanaka, G. L. Greene, A. Henins, and E. G. Kessler, Jr., *IEEE Trans. Instrum. Meas.*, vol. 36, p. 166, 1987.

[46] J. Szlachetko *et al.*, *Rev. Sci. Instrum.*, vol. 78, p. 093102, 2007.

[47] P. J. Mohr, B. N. Taylor, and D. B. Newell, *J. Phys. Chem. Ref. Data*, vol. 37, p. 1187, 2008.

[48] F. James and M. Roos, *Comput. Phys. Commun.*, vol. 10, p. 343, 1975.

[49] G. K. Wertheim, M. A. Butler, K. W. West, and D.N.E. Buchanan, *Rev. Sci. Instrum.*, vol. 45, p. 11, 1974.

[50] J. H. Scofield, *At. Data Nucl. Data Tables*, vol. 14, p. 121, 1974.

[51] T. A. Carlson and C. W. Nestor, *Phys. Rev. A*, vol. 8, p. 2887, 1973.

[52] T. Mukoyama and Y. Ito, *Nucl. Instrum. Methods B*, vol. 87, p. 26, 1994.

[53] F. Parente, M. H. Chen, B. Crasemann, and H. Mark, *At. Data Nucl. Data Tables*, vol. 26, p. 383, 1991.

[54] J. H. Scofield, *in Atomic Inner-Shell Processes.* Ed. by B. Crasemann (Academic Press, New York), 1975, vol. 1.

[55] Z. Rudzikas, *Theoretical Atomic Spectroscopy.* Cambridge Monographs on Atomic, Molecular and Chemical Physics. Cambridge University Press, 1997, vol. 7.

[56] J. P. Santos, J. P. Marques and F. Parente, P. Indelicato, and J. P. Desclaux, *At. Data Nucl. Data Tables*, vol. 76, p. 49, 2000.

[57] J. P. Santos, *private communication.*

[58] M. O. Krause, *J. Phys. Chem. Ref. Data*, vol. 8, p. 307, 1979.

[59] E. J. McGuire, *Phys. Rev. A*, vol. 5, p. 1052, 1972.

[60] W. Uchai, C. W. Nestor, Jr., S. Raman, and C. R. Vane, *At. Data Nucl. Data Tables*, vol. 34, p. 201, 1986.

[61] J. Härtwig, G. Hölzer, J. Wolf, and E. Förster, *J. Appl. Cryst.*, vol. 26, p. 539, 1994.

[62] P. Indelicato, S. Boucard, and E. Lindroth, *Eur. Phys. J. D*, vol. 3, p. 29, 1998.

[63] J. A. Bearden and A. F. Burr, *Rev. Mod. Phys.*, vol. 39, p. 125, 1967.

[64] E. Storm and H. I. Israel, *Nucl. Data Tables*, vol. 7, p. 565, 1970.

[65] M. Polasik, *private communication.*

[66] K.-N. Huang, M. Aoyagi, M. H. Chen, B. Crasemann, H. Mark, *At. Data Nucl. Data Tables*, vol. 18, p. 243, 1976.

[67] M. H. Chen, B. Crasemann, M. Aoyagi, K. Huang, and H. Mark, *At. Data Nucl. Data Tables*, vol. 26, p. 561, 1981.

[68] M. H. Chen and B. Crasemann, H. Mark, *Phys. Rev. A*, vol. 27, p. 2989, 1983.

[69] G. P. Williams. [Online]. Available: http://xray.uu.se/hypertext/EBindEnergies.html

[70] M. Polasik, *Phys. Rev. A*, vol. 52, p. 227, 1995.

[71] I. P. Grant, B.J. McKenzie, P. H. Norrington, D. F. Mayers, and N. C. Pyper, *Comput. Phys. Commun.*, vol. 21, p. 207, 1980.

[72] G. C. Nelson, W. John, B. G. Saunders, *Phys. Rev.*, vol. 187, p. 1, 1969.

[73] G. C. Nelson, W. John, B. G. Saunders, *Phys. Rev. A*, vol. 2, p. 542, 1970.

[74] G. C. Nelson and B.G. Saunders, *J. Phys. Colloques*, vol. 32, pp. C4–97, 1971.

[75] S. I. Salem and P. L. Lee, *At. Data Nucl. Data Tables*, vol. 18, p. 233, 1976.

[76] E. G. Kessler *et al.*, *Phys. Rev. A*, vol. 26, p. 2696, 1982.

[77] M. O. Krause and J. H. Oliver, *J. Phys. Chem. Ref. Data*, vol. 8, p. 329, 1979.

[78] M. H. Chen and B. Crasemann, H. Mark, *Phys. Rev. A*, vol. 21, p. 436, 1980.

[79] M. H. Chen and B. Crasemann, H. Mark, *Phys. Rev. A*, vol. 24, p. 177, 1981.

[80] M. H. Chen and B. Crasemann, H. Mark, *Phys. Rev. A*, vol. 21, p. 449, 1980.

[81] J. N. Cooper, *Phys. Rev.*, vol. 61, p. 234, 1941.

[82] J. H. Williams, *Phys. Rev.*, vol. 45, p. 71, 1934.

[83] E. J. McGuire, *Phys. Rev. A*, vol. 5, p. 1043, 1972.

[84] E. J. McGuire, *Phys. Rev. A*, vol. 9, p. 1840, 1974.

[85] E. J. McGuire, *Phys. Rev. A*, vol. 13, p. 1288, 1976.

[86] E. J. McGuire, *Phys. Rev. A*, vol. 3, p. 587, 1971.

[87] M. H. Chen and B. Crasemann, H. Mark, *At. Data Nucl. Data Tables*, vol. 24, p. 13, 1979.

[88] M. Ohno and G. Wendin, *Phys. Rev. A*, vol. 31, p. 2318, 1985.

[89] M. Ohno, *Phys. Rev. B*, vol. 29, p. 3127, 1984.

[90] I. Salem and P. L. Lee, *Phys. Rev. A*, vol. 10, p. 2033, 1974.

[91] K. J. Rawlings, B. J. Hopkins and S. D. Foulias, *J. Electron Spectrosc. Relat. Phenom.*, vol. 18, p. 213, 1980.

[92] J. C. Fuggle and S. F. Alvarado, *Phys. Rev. A*, vol. 22, p. 1615, 1980.

[93] O. Keski-Rahkonen and M. Krause, *At. Data Nucl. Data Tables*, vol. 14, p. 139, 1974.

[94] W. Heisenberg, *Z. Phys.*, vol. 32, p. 841, 1925.

[95] G. Charpak, *C. R. Hebd. Séances Acad. Sci.*, vol. 237, p. 243, 1953.

[96] J.P. Briand, P. Chevallier, M. Tavernier, and J.P. Rozet, *Phys. Rev. Lett.*, vol. 27, p. 777, 1971.

[97] F.R. Hirsh, Jr., *Rev. mod. phys.*, vol. 14, p. 45, 1942.

[98] J.P. Briand, P. Chevallier, and M. Tavernier, *J. Phys. Colloq.*, vol. 32, pp. C4–165, 1971.

[99] T. Aberg and J. Utriainen, *Phys. Rev. Lett.*, vol. 22, p. 1346, 1969.

[100] T. Mukoyama and K. Taniguchi, *Phys. Rev. A*, vol. 36, p. 693, 1987.

[101] J.A.R. Samson *et al.*, *Phys. Rev. A*, vol. 57, p. 1906, 1998.

[102] O. Keski-Rahkonen, J. Saijonmaa, M. Suvanen, and A. Servomaa, *Phys. Scr.*, vol. 16, p. 105, 1977.

[103] E. Mikkola and J. Ahopelto, *Phys. Scr.*, vol. 27, p. 297, 1983.

[104] E.P. Kanter, R.W. Dunford, B. Krässig, and S.H. Southworth, *Phys. Rev. Lett.*, vol. 83, p. 508, 1999.

[105] M. Oura *et al.*, *J. Phys. B: At. Mol. Opt. Phys.*, vol. 35, p. 3847, 2002.

[106] S. Huotari *et al.*, *J. Electron Spectrosc. Rel. Phenom.*, vol. 137, p. 293, 2004.

[107] R. Diamant *et al.*, *Phys. Rev. A*, vol. 79, p. 062511, 2009.

[108] L. Young *et al.*, *Nature*, vol. 466, p. 56, 2010.

[109] G. Doumy *et al.*, *Phys. Rev. Lett.*, vol. 106, p. 0830002, 2011.

[110] B. Rudek *et al.*, *Nat. Photon.*, vol. 6, p. 858, 2012.

[111] K. Tamasaku *et al.*, *Phys. Rev. Lett.*, vol. 111, p. 0430001, 2013.

[112] H. Yoneda *et al.*, *Nat. Commun.*, vol. 5, p. 5080, 2010.

[113] J. Hoszowska *et al.*, *ICPEAC 2015 Toledo, Spain, booklet of abstracts.* [Online]. Available: https://intranet.pacifico-meetings.com/amsysweb/publicacionOnline.jsf?id=236

[114] E. Mikkola, O. Keski-Rahkonen, and R. Kuoppala, *Phys. Scr.*, vol. 19, p. 29, 1979.

[115] S. I. Salem, *Phys. Rev. A*, vol. 21, p. 858, 1980.

[116] M. Kavcic, M. Kobal, M. Budnar, J.-Cl. Dousse and K. Tökesi, *Nucl. Instrum. Meth. Phys. Res. B*, vol. 233, p. 235, 2005.

[117] P. Richard, W. Hodge, and C. F. Moore, *Phys. Rev. Lett.*, vol. 29, p. 393, 1972.

[118] P. Richard, *in Atomic Inner-Shell Processes.* Ed. by B. Crasemann, Academic Press, New York, 1975.

[119] D.J. Nagel, A.R. Knudson, and P.G. Burkhalter, *J. Phys. B: At. Mol. Phys.*, vol. 8, p. 2779, 1975.

[120] Y. Awaya *et al.*, *Phys. Lett. A*, vol. 61, p. 111, 1977.

[121] M. Kobal *et al.*, *Phys. Rev. A*, vol. 70, p. 062720, 2004.

[122] J. Dunn *et al.*, *Phys. Rev. Lett.*, vol. 80, p. 2825, 1998.

[123] J. F. Ziegler. [Online]. Available: http://www.srim.org/SRIM/SRIM2003.htm

[124] D. Trautmann and D. Rösel, *Nucl. Instrum. Methods*, vol. 169, p. 259, 1980.

[125] [Online]. Available: http://www.nist.gov/pml/data/xcom/

[126] M. del Rio and R. Dejus. [Online]. Available: http://www.esrf.eu/UsersAndScience/Experiments/TBS/SciSoft/xop2.3/

[127] M. H. Chen, B. Crasemann, H. Mark and T. Papp, *Phys. Rev. A*, vol. 25, p. 1, 1982.

[128] A. M. Costa, M. C. Martins, J. P. Santos, P. Indelicato, F. Parente, *J. Phys. B: At. Mol. Opt. Phys.*, vol. 40, p. 57, 2007.

[129] A. M. Costa, M. C. Martins, J. P. Santos, F. Parente, P. Indelicato, *J. Phys. B: At. Mol. Opt. Phys.*, vol. 39, p. 2355, 2006.

[130] M. H. Chen, B. Crasemann and H. Mark, *Phys. Rev. A*, vol. 25, p. 391, 1982.

[131] L. Natarajan, *Phys. Rev. A*, vol. 78, p. 052505, 2008.

[132] H. R. Verma, *J. Phys. B: At. Mol. Opt. Phys.*, vol. 33, p. 3407, 2000.

[133] D. K. Olsen and C. F. Moore, *Phys. Rev. Lett.*, vol. 33, p. 194, 1974.

[134] D. Mitra, M. Sarkar, D. Bhattacharya, L. Natarajan, *X-Ray Spectrometry*, vol. 37, p. 585, 2008.

[135] S. I. Salem, A. Kumar and B. L. Scott, *Phys. Rev. A*, vol. 29, p. 2634, 1984.

[136] J. Ahopelto, E. Rantavuori, O. Keski-Rahkonen, *Phys. Scr.*, vol. 20, p. 71, 1979.

[137] G.P. Williams, *Electron Binding Energies, X-Ray Data Booklet, Lawrence Berkeley National Laboratory.* [Online]. Available: http://xdb.lbl.gov/xdb-new.pdf

[138] J.P. Mossé, P. Chevallier, and J.P. Briand, *Z. Phys. A*, vol. 322, p. 207, 1985.

[139] G. Basbas and W. Brandt, R. Laubert, *Phys. Rev. A*, vol. 7, p. 983, 1973.

[140] J.R. Oppenheimer, *Phys. Rev.*, vol. 31, p. 349, 1928.

[141] V.S. Nikolaev and I.S. Dmitriev, *Physics Letters A*, vol. 28, p. 277, 1968.

[142] K. Shima, T. Mikumo, and H. Tawara, *At. Data Nucl. Data Tables*, vol. 34, p. 357, 1986.

[143] J. Bang and J.M. Hansteen, *Kgl. Danske Videnskab Selskab, Mat.-Fys. Medd.*, vol. 31.

[144] Z. Halabuka, W. Perger, and D. Trautmann, *Z. Phys. D*, vol. 29, p. 151, 1994.

[145] B. Boschung *et al.*, *Phys. Rev. A*, vol. 52, p. 3889, 1995.

[146] Ch. Herren *et al.*, *Phys. Rev. A*, vol. 57, p. 235, 1998.

[147] M. Karplus, R.N. Porter, and R.D. Sharma, *J. Chem. Phys.*, vol. 43, p. 3259, 1965.

[148] R.E. Olson and A. Salop, *Phys. Rev. A*, vol. 16, p. 531, 1977.

[149] F.T. Chan and J. Eichler, *Phys. Rev. Lett.*, vol. 42, p. 58, 1979.

REMERCIEMENTS / ACKNOWLEDGEMENTS

Je tiens ici à remercier tous ceux qui, de près ou de loin, directement ou indirectement, ont permis que ce travail puisse être mené à terme.

En premier lieu, je veux remercier très chaleureusement mon Directeur de thèse, le Prof. Jean-Claude Dousse, qui m'a offert la possibilité d'entrer dans le monde de la recherche scientifique. Avec une très grande bienveillance, il m'a guidé tout au long des nombreuses années qu'a duré ce travail.

Un merci tout particulier à Dr. hab. Joanna Hoszowska pour son soutien, son expertise et ses encouragements. Elle aussi a vu défiler toutes ces années durant lesquelles j'ai pu bénéficier de son expérience et des ses connaissances étendues.

I would like to aknowledge Prof. Marek Pajek from the Jan Kochanowski University, Kielce, Poland, for the review of my PhD.

I would also like to acknowledge Prof. Jose Paulo Santos and Prof. Fernando Parente from the New University of Lisbon, Portugal, as well as Prof. Jose Pires Marques from the University of Lisbon, Portugal, for the computation of the $L_{2,3}$ Coster-Kronig yields of Hg. The latter were particularly useful for the determination of the theoretical line shapes of the M- and N-shell satellites employed in the data analysis. Many thanks also to Prof. Marek Polasik from Nicolaus Copernicus University, Torun, Poland, for the MCDF calculations of the binding energies of the Hg core-levels.

My thanks also go to Dr. hab. Matjaz Kavčič from the Josef Stefan Institute, Ljubljana, Slovenia, for the HWF SCA calculations, to Dr. hab. Darek Banaś, from the Jan Kochanowski University, Kielce, Poland, for the DHF SCA calculations and to Dr. Karoly Tökésy from the Institute of Nuclear Research of the Academy of Sciences, Debrecen, Hungary for the CTMC simulations.

Ma reconnaissance va aussi à feu le Prof. Jean Kern grâce à qui toute cette aventure a débuté. Au travers d'un stage d'été il m'a ouvert les portes de son groupe de recherche (PAN devenu par la suite AXP). Je veux remercier ici les membres actuels et anciens de ces groupes. Grâce à eux, j'ai pu bénéficier d'une ambiance de travail agréable et d'échanges très constructifs. Merci donc à Christophe, Didier, Pierre-Alexandre, Isabelle, Olivier, Jacek, Jakub, Karima, Monika, Cao, Yves, Staszek, Lucie et Faisal. Un merci tout particulier à Wojciech pour l'aide apportée à la résolution des problèmes LaTex.

Les équipes techniques et administratives ont toujours donné un écho constructif à mes diverses sollicitations. Un merci particulier à Oswald, Jean-Louis, Roger, Elmar, Martial, Olivier, Francis, Michel, Elisabeth, Marie-Louise, Eliane, Nadia, Anne et Bernadette.

Ma gratitude dépasse le cadre universitaire pour s'adresser à ceux qui ont accepté que je poursuive le travail de thésard en freelance, en permettant des adapations même dans le cadre d'une activité professionelle à plein temps. Je veux citer ici feu Monsieur Pierre Telley et Monsieur Pius Lehmann, Directeurs de l'Ecole Normale Cantonale de Fribourg, Messieurs Nicolas Renevey et Jacques de Coulon, Recteurs du Collège St-Michel de Fribourg et enfin Monsieur Thierry Maire, Directeur du GYB à Payerne.

Je tiens à remercier tout spécialement mon épouse Sandra ainsi que mes enfants Klara-Sophia et Arius, lesquels ont consenti à me donner le temps nécessaire à l'achèvement de ma thèse.

Dans l'organisation du quotidien, les grands-parents ont joué un rôle très important avec une grande disponibilité de temps qu'ils ont consacré à Klara-Sophia et Arius... pour le plus grand plaisir de ceux-ci. Pour moi ils ont bien-sûr été d'un soutien indéfectible. Merci tout particulièrement à mes parents François & Myrtha, ainsi qu'à Werner & Elisabeth.

Dans les moments plus difficiles ou simplement quand tout allait bien, j'ai toujours pu compter sur mes amis Boris-Alexandre & Frédérique, Willy, Viivi, Philippe & Chantal, Yitzhak & Noale, John, Verena, Marjan, Cecilie, Svetlana et Grégory. Merci à chacun.

En dernier lieu, je veux exprimer ma sincère gratitude à Gabriel & Charlotte pour toute la confiance témoignée.

Curriculum vitae

Personal details

First name & family name:	**Yves-Patrik Maillard**
Date and place of birth:	10.05.1973, Billens, Switzerland
Nationality:	Swiss
Marital status:	married with Sandra Priska Aeppli; two children: Klara-Sophia and Arius
Current address:	Route de Villaranon 8 1681 Hennens Switzerland
Languages:	French (native) English (fluent) German (basic)
Social commitment:	Choeur des Armaillis de la Gruyère

Education & research

1998 – **present day**	University of Fribourg Ph.D. studies on high resolution X-ray spectroscopy activities: participation in experiments at facilities: Philipps^{TM} Cyclotron (Paul Scherrer Institute, Villigen, Switzerland), Swiss Light Source (Paul Scherrer Institute, Villigen, Switzerland), European Synchrotron Radiation Facility (Grenoble, France) and in other in-house experiments; contributions to conferences: ISPA 2002 (7thICR Seminar) (2002, Kyoto, Japan), IWP 2002 (2002, SPring 8, Hyogo, Japan).
2010 – **2011**	Agrilogie Moudon Degree in agricultural sciences: Certified farmer (Option: Organic Agriculture Processes).
2003 – **2006**	University of Fribourg Did@cTIC: *Higher education & educational technology training (Prof. Dr. Bernadette Charlier).*
2005	EPFL Lausanne Postgrade education: *Space operations technologies (Prof. Dr. Claude Nicollier).*
2004 – **2005**	Swiss Firemen Federation Firefighter Instructor (I & II).
2000 – **2002**	CNED - Paris Basic education in astronomy & astrophysics (I & II).
1997 – **1999**	University of Fribourg *Swiss Gymnasium College Teacher (Mathematics & Physics).*
1993 – **1998**	University of Fribourg Master in Physics (Mathematics as option) with Master Thesis in Experimental Physics.
1989 – **1993**	Highschool, Collège St-Michel, Fribourg.
1985 – **1989**	Secondary School, Romont.
1979 – **1985**	Primary School, Siviriez.

Employment history

2007 – **present day**	Gymnase Intercantonal de la Broye, Payerne Regular Teacher in Mathematics and Physics. special activities: Commemoration event based on 50^{th} anniversary of J. F. Kennedy assassination (co-organized with Dr. Willy Dinkelmann and in partnership with Prof. Dr. Alexandre Vautravers (Webster University Geneva).
2002 – **present day**	University of Fribourg & HEP Lausanne *Teacher coach.*
1998 – **2013**	Observatoire du Moléson In charge of popularization training in astronomy. special activities: Organization of the events based on 1999, 11^{th} of August solar eclipse and 2012 6^{th} of June solar Venus transit.
2004 – **2011**	Swiss Firemen Federation On-duty firefighter instructor.
1993 – **2011**	Siviriez On-duty firefighter. special activities: from 2000, commanding officer, in charge of the education & training.
2004 – **2011**	University of Fribourg Graduate assistant for advanced students, dedicated to astronomical laboratory education.
2000 – **2007**	Collège St-Michel, Fribourg Regular Teacher in Mathematics and Physics. special activities: *Prize award (10'000 CHF) for innovative educational projects in the field of new evaluation implementation for physics students.* *Class Supervisor from 2003 to 2007.* *Organization of an event based on 2004, 8^{th} of June solar Venus transit.*
2002 – **2004**	Departement of Education and Culture, Fribourg Provider of post-graduate education in astronomy for primary and secondary teachers.
1999 – **2002**	State Teacher Training School, Fribourg Regular Teacher in Physics. special activities: 2000, Study trip to Prague. Supervisor. Class Supervisor in 2000 & 2001.
1998 – **1999**	University of Fribourg Graduate assistant. activities: Laboratory training and exercices sessions.

List of publications

Refereed articles

J. Hoszowska, J.-Cl. Dousse, D. Castella, D. Corminboeuf, J. Kern, Y.-P. Maillard and P.-A. Raboud.
Influence of the chemical environment on the Si KL X-ray satellite spectra of transition metal silicides bombarded by 43 MeV neon ions.
J. Phys. B : At. Mol. Phys. **33**, 3165 (2000).

D. Castella, D. Corminboeuf, J.-Cl. Dousse, J. Hoszowska, Y.-P. Maillard and P.-A. Raboud.
Trapping of xenon in polymeric films by photopolymerization.
Macromolecules **33**, 8583 (2000).

M. Pajek, D. Banas, D. Castella, D. Corminboeuf, J.-Cl. Dousse, Y.-P. Maillard, O. Mauron, P.-A. Raboud, D. Chmielewska, I. Fijal, M. Jaskola, A. Korman, T. Ludjiejewski, J. Rzadkiewicz, Z. Sujkowski, J. Hoszowska, M. Polasik and T. Mukoyama.
High-resolution measurements of Th and U $L\gamma$ *X-rays induced by energetic ions.*
Proc. of the 10th International Conference on the Physics of Highly Charged Ions (HCI 2000), Berkeley, USA, Jul. 30-Aug. 3, 2000. Phys. Scr. T92 (2001) 382.

J. Rzadkiewicz, D. Chmielewska, Z. Sujkowski ; M. Berset, J.-Cl. Dousse, Y.-P. Maillard, O. Mauron, P.-A. Raboud ; J. Hoszowska ; M. Polasik, K. Slabkowska ; and M. Pajek.
Effect of L- and M-subshell ionization on the K X-ray diagram and hypersatellite lines of cadmium.
Act. Phys. Pol. B **33** 415 (2002).

P.-A. Raboud, M. Berset, J.-Cl. Dousse and Y.-P. Maillard.
L_1 *atomic level width of elements* $62 \leq Z \leq 83$.
Phys. Rev. A **65** 022512 (2002).

P.-A. Raboud, M. Berset, J.-Cl. Dousse, Y.-P. Maillard, O. Mauron; J. Hoszowska; M. Polasik and J. Rzadkiewicz.
Energy dependent KL double photoexcitation of Argon.
Phys. Rev. A**65** 062503 (2002).

J.-Cl. Dousse, M. Berset, Y.-P. Maillard and P.-A. Raboud.
Revisited L_1 atomic-level widths of rare-earth elements.
Proc. of the 7^{th} International Seminar on Photoionization in Atoms (ISPA), Uji, Kyoto, Japan, Aug. 2002. Kyoto University Press pp. 74-79 (2002).

M. Czarnota, M. Pajek, D. Banas, D. Chmielewska, J. Rzadkiewicz, Z. Sujkowski, J.-Cl. Dousse, M. Berset, O. Mauron, Y.-P. Maillard, P.-A. Raboud, J. Hoszowska, M. Polasik, and K. Slabkowska.
Observation of L X-ray satellites and hypersatellites in collisions of O and Ne ions with Mo and Pd.
Proc. of the 11^{th} International Conference on the Physics of Highly Charged Ions, Caen, France, Sept. 2002. Nucl. Instrum. Meth. Phys. Res. B **205** pp. 133-138 (2003).

J. Rzadkiewicz, D. Chmielewska, Z. Sujkowski, M. Berset, J.-Cl. Dousse, Y.-P. Maillard, O. Mauron, P.-A. Raboud, M. Polasik, J. Hoszowska and M. Pajek.
M-subshell ionization in near-central collisions of 20 MeV/amu carbon ions with molybdenum atoms.
Proc. of the 11^{th} International Conference on the Physics of Highly Charged Ions, Caen, France, Sept. 2002. Nucl. Instrum. Meth. Phys. Res. B **205** pp. 128-132 (2003).

M. Czarnota, M. Pajek, D. Banas, D. Chmielewska, J. Rzadkiewicz, Z. Sujkowski, J.-Cl. Dousse, M. Berset, O. Mauron, Y.-P. Maillard, P.-A. Raboud, J. Hoszowska, M. Polasik, and K. Slabkowska.
The study of Th M X-ray satellites and hypersatellites induced by energetic O and Ne ions.
Proc. of the 2^{nd} Conference on Elementary Processes in Atomic Systems, Gdansk, Poland, Sept. 2002. Rad. Phys. Chem. **68** pp. 121-125 (2003).

O. Mauron, J.-Cl. Dousse, S. Baechler, M. Berset, Y.-P. Maillard, P.-A. Raboud and J. Hoszowska.
Reexamination of the L_3 and M_1 atomic-level widths of elements $54 \leq Z \leq 77$.
Phys. Rev. A **67** (2003) 032506.

M. Kobal, M. Kavcic, M. Budnar ; J.-Cl. Dousse, Y.-P. Maillard, O. Mauron, P.-A. Raboud and K. Tökesi.
Double K shell ionization of Mg and Si induced in collisions with C and Ne ions.
Phys. Rev. A **70** 062720 (2004).

J. Rzadkiewicz, D. Chmielewska, A. Gojska, Z. Sujkowski ; M. Berset, J.-Cl. Dousse, Y.-P. Maillard, O. Mauron, P.-A. Raboud ; M. Polasik, K. Slabkowska ; J. Hoszowska and M. Pajek.
Natural widths of hypersatellite K X-ray spectra and lifetimes of double K-hole states in mid-Z atoms.
Proc. 12th International Conference on the Physics of Highly Charged Ions (HCI), Vilnius, Lithuania, Sept. 6-10, 2004. Nucl. Instrum. Meth. Phys. Res. B **235** 110 (2005).

M. Czarnota, M. Pajek, and D. Banas; J.-Cl. Dousse, Y.-P. Maillard, O. Mauron, P.A. Raboud, and M. Berset ; D. Chmielewska, J. Rzadkiewicz, and Z. Sujkowski; J. Hoszowska; K. Slabkowska and M. Polasik.
Multiple ionization effects in X-ray emission induced by heavy ions.
Proc. *XIX* International Seminar on Ion-Atom Collisions (ISIAC 05), Jul. 28-29, Rio de Janeiro, Brazil. Brazilian Journal of Physics **36** 546 (2006).

M. Czarnota, M. Pajek, D. Banas; J.-Cl. Dousse, Y.-P. Maillard, O. Mauron, P.A. Raboud, M. Berset, J. Hoszowska, K. Slabkowska, M. Polasik, D. Chmielewska, J. Rzadkiewicz and Z. Sujkowski.
Vacancy rearrangement processes in multiply ionized atoms.
Proc. 13th International Conference on the Physics of Highly Charged Ions (HCI 2006), Aug. 28-Sept. 1, 2006, Belfast, Northern Ireland, UK. J. Phys. : Conf. Series **58** 295 (2007).

K. Fennane, J.-Cl. Dousse, J. Hoszowska, M. Berset, W. Cao, Y.-P. Maillard, J. Szlachetko, M. Szlachetko, and M. Kavcic.
Double K-shell ionization of Al induced by photon and electron impact.
Phys. Rev. A bf 79 032708 (2009).

Y.-P. Maillard, J.-Cl. Dousse and J. Hoszowska.
Energies and widths of atomic core-levels in liquid mercury.
Eur. J. Phys. D **57** 155 (2010).

M. Czarnota, D. Banas, M. Berset, D. Chmielewska, J.-Cl. Dousse, J. Hoszowska, Y.-P. Maillard, O. Mauron, M. Pajek, M. Polasik, P.-A. Raboud, J. Rzadkiewicz, K. Slabkowska and Z. Sujkowski.
High-resolution X-ray study of the multiple ionization of Pd atoms by fast oxygen ions.
Eur. J. Phys. D **57** 321 (2010).

M. Czarnota, D. Banas, M. Berset, D. Chmielewska, J.-Cl. Dousse, J. Hoszowska, Y.-P. Maillard, O. Mauron, M. Pajek, M. Polasik, P.-A. Raboud, J. Rzadkiewicz, K. Slabkowska and Z. Sujkowski.
Observation of internal structure of the L-shell hypersatellites for palladium atoms multiply ionized by fast oxygen ions.
Phys. Rev. A Brief Report **81** 064702 (2010).

W. Cao, M. Kavcic, J.-Cl. Dousse, M. Berset, K. Bucar, M. Budnar, K. Fennane, J. Hoszowska, Y.-P. Maillard, J. Szlachetko, M. Szlachetko, and M. Zitnik.
High-resolution KMM radiative Auger X-ray emission spectra of calcium induced by synchrotron radiation.
Phys. Rev. A **83** 042513 (2011).

M. Czarnota, D. Banas, M. Berset, D. Chmielewska, J.-Cl. Dousse, J. Hoszowska, Y.-P. Maillard, O. Mauron, M. Pajek, M. Polasik, P.-A. Raboud, J. Rzadkiewicz, K. Slabkowska and Z. Sujkowski.
Satellite stucture of $L\alpha_{1,2}$ *and* $L\beta_1$ *X-ray transitions in mid-Z atoms multiply ionized by fast oxygen ions.*
Phys. Rev. A **88** 052505 (2013).

Conference abstracts

J.-Cl. Dousse, J. Hoszowska and Y.-P. Maillard.
High-resolution measurement of the L X-ray spectrum of mercury.
6th EPS Conf. on At. Mol. Phys. (ECAMP), Sienna, Italy, 1998, Europhys. Conf. Abstr. 22 D (1998) I-40.

J. Hoszowska, D. Castella, J.-Cl. Dousse, Y.-P. Maillard and P.-A. Raboud.
Influence of the Chemical State on the Si KL X-ray Satellite Spectra of Transition Metal Silicides bombarded by 43 MeV Ne^{3+} *ions.*
Fifteenth International Conference on the Applications of Accelerators in Research & Industry, Denton, USA, 1998, book of abstr., p. 82.

M. Pajek, D. Banas, D. Castella, D. Corminboeuf, J.-Cl. Dousse, Y.-P. Maillard, O. Mauron, P.-A. Raboud, D. Chmielewska, I. Fijal, M. Jaskola, A. Korman, T. Ludziejewski, J. Rzadkiewicz, Z. Sujkowski, M. Polasik and J. Hoszowska.
High-resolution measurements of Th and U L X-rays induced by O ions.
Physics od Highly Charged Ions (HCI), Berkeley, USA, 2000, book of abstr.

J.-Cl. Dousse, D. Castella, D. Corminboeuf, J. Hoszowska, Y.-P. Maillard and P.-A. Raboud.
Trapping of rare gases induced in polymeric substrates by X-ray and UV irradiation.
European Conference on Energy Dispersive X-ray Spectrometry (EDXRS-2000), June 19-23, 2000, Cracov, Poland, book of abstr. p. 56.

J.-Cl. Dousse, J. Hoszowska, Y.-P. Maillard and P.-A. Raboud.
High-resolution measurements of the L and M X-ray emission spectra of several heavy elements.
Sixteenth International Conference on the Applications of Accelerators in Research & Industry, Nov. 1-6, 2000, Denton, USA, book of abstr., p. 92.

J.-Cl. Dousse, D. Banas, D. Castella, D. Chmielewska, D. Corminboeuf, I. Fijal, J. Hoszowska, M. Jaskola, A. Korman, T. Ludziejewski, Y.-P. Maillard, O. Mauron, M. Pajek, M. Polasik, P.-A. Raboud, J. Rzadkiewicz, and Z. Sujkowski.
High-resolution study of thorium and uranium L X-ray spectra induced by impact with fast oxygen ions.
7th EPS Conf. on At. Mol. Phys. (ECAMP), Apr. 2-6, 2001, Berlin, Germany, Europhys. Conf. Abstr. 25 B (2001) 47.

D. Banas, M. Berset, D. Chmielewska, M. Czarnota, J.-Cl. Dousse, J. Hoszowska, Y.-P. Maillard, O. Mauron, T. Mukoyama, M. Pajek, M. Polasik, P.A. Raboud, J. Rzadkiewicz and Z. Sujkowski.
High-resolution study of L- and M X-ray satellites excited in collisions of 360-MeV oxygen ions with heavy atoms.
XXII International Conference on Photonic, Electronic and Atomic Collisions (ICPEAC), July 18-24, 2001, Santa Fe, USA, book of abstr.

P.-A. Raboud, M. Berset, J.-Cl. Dousse, J. Hoszowska, Y.-P. Maillard, O. Mauron, M. Polasik and J. Rzadkiewicz.
Energy dependent KL double photoexcitation of argon.
12th ESRF Users Meeting, Feb. 13th, 2002, Grenoble, France.

J.-Cl. Dousse, M. Berset, Y.-P. Maillard and P.-A. Raboud .
L_1 atomic-level widths of elements ranging between Samarium and Bismuth.
19th Int. Conf. on X-ray and Inner-Shell Processes (X02), June 24-28, 2002, Roma, Italy, book of abstr., p. 52.

M. Czarnota, M. Pajek, D. Banas, D. Chmielewska, J. Rzadkiewicz, Z. Sujkowski, J.-Cl. Dousse, M. Berset, O. Mauron, Y.-P. Maillard, P.-A. Raboud, J. Hoszowska, M. Polasik, and K. Slabkowska.
High-resolution measurements of Zr, Mo and Pd L X-ray satellites excited by O and Ne ions.
34th Meeting of the European Group for Atomic Spectroscopy (EGAS), July 9-13, 2002, Sofia, Bulgaria.

J.-Cl. Dousse, M. Berset, Y.-P. Maillard and P.-A. Raboud.
Revisited L_1 atomic-level widths of rare-earth elements.
International Seminar on Photoionization in Atoms (ISPA), Aug. 19-20, 2002, Uji-Kyoto, Japan, book of abstr.

J.-Cl. Dousse, M. Berset, J. Hoszowska, O. Mauron, Y.-P. Maillard, P.-A. Raboud, M. Polasik and J. Rzadkiewicz.
Energy dependent KL double photoexcitation of argon.
International Workshop on Photoionization (IWP2002), Spring-8, Aug. 22-26, 2002, Hyogo, Japan, book of abstr., p. SA04.

Y.-P. Maillard, J.-Cl. Dousse and J. Hoszowska.
Energies and widths of atomic core-levels in liquid mercury.
International Workshop on Photoionization (IWP2002), Aug. 22-26, 2002, Spring-8, Hyogo, Japan, book of abstr., p. SA12.

M. Czarnota, M. Pajek, D. Banas, D. Chmielewska, J. Rzadkiewicz, Z. Sujkowski, J.-Cl. Dousse, M. Berset, O. Mauron, Y.-P. Maillard, P.-A. Raboud, J. Hoszowska, M. Polasik and K. Slabkowska.
Observation of L X-ray (hyper)-satellites excited in collisions of O and Ne ions with mid-Z atoms.
11^{th} International Conference on the Physics of Highly Charged Ions (HCI), Sept. 1-6, 2002, Caen, France.

M. Czarnota, M. Pajek, D. Banas, D. Chmielewska, J. Rzadkiewicz, Z. Sujkowski, J.-Cl. Dousse, M. Berset, O. Mauron, Y.-P. Maillard, P.-A. Raboud, J. Hoszowska, M. Polasik and K. Slabkowska.
Study of Th M X-ray satellites and hypersatellites excited by energetic O and Ne ions.
2^{nd} Conference on Elementary Processes in Atomic systems, Sept. 2-6, 2002, Gdansk, Poland.

J.-Cl. Dousse, M. Berset, O. Mauron, Y.-P. Maillard, P.-A. Raboud, J. Hoszowska, M. Polassik and J. Rzadkiewicz.
Near-threshold argon KL satellite structures studied by high-resolution X-ray spectroscopy.
Seventeenth International Conference on the Applications of Accelerators in Research & Industry, Nov. 12-16, 2002, Denton, USA, book of abstr., p. 73.

O. Mauron, J.-Cl. Dousse, S. Baechler, M. Berset, Y.-P. Maillard, P.-A. Raboud and J. Hoszowska .
Revisited L_3 *and* M_1 *atomic level widths of elements between* $54 \leq Z \leq 70$.
13^{th} ESRF Users Meeting, Feb. 12, 2003, Grenoble, France.

M. Czarnota, D. Banas, M. Berset, D. Chmielewska, J.-Cl. Dousse, J. Hoszowska, Y.-P. Maillard, O. Mauron, M. Pajek, M. Polasik, P.-A. Raboud, J. Rzadkiewicz, K. Slabkowska and Z. Sujkowski.
The structure of palladium L X-ray satellites excited by fast oxygen and neon ions.
35^{th} Meeting of the European Group for Atomic Spectroscopy (EGAS), July 15-18, 2003, Brussels, Belgium.

M. Czarnota, D. Banas, M. Pajek; M. Berset, J.-Cl. Dousse, O. Mauron, Y.-P. Maillard, P.-A. Raboud, D. Chmielewska, J. Rzadkiewicz, Z. Sujkowski; J. Hoszowska; M. Polasik and K. Slabkowska.
High-resolution measurements of L- and M X-ray satellites and hypersatellites excited by energetic O and Ne ions.
XXIII International Conference on Photonic, Electronic and Atomic Collisions (ICPEAC), July 23-29, 2003, Stockholm, Sweden, book of abstr. p. We140.

J.-Cl. Dousse, J. Hoszowska and Y.-P. Maillard.
High-resolution study of atomic core-levels in liquid mercury.
European Conference on X-Ray Spectrometry (EXRS-2004), June 6-11, 2004, Alghero, Italy, book of abstr.

J. Szlachetko, R. Barrett, M. Berset, J.-Cl. Dousse, K. Fennane, J. Hoszowska, A. Kubala-Kukus, Y.-P. Maillard, M. Pajek, M. Szlachetko.
Resonant Raman scattering for Al, Si and their oxides.
Fourth Conference on Synchrotron Radiation in Materials Science, Aug. 23-25, 2004, Grenoble, France, book of abstr.

J. Hoszowska, J.-Cl. Dousse, M. Berset, K. Fennane, Y.-P. Maillard, J. Szlachetko and M. Szlachetko.
Size-dependent $K\beta$ *resonant X-ray emission spectra of* MnO_2 *nanopowder.*
15^{th} ESRF Users Meeting, Feb. 8-9, 2005, ESRF, Grenoble, France.

M. Czarnota, D. Banas, M. Pajek, M. Berset, J.-Cl. Dousse, O. Mauron, Y.-P. Maillard, P.-A. Raboud, D. Chmielewska, J. Rzadkiewicz, Z. Sujkowski, J. Hoszowska, M. Polasik and K. Slabkowska.
Satellite structure of Pd $L\alpha_{1,2}(L_3 - M_{4,5})$ *X-ray transition excited by oxygen ion impact.*
XXIV International Conference on Photonic, Electronic and Atomic Collisions (ICPEAC), July 20-26, 2005, Rosario, Argentina, book of abstr.

M. Czarnota, D. Banas, M. Pajek, J.-Cl. Dousse, Y.-P. Maillard, O. Mauron, M. Berset, P.A. Raboud, D. Chmielewska, J. Rzadkiewicz, Z. Sujkowski, M. Polasik, K. Slabkowska and J. Hoszowska.
Vacancy rearrangment processes in multiply ionized atoms.
Proc. 13^{th} International Conference on the Physics of Highly Charged Ions (HCI), Belfast, Northern Ireland, UK, Aug. 28-Sept. 1, 2006, book of abstr. p. 2-55.

M. Czarnota, D. Banas, M. Berset, D. Chmielewska, J.-Cl. Dousse, J. Hoszowska, Y.-P. Maillard, O. Mauron, M. Pajek, M. Polasik, P.A. Raboud, J. Rzadkiewicz, K. Slabkowska and Z. Sujkowski.
Observation of L-shell hypersatellites in ion-atom collisions.
XXV International Conference on Photonic, Electronic and Atomic Collisions (ICPEAC), July 25-31, 2007, Freiburg, Germany, book of abstr. p. We-123.

J. Hoszowska, J.-Cl. Dousse, M. Berset, W. Cao, K. Fennane, Y. Kayser, M. Kavcic, A. S. Kheifets, Y-P. Maillard, J. Szlachetko, and M. Szlachetko.
Hollow magnesium, aluminium and silicon: photon energy dependence of double 1s ionization.
Annual Meeting of the Swiss Physical Society, March 26-27, 2008, University of Geneva, booklet of abstr. p. 88.

M. Czarnota, D. Banas, M. Berset, D. Chmielewska, J.-Cl. Dousse, J. Hoszowska, Y.-P. Maillard, O. Mauron, M. Pajek, M. Polasik, P.-A. Raboud, J. Rzadkiewicz, K. Slabkowska and Z. Sujkowski.
Observation of L- and M-shell X-ray hypersatellites excited in collisions of fast oxygen ions with atoms.
21st International Conference on X-Ray and Inner-Shell Processes (X08), June 22-27, 2008, Paris, France, booklet of abstr. p. 159.

M. Czarnota, M. Pajek, D. Banas, M. Berset, J.-Cl. Dousse, Y.-P. Maillard , O. Mauron, P.-A. Raboud, D. Chmielewska, J. Rzadkiewicz, Z. Sujkowski, J. Hoszowska, K. Slabkowska and M. Polasik.
High-resolution measurements of molybdenum L-shell satellites and hypersatellites excited by oxygen and neon ions.
40th European Group for Atomic Systems (EGAS) Conference, July 2-5, 2008, Graz, Austria.

M. Czarnota, M. Pajek, D. Banas, M. Berset, J.-Cl. Dousse, Y.-P. Maillard , O. Mauron, P.-A. Raboud, D. Chmielewska, J. Rzadkiewicz, Z. Sujkowski, J. Hoszowska, K. Slabkowska, and M. Polasik.
High-resolution X-ray study of multiple ionization of Pd atoms by fast oxygen ions.
14th International Conference on the Physics of Highly Charged Ions (HCI), Sept. 1-5, 2008, Chofu, Tokyo, Japan.

M. Czarnota, M. Pajek, D. Banas, M. Polasik, K. Slabkowska, J.-Cl. Dousse, Y.-P. Maillard, O. Mauron, M. Berset, P.-A. Raboud, J. Hoszowska, D. Chmielewska, J. Rzadkiewicz and Z. Sujkowski.
Structure of satellites and hypersatellites of $L\alpha_{1,2}$ *and* $L\beta_1$ *lines in mid-Z atoms excited by oxygen ions.*
41st European Group for Atomic Systems (EGAS) Conference, July 8-11, 2009, Gdansk, Poland.

M. Czarnota, M. Pajek, D. Banas, J.-Cl. Dousse, M. Berset, O. Mauron, Y.-P. Maillard, P.A. Raboud, J. Hoszowska, M. Polasik, K. Slabkowska, D. Chmielewska, J. Rzadkiewicz and Z. Sujkowski.
The satellites and hypersatellites of $L\alpha_{1,2}$ *and* $L\beta_1$ *X-ray transitions in zirconium excited by oxygen and neon ions.*
XXVI International Conference on Photonic, Electronic and Atomic Collisions (ICPEAC), July 22-28, 2009, Kalamazoo, USA. J. Phys.: Conf. Series 194 (2009) 152012.

W. Cao, M. Berset, K. Bucar, M. Budnar, J.-Cl. Dousse, K. Fennane, J. Hoszowska, M. Kavcic, Y.-P. Maillard, J. Szlachetko, M. Szlachetko, and M. Zitnik.
High-resolution KMM radiative Auger X-ray spectra of calcium induced by synchrotron radiation.
43^{rd} European Group for Atomic Systems (EGAS) Conference, June 28-July 2, 2011, Fribourg, Switzerland.

M. Czarnota, M. Pajek, D. Banas, J.-Cl. Dousse, M. Berset, O. Mauron, Y.-P. Maillard, P.A. Raboud, J. Hoszowska, M. Polasik, K. Slabkowska, D. Chmiellewska, J. Rzadkiewicz, and Z. Sujkowski.
The X-ray satellites and hypersatellites excited in fast ion-atom collisions.
43^{rd} European Group for Atomic Systems (EGAS) Conference, June 28-July 2, 2011, Fribourg, Switzerland.

J.-Cl. Dousse, Y.-P. Maillard, M. Berset, D. Castella, J. Hoszowska, M. Kavcic, M. Kobal, O. Mauron, A. Mühleisen, P.-A. Raboud, J. Rzadkiewicz, K. Tökesi and B. Zorko.
High energy resolution measurements of the radiative decay of double K-shell vacancies in $20 \leq Z \leq 29$ *elements bombarded by fast C and Ne ions.*
XXIX International Conference on Photonic, Electronic and Atomic Collisions (ICPEAC), July 22-28, 2015, Toledo, Spain.

J-Cl. Dousse, Y.-P. Maillard, J. Hoszowska, M. Kavčič, J. Rzadkiewicz and K. Tökési.
High energy resolution measurements of K-hypersatellites X-ray spectra of solid Ca, V, Fe and Cu targets bombarded by fast C and Ne ions.
18^{th} International Conference on the Physics of Highly Charged Ions, Sept. 11-16, 2016, Kielce, Poland.

Non Refereed papers and reports

D. Banas, D. Castella, D. Chmielewska, D. Corminboeuf, J.-Cl. Dousse, I. Fijal, J. Hoszowska, M. Jaskola, A. Korman, T. Ludziejewski, Y.-P. Maillard, O. Mauron, M. Pajek, M. Polasik, P.-A. Raboud, J. Rzadkiewicz, and Z. Sujkowski.
High-resolution study of heavy-ion-induced Thorium and Uranium $L\gamma$ *X-ray spectra.*
PSI, Scientific Report 2000, Volume 1 : Particle and Matter, ISSN 1423-7296, March 2001, p.22.

J. Rzadkievicz, D. Chmielewska, T. Ludziejewski, Z. Sujkowski ; D. Castella, J.-Cl. Dousse, O. Mauron, Y.P. Maillard, P.A. Raboud, J. Hoszowska, M. Polasik and M. Pajek.
M-(sub)shell ionization in collisions of carbon ions with palladium.
The Andrzej Soltan Institute for nuclear studies, Swierk, PL, Annual Report 2000, p. 43.

J. Rzadkievicz, D. Chmielewska, Z. Sujkowski ; M. Berset, J.-Cl. Dousse, O. Mauron, Y.-P. Maillard, P.A. Raboud, J. Hoszowska, M. Polasik, K. Slabkowska and M. Pajek.
Effect of L- and M-(sub)shell ionization on the K X-ray diagram and hypersatellite lines of cadmium.
The Andrzej Soltan Institute for nuclear studies, Swierk, PL, Annual Report 2001, p. 42.

J.-Cl. Dousse, D. Banas, M. Berset, D. Chmielewska, M. Czarnota, J. Hoszowska, Y.-P. Maillard, O. Mauron, T. Mukoyama, M. Pajek, M. Polasik, P.-A. Raboud, J. Rzadkiewicz, and Z. Sujkowski.
High-resolution M_5-N_7 *and* M_4-N_6 *satellite and hypersatellite X-ray spectra of metallic thorium bombarded by 24 MeV/amu oxygen ions.*
PSI, Scientific Reports 2001, Volume 1 : Particles and Matter, ISSN 1423-7296, March 2002, p. 24.

J. Rzadkiewicz, D. Chmielewska, Z. Sujkowski, M. Berset, J.-Cl. Dousse, Y.-P. Maillard, O. Mauron, P.-A. Raboud, J. Hoszowska, M. Polasik, M. Pajek.
High-resolution study of $K\beta$ *X-ray spectra of mid-Z Atoms bombarded with 20 MeV/amu* C^{12+}*-ions.* The Andrzej Soltan Institute for nuclear studies, Swierk, PL, Annual Report 2002, p. 49.